

SILICON INTEGRATED ELECTRO-OPTIC MODULATORS
WITH ULTRA-LOW ENERGY CONSUMPTION

MAOQING XIN

(B. ENG., SHANGHAI JIAO TONG UNIVERSITY, 2007)

A THESIS SUBMITTED FOR THE DEGREE OF
DOCTOR OF PHILOSOPHY
DEPARTMENT OF ELECTRICAL AND COMPUTER ENGINEERING
NATIONAL UNIVERSITY OF SINGAPORE

2011

ACKNOWLEDGEMENT

To many, PhD work is a lonely journey into the academic abyss. It takes independent thinking, insightful perspective, and huge amount of courage and faith to keep you moving in a positive direction towards your destination. The same set of conditions applies to me, except that I am lucky enough to have all my mentors, colleagues, and friends behind me, being supportive of my decisions and movements throughout the harsh quest. Here from the bottom of my heart, I want to thank all of you who have ever shared your precious thoughts, time, and efforts with me to make this work happen. Also, I want to extend my gratefulness to those who have provided me with indispensable access to numerous research resources. Finally, those who are behind the funding for this project should never be forgotten.

In particular, I would like to thank Dr. Aaron J. Danner for recruiting me into this project and supervising this work from the very beginning to the end. Aaron is such a liberal and open minded mentor who allowed me a chance to explore the unknown in a fashion that appeals to me most. He was almost always supportive of my ideas and decisions even at the time when I just started the project around four years ago. Also, the talks with him made me inspired and encouraged from time to time. Undoubtedly, his financial support from grantors was crucial to my overseas talks and collaboration with other academic and research institutes.

Tremendous gratefulness also goes to Dr. Ching Eng Png (Jason) at Institute of High Performance Computing (IHPC) for the indispensable access to numerical study resources and guidance in device simulation processes. His long time experience in the realm of silicon photonics enlightened me when I was still new to this field and had a lasting effect on the foundation of this work. At the same time, I want to thank Dr. Jing Hua Teng at Institute of Material Research and Engineering (IMRE) for precious hands-on work experience with all the state-of-the-art fabrication facilities for CMOS compatible processing.

Special thanks to Dr. Mingbin Yu at Institute of Microelectronics (IME) for his enormous time and energy spent on the fabrication of the modulator device as well as the helpful discussions on the device processes. His hard work and devotion to his career left me lasting impression. My gratitude is also extended to Dr. Tsung-Yang Liow, Dr. Qing Fang and Dr. Lianxi Jia at IME for their helpful suggestions on the experimental characterization of the device.

For the successful completion of the work, a lot of others played a very significant role and therefore can never be left behind. Among others, Dr. Soon Thor Lim and Dr. Vivek Dixit from IHPC helped a lot on the optical device analysis in some of the industry and research projects of this work. Mr. Poh Chin Phua from SILVACO Singapore gave important guidance on the 3D device electrical simulations. Mr. Kian Chiew Seow, Mr. Kwok Peng Lai, and Ms. Barbara Lim from Exploit Technologies made great efforts for the commercialization and marketing of the breakdown-delay based depletion mode operation invention. Mr. Jun Deng from the Center for Optoelectronics (COE) lab of the National University of Singapore (NUS) helped with some of the SEM images in this work. Mrs. Musni Bte Hussain as lab officer of the same lab helped with the equipment ordering and management. Ms. Cynthia Chan and Mr. Choon-Sze Ng from Agilent Singapore provided important suggestions and information on the optical measurement setup. You made my PhD study a lot easier for me to undertake. Many thanks to you all!

This thesis is dedicated to my mother, who is always the first sunshine through my window.

TABLE OF CONTENTS

ACKNOWLEDGEMENT.....	i
TABLE OF CONTENTS.....	iii
ABSTRACT.....	vi
LIST OF FIGURES.....	vii
LIST OF TABLES.....	xiii
ACRONYMS.....	xiv
CHAPTER 1. INTRODUCTION AND MOTIVATION.....	1
1.1 <i>Introduction to silicon modulators</i>	4
1.2 <i>Photonic bandgap material based solution</i>	8
1.3 <i>Historical Modulators</i>	11
1.3.1. <i>Silicon waveguide MZI based devices</i>	11
1.3.2. <i>Silicon photonic resonator based devices</i>	14
1.3.3. <i>Polymer waveguide MZI based devices</i>	16
1.3.4. <i>Polymer photonic resonator based devices</i>	19
1.4 <i>Research objectives</i>	22
1.5 <i>Outline of the thesis</i>	22
CHAPTER 2. PHOTONIC RESONATOR BASED ELECTRO-OPTICAL MODULATORS.....	24
2.1. <i>Introduction</i>	24

2.2.	<i>Numerical methods and techniques</i>	26
2.2.1.	<i>Finite-difference time-domain method</i>	27
2.2.2.	<i>Plane wave expansion method</i>	34
2.2.3.	<i>Physically-based device simulation</i>	37
2.3.	<i>One dimensional photonic crystal cavities for EO modulators</i>	43
2.3.1.	<i>Fabry-Perot microcavity based design</i>	44
2.3.2.	<i>Cross waveguide based design</i>	53
2.4.	<i>Two-dimensional photonic crystal cavities for EO modulators</i>	61
2.4.1.	<i>Optical and electrical design of the photonic hybrid-lattice resonator based modulator</i> ..	62
2.4.2.	<i>Reduce electrical scattering by lattice transition</i>	67
2.4.3.	<i>Breakdown delay-based depletion mode operation</i>	69
2.5.	<i>Performance summary and comparison</i>	79
 CHAPTER 3. PHOTONIC WAVEGUIDE BASED MODULATORS		82
3.1.	<i>Introduction</i>	82
3.2.	<i>Numerical methods and techniques</i>	83
3.2.1.	<i>Beam propagation method for rib waveguide based MZI modulators</i>	84
3.3.	<i>Polymer-infiltrated P-S-N diode capacitor based EO phase shifter</i>	86
3.3.1.	<i>Device structure and EO overlap</i>	88
3.3.2.	<i>Parameter study and optimization</i>	93
3.3.3.	<i>Modulation performance and transmission line design</i>	98
3.4.	<i>Performance conclusion and comparison</i>	108
 CHAPTER 4. DEVICE FABRICATION AND EXPERIMENTAL CHARACTERIZATION		110

4.1. <i>Introduction</i>	110
4.2. <i>Device fabrication</i>	111
4.2.1. <i>Preliminary design</i>	112
4.2.2. <i>Process flow and technical background</i>	116
4.2.3. <i>Completed device</i>	119
4.3. <i>Optical characterization</i>	121
4.4. <i>Electrical characterization</i>	125
4.5. <i>Summary</i>	127
CHAPTER 5. SUMMARY AND FUTURE WORK	129
5.1. <i>Summary</i>	129
5.2. <i>Future work</i>	132
APPENDIX A	133
APPENDIX B	135
LIST OF REFERENCES.....	138

ABSTRACT

The ambition to create photonic devices in silicon originates from the overwhelming success of complementary metal–oxide–semiconductor (CMOS) technology. In particular, high speed silicon modulators are one of the most important applications of silicon photonics to optical communication networks, where ever-increasing demand for optical bandwidth and data transmission capacity is witnessed. The commercially available optical modulators nowadays, however, are mostly based on III-V compound semiconductor materials that involve CMOS incompatible processes. As a result, the low cost efficiency of the device-making process imposes obstacles for mass production in terms of integration.

The main scope of this work is to design silicon based high speed optical modulators with ultra-low energy consumption. Firstly, various photonic resonance and slow light media were designed to miniaturize device footprint via an enhanced nonlinear interaction between optical resonance mode and EO active region. And a high speed of 238 GHz was theoretically predicted with an ultra-low energy consumption of 26.6 fJ/bit in a compact hybrid lattice resonator based silicon modulator. Secondly, a polymer MZI based phase shifter was studied which incorporates multiple nonlinear effects (free carrier effect and Pockels effect) for an increased EO overlapped volume. The device speed was significantly improved from previous studies by employing low aspect ratio slot waveguide geometry. A record high 3-dB bandwidth of 269 GHz was demonstrated numerically with low energy consumption of 5.83 pJ/bit. Last but not least, the hybrid lattice resonator based modulator was fabricated and measured both optically and electrically, where high level agreement was found between experimental and theoretical results.

LIST OF FIGURES

Figure 1.1 An example of an EO modulator which is based on a MZI configuration.....	5
Figure 1.2 (a) IBM’s view for development of high performance computing systems; (b) an example optical channel connecting two computation cores (Courtesy of IBM TJ Watson Research Center).	8
Figure 1.3 Illustration of the idea of (a) a line defect photonic crystal waveguide and (b) a 90 degree bend with theoretically 100% transmission [6].	10
Figure 1.4 A Fabry-Perot microcavity built on a silicon layer [8]: (a) scanning electron microscope (SEM) image of the structure; (b) measured and calculated transmission spectrum of the structure shown in (a).	10
Figure 1.5 Design philosophy of an integrated EO modulator.	11
Figure 1.6 Intel’s 40 Gbps silicon modulator [12]: (a) Image of the completed device within the package; (b) cross sectional schematic of the phase shifter embedded in one of the two arms.	12
Figure 1.7 Device performance of Intel’s 40 Gbps silicon modulator [12]: (a) normalized optical response of two MZI modulators against RF frequency; (b) optical eye diagram of MZI modulator (shows data transmission at 40 Gbit/s)	13
Figure 1.8 (a) 3D schematic of the lateral P+-P-N-N+ diode embedded in the phase shifter; (b) dynamic optical response of the devices with 1 mm and 0.25 mm phase shifters [14].	14
Figure 1.9 Normalized transmission spectra of the modulator along with a schematic of the device structure (inset) [24].	15
Figure 1.10 (a) The output optical power when the modulator is driven normal and pre-emphasized NRZ signals; (b) eye-diagrams of the modulated optical output at 12.5 Gbit/s with PRBS 210-1 [24].	16
Figure 1.11 Three implementations of silicon organic hybrid electro-optic modulators proposed by Leuthold’s group with electric field magnitudes depicted on the right-hand side [31]: (a) traveling-wave strip waveguide structure; (b) traveling wave slot waveguide structure; (c) photonic crystal slot waveguide structure.	17
Figure 1.12 (a) Device schematic of the polymer based silicon slot waveguide modulator; (b) S_{21} response of the device at high frequency operation [32].	19
Figure 1.13 The polymer based slotted heterostructure resonator for optical modulation: (a) the 3D schematic of the device layout; (b) the SEM image of the fabricated device [40, 41].	20

Figure 1.14 (a) Calculated and experimental transmission spectra of the device (inset shows the SEM image of the polymer infiltrated PC lattice); (b) spectral transmission and modulation response after polymer infiltration and poling [41].	21
Figure 1.15 (a) Dark field optical micrograph of the device; (b) measured normalized S_{21} spectrum for dynamic performance demonstration [42].	21
Figure 2.1 Illustration of the active region of an injection mode modulator where the resonance peak shifts due to the free carrier effect.	24
Figure 2.2 In a Yee cell of dimension Δx , Δy , Δz , where the H field is computed at points shifted one-half grid spacing from the E field grid points [49].	28
Figure 2.3 3D FDTD layout of cross waveguide resonator: (a) 2D topview of the device showing launch, monitor, and computation domain; (b) 3D schematic of the device that corresponds to (a).	31
Figure 2.4 (a) 3D schematic of the photonic crystal slab waveguide for PWE method calculation; (b) 3D schematic of the supercell that is used in the band diagram calculation of the structure given in (a).	35
Figure 2.5 The basic structure of the SILVACO device simulation suite [44].	37
Figure 2.6 3D schematic of the device shown in Fig. 2.4: (a) device schematic that is composed by different material regions; (b) device material schematic with computation mesh (in black lines).	42
Figure 2.7 Schematic of the resonator-based electro-optic modulator: (a) cross sectional schematic of electrical profile with illustration of electrodes and embedded P-I-N diode; (b) 3D schematic of optical profile with illustration of 1D FP resonator.	45
Figure 2.8 I-V characteristic and corresponding RI change of the doped area.	46
Figure 2.9 Transient characteristic of the modulator at different bias voltages indicates a peak modulation speed of 100 MHz.	47
Figure 2.10 Fundamental mode profile of the rib waveguide with the absence of air holes and central doping.	48
Figure 2.11 Relationship between resonance peak shift, modulation depth, and power density.	50
Figure 2.12 Color coded schematic of the net doping profile of the active region located at the center of the waveguide.	50
Figure 2.13 Transient performance improvement of the device after the introduction of sidewall doping. A modulation speed of 220 MHz is detected at 1.18 V bias when DOC_2 equals 10^{19} cm^{-3} .	51
Figure 2.14 Improved performance of the modulator is detected as the value of DTW decreases from 515 to 155 nm. The upper (a) is the DC characteristic of the device, which demonstrates an increase in the modulation depth at a reduced power supply; and transient characteristic in the lower (b) indicates an improved modulation speed of 300 MHz.	52

Figure 2.15 (a) 3D schematic of the cross waveguide resonator based modulator; (b) top view of the device with notations of the optimum device dimensions.	54
Figure 2.16 Resonance peak optimization: (a) tuning lattice constant a to move mid-gap wavelength to 1550 nm; (b) tuning defect length l to position resonance peak toward the middle of the bandgap.....	55
Figure 2.17 Color coded E_x field intensity profile of the cavity mode with resonance wavelength of 1526 nm. The cavity mode penetrates partially into the side branches.	56
Figure 2.18 Electrical and optical response of the device to different doping concentrations: (a) I-V characteristics of the p-i-n diode shows a lower bias voltage is needed to achieve the same RI change for higher doping concentrations; (b) a blue shift and amplitude decrease of the resonance peak are detected with an increase of the doping concentration.....	57
Figure 2.19 DC and transient characteristics of the device performance: (a) the relationship between modulation depth, peak shift and power consumption; (b) refractive index changes with time in response to a rectangular voltage pulse with different amplitudes, and 2.9 GHz modulation speed is indicated at the bias voltage 1.65 V.	58
Figure 2.20 (a) 3D schematic of the device showing the planar HLMG resonator and electrode configuration for external driving signal. (b) The magnified 2D demonstration of the HLMG resonator constructed by hybrid PC lattice transition and additional insertion stages.....	63
Figure 2.21 (a) The defect lattice constant a_2 is selected at 400 nm for optimized cavity confinement and EO sensitivity. (b) The projected band diagram shows a wide mode gap between PC1 and PC2, which is the origin of the highly confined optical cavity resonance.	64
Figure 2.22 (a) Transmission spectrum of the HLMG resonator indicates a highly confined resonance mode in the NIR range. (b) 2D profile of the resonance mode in the xy plane. (c) 2D profile of the resonance mode in the xz plane.	65
Figure 2.23 Significantly improved insertion efficiency is detected with 6 periods of PC3 when a_3 is kept at 450 nm.	66
Figure 2.24 (a) 2D schematic of the lateral P ⁺ PNN ⁺ diode embedded in the HLMG cavity. yz cross section of the embedded diode shows (b) indirect carrier depletion path in a rib waveguide based diode (not recommended) and (c) direct depletion path in the planar diode design that we employ instead.....	67
Figure 2.25 (a) Static carrier level near the center of the waveguide shows different hole contrasts at the same bias voltage for diodes embedded in different lattice patterns. 2D hole profiles at -8 V indicate in the x direction (b) highly uniform carrier distribution for the HLMG cavity and (c) periodically modulated concentration for the DHS cavity.....	69
Figure 2.26 (a) A finite breakdown delay time is found in the post breakdown operation regime where the carrier level can be further depleted with increase of the bias voltage. (b) The leakage current is found to be negligible within the breakdown delay and increases drastically after breakdown takes place.	70

Figure 2.27 Magnified 2D hole profiles at -15 V indicate the depletion region (a) in the xy plane and (b) in the yz plane.	73
Figure 2.28 (a) 1D cutline of the hole/electron concentration along the y direction indicates the depletion width movement at -15 V bias. (b) 1D carrier contrast profile between 0 and -15 V within the depletion region.	74
Figure 2.29 (a) The transient carrier response at different locations of the depletion region at -15 V indicates uniform switching speed of 238 GHz. (b) Equivalent RC circuit of the embedded P ⁺ PNN ⁺ diode. (c) Tradeoff relationship between MD and bias voltage among different operation regimes.	76
Figure 2.30 (a) The applied 238 GHz RZ voltage signal switching between 0 and -15 V. (b) The representative hole response at the center of the waveguide. (c) The 3D FDTD interpreted transmission evolution of the HLMG resonator corresponding to (b). (d) The transient current flow of the device at voltage transitions.	77
Figure 3.1 (a) 2D schematic cross section of the device showing the lateral polymer infiltrated P-S-N diode capacitor configuration. (b) The small signal equivalent circuit corresponding to (a) showing the RC limitation of the phase shifter.	88
Figure 3.2 The fundamental mode profile cross section of the RM SWG: (a) TE-like polarization and (b) TM-like polarization. (c) E-field intensity cutlines of the TE-like and TM-like mode profiles in the x direction across the waveguide center, which show a large portion of the total intensity located within the silicon ridges.	91
Figure 3.3 (a) E-field (x component) profile within the nonlinear slot when the diode capacitor is reverse biased. (b) Free carrier (hole) concentration profile within the silicon ridges under the same bias. (c) Localized index perturbation corresponding to (a) via Pockels effect. (d) Localized index perturbation corresponding to a combined effort of hole and electron depletion via free carrier effect (the value below the lower end of the color scale is shown in black).	93
Figure 3.4 (a) Δn_{eff} and $\Delta n_{\text{eff,poly}}$ changes when W_{slot} is varied for both TE- and TM-like polarizations. (b) Change of the intensity fraction within the slot for both polarizations when W_{slot} is swept over the same range.	95
Figure 3.5 The carrier concentration evolution with time indicating a reduced device response time with an increase of W_{slot}	96
Figure 3.6 (a) Δn_{eff} decreases as propagation loss increases with an increase of h_{slab} . (b) The device response time further reduces with an increase of h_{slab}	98
Figure 3.7 (a) Faster response is found for free carriers than E-field due to the reduced transient capacitance. (b) The carrier cutline along the x direction indicating the depletion width shift under reverse bias.	100

Figure 3.8 (a) The tradeoff relationship between bias voltage and phase shift. (b) The RF driving signal with $V_{pp}=10$ V and period of 2.4 ps. (c) The modulated phase shift in response to (b). (d) The transient current flow within the P-S-N diode capacitor in response to (b).....	102
Figure 3.9 Equivalent circuit of the TL loaded with the P-S-N diode capacitor.....	103
Figure 3.10 The walk-off bandwidth (ON and OFF states) reduces with the increase of the polymer index shift from polling effect.	105
Figure 4.1 Schematics of the device fabricated in Chapter 4. (a) 3D schematic of the whole device; (b) 2D schematic of the device showing dopant profile for injection mode operation.	111
Figure 4.2 Aluminum contact pad schematic as it appears in L-Edit design module.	112
Figure 4.3 Completed device layout design using L-Edit: (a) the magnified schematic of a single device that is defined in a multi-layer hierarchy; (b) the view of the whole set of devices with different dimensions for chip layout.....	113
Figure 4.4 The dopant profile in the longitudinal direction after ion implantation and RTA calculation from ATHENA.	116
Figure 4.5 Process flow of the hybrid lattice resonator based modulator. (a) DUV patterning of implantation barrier; (b) boron and phosphorus ion implantation; (c) DUV patterning of waveguide and photonic cavity; (d) RIE etching of waveguide and photonic cavity; (e) PECVD process for top SiO_2 cladding; (f) contact hole patterning; (g) contact hole RIE etching; (h) EBE process for aluminum deposition.....	118
Figure 4.6 (a) SEM image of the completed device (after SiO_2 cladding) showing the light path through the photonic crystal resonator and electrical driving contacts; (b) SEM image of the passive hybrid-lattice resonator and coupling waveguides.	120
Figure 4.7 (a) SEM image of the inverse tap at the end of the coupling waveguide; (b) device top view under high magnification optical microscope for waveguide alignment purposes.....	121
Figure 4.8 (a) Image of the passive nanophotonics measurement setup; (b) Schematic of the optical connection for transmission measurement.	122
Figure 4.9 (a) The full spectrum of the device from 1540 to 1640 nm in dB. The photonic bandgap and slow light phenomenon are apparent from the low transmission and periodic resonances from 1580 to 1640 nm, which matches the numerical results; (b) the transmission is plotted in linear scale and resonance peaks are detected in the PBG.....	124
Figure 4.10 Measured transmission spectrum of the hybrid lattice resonator based modulator (defect lattice period 400 nm) indicates a highly confined resonance mode in the near infrared range with a Q factor around 7800.	124

Figure 4.11 (a) Image of the probe station for I-V measurement; (b) image of the HP 4156A semiconductor parameter analyzer..... 125

Figure 4.12 I-V characteristic of the devices with different design parameters: (a) doping offset changes when the defect period is kept at 400 nm; (b) defect period changes when the doping period is fixed at 0.71 μm 127

LIST OF TABLES

Table 1.1 Summary of the devices studied in this thesis.	3
Table 2.1 Cavity optical confinement and response at different r_c under the voltage bias of 1.65 V.....	60
Table 2.2 Performance summary and comparison between EO modulators studied in Chapter 2.	79
Table 2.3 Detailed device performance comparison between the best device in Chapter 2 and previous work in the literature.	81
Table 3.1 List of the major design parameters in the RM device.	91
Table 3.2 Detailed device performance comparison between the device studied in Section 3.3 and previous works in literature.	109
Table 4.1 Dopant recipe for the injection mode hybrid-lattice resonator based modulator that is fabricated in Chapter 4: (a) P ⁺ region; (b) N ⁺ region.	115
Table 5.1 Summary of the major FOMs of the devices studied in this work.....	130

ACRONYMS

1D	One dimensional
2D	Two dimensional
BDDM	Breakdown delay-based depletion mode
BER	Bit error rate
BPM	Beam propagation method
CMOS	Complementary metal–oxide–semiconductor
CW	Continuous wave
DFT	Discrete Fourier transform
DHS	Double heterostructure
DOC	Dopant concentration
DUV	Deep ultraviolet
DWDM	Dense wavelength division multiplexing
EBE	Electron beam evaporation
EO	Electro-optic
ER	Extinction ratio
FDTD	Finite-difference time-domain
FHA	Fast harmonic analysis
FOM	Figure of merit
FP	Fabry-Perot
FSR	Free spectral range
FTTH	Fiber to the home
FWHM	Full-width half maximum
GBE	Gigabit Ethernet

HDPIC	High density photonic integrated circuits
HLMG	Hybrid-lattice mode gap
IC	Integrated circuit
MD	Modulation depth
MIS	Metal-insulator-semiconductor
MZI	Mach-Zehnder Interferometer
NIR	Near infrared
NLO	Nonlinear optical
NRZ	Non-return-to-zero
OSA	Optical spectrum analyzer
PBG	Photonic bandgap
PC	Photonic crystal
PCW	Photonic crystal waveguide
PECVD	Plasma-enhanced chemical vapour deposition
PIC	Photonic integrated circuit
PMG	Photonic mode gap
PML	Perfectly matched layer
PRBS	Pseudo-random bit sequence
PVD	Physical vapor deposition
PWE	Plane wave expansion
RF	Radio frequency
RI	Refractive index
RIE	Reactive ion etching
RM	Reference model
RR	Ring resonator
RTA	Rapid thermal annealing

SEM	Scanning electron microscope
SNR	Signal-to-noise ratio
SOI	Silicon-on-insulator
SOH	Silicon organic hybrid
SRD	Step recovery diode
SRH	Shockley-Read-Hall
SWG	Slot waveguide
SVDP	SIMS verified dual Pearson
TE	Transverse electric
TIR	Total internal reflection
TL	Transmission line
TLS	Tunable laser source
TM	Transverse magnetic
TPA	Two photon absorption

CHAPTER

1. INTRODUCTION AND MOTIVATION

Generally speaking, the ambition to create photonic devices in silicon originates from the overwhelming success of semiconductor technology in microelectronics, which are better known as integrated circuits (ICs). The advent of complementary metal–oxide–semiconductor (CMOS) transistors facilitated the manipulation of electrons in such an ambidextrous way that an array of useful analog and digital devices has been made possible. Therefore, it is natural that scientists and researchers would seek a reliable way of manipulating photons in a similar way by searching for counterparts in the photonic realm [1]. This vision began to take form when low loss optical propagation was demonstrated in undoped crystalline silicon at infrared wavelengths like 1330 and 1550 nm, and when early experiments on waveguides and electro-optic switches were carried out in the mid 1980s [2, 3]. Since then, a broad spectrum of functional blocks has been proposed and studied based on a silicon foundation to build photonic integrated circuits (PICs).

In particular, high speed silicon modulators are one of the most important applications of silicon photonics to optical communication networks, where ever-increasing demand for optical bandwidth and data transmission capacity is witnessed. To better address future bandwidth intensive applications such as multimedia resource sharing and broadcasting, dense wavelength division multiplexing (DWDM) and gigabit ethernet (GBE) architectures have been proposed. More importantly, on the physical layer, high speed optical modulators with carrier frequencies up to the THz range need to be designed to realize such systems. The commercially available optical modulators nowadays, however, are mostly based on III-V compound semiconductor materials that involve CMOS incompatible processes. As a result, the low cost efficiency of the device-making process imposes obstacles for mass production in terms of integration. In addition, their device footprint and power consumption are still much larger than those of integrated

electronic devices. These concerns significantly limit their application in high density photonic integrated circuits (HDPICs) and on-chip optical interconnects.

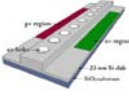
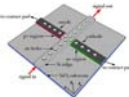
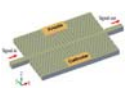
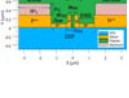
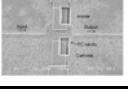
The main scope of this work is to design silicon based high speed optical modulators with ultra-low energy consumption. Silicon is inherently CMOS compatible and conventional electro-optic (EO) modulators with high 3-dB bandwidth are mostly based on Mach-Zehnder interferometer (MZI) configurations. The long interaction length of the two interferometer arms in that structure is the main reason behind relatively large device dimensions and power consumption. To address this concern, in Chapter 2 of this work, various photonic resonance and slow light media have been designed to bypass the large phase interference length via an enhanced nonlinear interaction between optical resonance mode and EO active region. In Section 2.3, various one dimensional (1D) photonic crystal (PC) nanocavities have been applied to conventional silicon waveguides to construct miniaturized silicon EO modulators. High operation bandwidths and competitive energy consumptions are found in the resultant devices. Admittedly, while 1D PC resonators have a very compact device footprint that is highly favorable for low energy consumption and high density integration purposes, this kind of structure is limited by a strict tradeoff between optical confinement and transmitted intensity, which are both highly desired in a high efficiency optical modulator. To alleviate this tradeoff, a two dimensional (2D) PC nanocavity is designed in Section 2.4. The 2D PC nanocavity has an improved in-plane optical confinement due to the presence of a photonic bandgap (PBG), and out of plane confinement from total internal reflection (TIR). At the same time, the dopant profile is modified to facilitate carrier depletion mode operation instead of injection mode operation. As a result, both 3-dB operation bandwidths and energy consumptions are further improved significantly compared to 1D PC resonator based approaches.

The device structure studied in Section 2.4 is pushing the upper physical limit of modulation speed for carrier movement based approaches, since the device configuration is optimized both optically and electrically. To further improve device speed, a polymer MZI based phase shifter is studied in Section 3.3 which incorporates two different nonlinear effects: free carrier effect and Pockels effect. The phase

modulation efficiency of the device is therefore significantly improved by an increased EO overlapped volume. Moreover, low aspect ratio slot waveguide geometry is employed to further unleash the almost instantaneous response of Pockels nonlinearity with a reduced RC limitation. At the same time, high energy efficiency of the device is maintained. Regarding device performance, a record high 3-dB bandwidth of 269 GHz is demonstrated numerically with low energy consumption of 5.83 pJ/bit.

Finally, a 2D PC nanocavity based modulator designed in Section 2.4 has been fabricated with an injection mode dopant profile and the process details are described in Section 4.2. The performance of the fabricated device is characterized both optically and electrically in Section 4.3 and 4.4. The measured passive transmission of the resonator indicates strong optical confinement and a resonance condition within near infrared (NIR) communication wavelength, which agrees well with the numerical results presented in the device design. The measured I-V characteristics of the device also show a high level

Table 1.1 Summary of the devices studied in this thesis.

Device thumbnail	Section	Photonic medium	EO active medium	Operation mode	Nature of study	Advantages	Disadvantages
	2.3.1	Fabry-Perot resonator	Free carrier	Injection	Design, simulation	Compactness, small bias voltage	Low speed, high energy consumption, low optical transmission
	2.3.2	Cross waveguide resonator	Free carrier	Injection	Design, simulation	Compactness, small bias voltage	Low speed, high energy consumption, low optical transmission
	2.4	Hybrid lattice mode gap resonator	Free carrier	Breakdown	Design, simulation	Compactness, high speed, low energy consumption	Low optical transmission, less compact footprint, large bias voltage
	3.3	MZI	Free carrier & Pockels polymer	Reverse bias	Design, simulation	High speed, low energy consumption, high optical transmission	Large footprint, large bias voltage
	Chapter 4	Hybrid lattice mode gap resonator	Free carrier	Injection	Design, simulation, fabrication, & measurement	Compactness, small bias voltage	Low speed, low optical transmission

agreement with simulations. A summary of all the devices studied within the scope of this thesis is given in Tab. 1.1.

The rest of the chapter is organized as follows. In Section 1.1, fundamental information on the working mechanism of modulators is given for optical signal processing applications. Then in Section 1.2, PBG based resonance and slow light media are discussed in detail as a solution for minimizing device dimensions with ultra-low energy consumption. After that, a literature review of historical modulators is carried out in Section 1.3, which covers a wide range of optical and electrical approaches. Finally, the research objectives and an outline of the thesis are provided in Sections 1.4 and 1.5 respectively.

1.1 Introduction to silicon modulators

An optical modulator is a device which is used to modulate a beam of light. In a binary communication system, in particular, an optical switching component is usually used to dynamically control the transmission of light to generate a sequence that consists of '1's and '0's, which is called intensity modulation. All of the devices studied in this work belong to this category and are called optical modulators for short throughout the thesis. Depending on the type of the modulating signal, an optical modulator can be categorized as an EO modulator or an all optical modulator. In an EO modulator, a high frequency voltage/current signal is used to modulate the input optical signal in such a way that the output optical signal follows the modulating voltage/current signal applied. In an all optical modulator, the input optical signal is modulated by another optical signal to achieve the same effect, which is highly favourable to all optical communication networks without involving E-O/O-E conversion units. The focus of this work is mainly on the design of novel EO modulators where the transmission contrast at the output side is achieved by a localized refractive index (RI) perturbation via an EO nonlinear medium. For

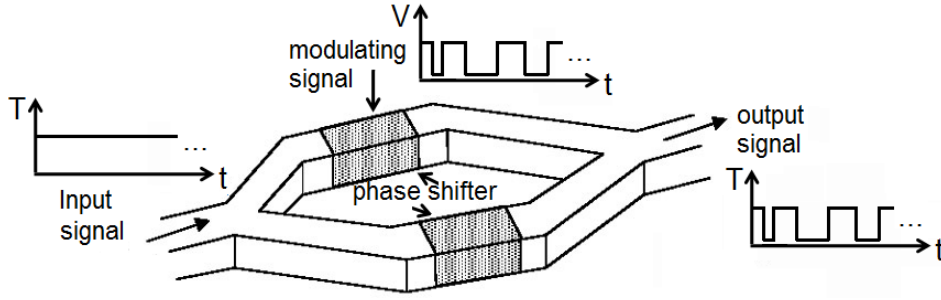


Figure 1.1 An example of an EO modulator which is based on a MZI configuration.

example, an EO modulator is constructed based on a MZI configuration in Fig. 1.1, where a phase shifter is embedded into each arm of the interferometer for push-pull operation. As a result, either constructive or destructive interference can be achieved at the output end when the phase difference between these two arms is either 0 or π . Another way of achieving transmission contrast is by using a photonic resonance medium, where the resonance peak of the resonator/cavity is shifted due to RI perturbation so that the optical signal at the original resonance wavelength is blocked by the peak shift. In this approach, the device dimensions and energy consumption can be significantly reduced due to the enhanced interaction between the EO nonlinear medium and the optical resonance mode (The details will be discussed in Section 1.2).

As one can tell from Fig. 1.1, at the heart of an EO modulator is a high efficiency nonlinear medium for index perturbation. Due to the absence of second order nonlinearity, i.e. Pockels effect, from the centrosymmetric nature of crystalline silicon, the only physically available field effects are the Kerr effect and the Franz-Keldysh effect. The Kerr effect is a third order electric field effect in which the change in real refractive index Δn is proportional to the square of the applied electric field. This effect is present in silicon, although it is relatively weak. The change may be expressed as:

$$\Delta n = s_{33} n_0 \frac{E^2}{2} \quad (1.1)$$

where s_{33} is the Kerr coefficient, n_0 is the unperturbed refractive index, and E is the applied field. In this case, the sign of the refractive index change is not dependent on the direction of the field polarization within the crystal. Soref and Bennett [4] theoretically quantified the refractive index change in silicon at a wavelength of 1.3 μm as a function of the applied electric field. According to their study, the change in refractive index Δn is predicted to reach 10^{-4} at an applied field of 10^6 Vs/cm (100 V/ μm), which is above the breakdown field for lightly doped silicon. Therefore, the effect itself is too weak to be practically viable.

Unlike the Pockels effect and the Kerr effect, the Franz-Keldysh effect gives rise to both electrorefraction and electroabsorption, although primarily the latter. The effect is due to distortion of the energy bands of the semiconductor upon application of an electric field. In effect, this shifts the bandgap energy, resulting in a change in the absorption properties of the crystal, particularly at wavelengths close to the bandgap, and hence a change in the complex refractive index. Soref and Bennett also quantified the changes in refractive index due to the Franz-Keldysh effect. Although noticeable RI change is available at the wavelength of 1.07 μm by an applied electric field, the effect diminishes significantly at the telecommunications wavelengths of 1.31 μm and 1.55 μm , where material loss in silicon reaches a minimum.

Apart from the abovementioned electric field effects; there is also thermal-optic effect in silicon, in which the refractive index of silicon is varied by applying heat to the material. The thermo-optic coefficient in silicon is [4]:

$$\frac{dn}{dT} = 1.86 \times 10^{-4} / K \quad (1.2)$$

Therefore, if the waveguide material can be raised in temperature by approximately 6° C in a controllable manner, a RI change of 1.1×10^{-3} results. There are of course issues about confining the temperature rise to the locality of the waveguide, and of efficiency of the mechanism to deliver the thermal energy.

Assuming efficient heat delivery and precise localized control, the effect is still too slow to achieve GHz level optical modulation.

The above listed effects in silicon prove to be unsuitable for modern design of silicon optical modulators because these effects are either too weak in terms of power efficiency or too slow for high speed modulation purposes. In this light, the only well-acknowledged modulation mechanism in silicon involves the plasma dispersion effect by either optical pumping (two photon absorption, TPA) or electrical pumping (carrier injection, accumulation, and depletion). Soref and Bennett computed the dependence of the change in the refractive index with carrier concentration. They produced expressions relating the refractive index and absorption coefficients changes in silicon due to carrier movement at both 1.3 and 1.55 μm wavelengths, which are now almost universally used for the evaluation of optical modulation in silicon. At $\lambda_0 = 1.55\mu\text{m}$ these expressions are:

$$\begin{aligned}\Delta n &= \Delta n_e + \Delta n_h = -8.8 \times 10^{-22} \Delta n_e - 8.5 \times 10^{-18} (\Delta n_h)^{0.8} \\ \Delta \alpha &= \Delta \alpha_e + \Delta \alpha_h = 8.5 \times 10^{-18} \Delta n_e + 6.0 \times 10^{-18} \Delta n_h\end{aligned}\quad (1.3)$$

Similarly, at $\lambda_0 = 1.3\mu\text{m}$ the relationships are:

$$\begin{aligned}\Delta n &= \Delta n_e + \Delta n_h = -6.2 \times 10^{-22} \Delta n_e - 6.0 \times 10^{-18} (\Delta n_h)^{0.8} \\ \Delta \alpha &= \Delta \alpha_e + \Delta \alpha_h = 6.0 \times 10^{-18} \Delta n_e + 4.0 \times 10^{-18} \Delta n_h\end{aligned}\quad (1.4)$$

It can be calculated that a carrier injection level of the order of $5 \times 10^{17} \text{ cm}^{-3}$ is readily achievable for both electrons and holes. Therefore, if we evaluate the RI change at a wavelength of 1.3 μm (Equation 1.4), for comparison with the field effects evaluated earlier we obtain $\Delta n = -1.17 \times 10^{-3}$. This is more than an order of magnitude larger than the changes due to the electric field effects described earlier. Furthermore, by appropriate high doping of impurity ions to the silicon layer, it is reasonable to expect higher injection levels, and therefore higher refractive index changes. Thus, the free carrier effect is the only practical nonlinear effect for achieving high speed optical modulation in pure silicon.

1.2 Photonic bandgap material based solution

One of the main trends in the development of silicon photonics is ever increasing integration density. Figure 1.2 (a) shows IBM's vision of the development of nanophotonic circuits for high performance computing systems. As one can see, consistent efforts have been devoted to increasing the number of optical channels in silicon CMOS chips. By doing that, the conventional copper connects can be gradually replaced by optical links to leverage the broadband and parallel nature in optical processing with wavelength division multiplexing. In Fig. 1.2 (b), for example, the communication between two

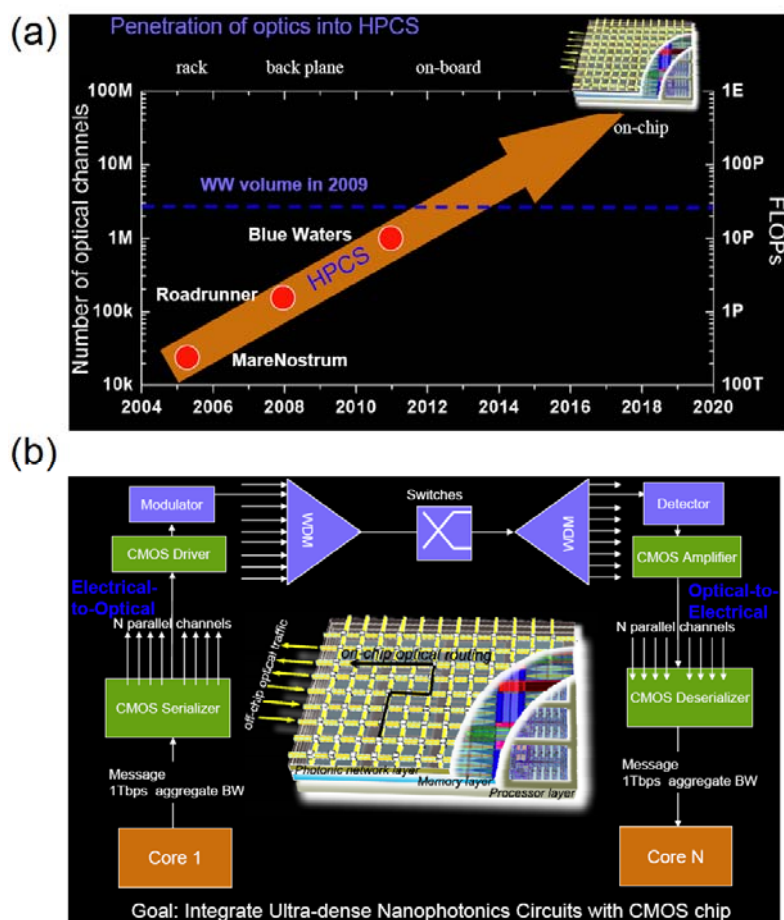


Figure 1.2 (a) IBM's view for development of high performance computing systems; (b) an example optical channel connecting two computation cores (Courtesy of IBM TJ Watson Research Center).

remotely located computation cores can be expedited by optical means with wavelength division multiplexers in the middle and E-O/O-E conversion units at the two ends. At the heart of the circuit is a high bit rate optical modulator that encodes the baseband signal onto the optical carrier, which also determines the bandwidth of the optical link and therefore the speed of computation. As a result, it is important to develop compact high speed modulators that consume ultra-low energy for high density integration purposes.

As we know from a physical perspective, the dimensions of photonic devices are proportional to the material wavelength of the operation light source λ_0/n , where λ_0 is free space wavelength of the light source and for homogenous materials, n is the refractive index at λ_0 . For conventional material systems, the refractive index range is quite limited and therefore, the device size needs to be large enough for necessary nonlinear optical interaction. One solution to this is to employ PBG materials where the speed of light (group velocity) can be significantly slowed down. As a result, the nonlinear interaction between the guided mode and EO active medium can be enhanced.

Perfect or defect PC lattices are an important approach to slow light phenomenon. In 1994, Meade et al. [5] first proposed the concept of utilizing PCs with PBGs as waveguides for optical interconnection by introducing a line defect, shown in Fig. 1.3 (a). Soon after that, they also showed [6] that highly efficient transmission of light can indeed be achieved through sharp corners in waveguides created by taking one row away in square arrays of infinitely long dielectric rods with a refractive index of 3.4, wherein 100% transmission through sharp bends was shown at several frequencies, Fig. 1.3 (b). The guided optical mode is strongly confined within the defect line due to the fact that its frequency lies within the photonic bandgap of the PC lattices on the two sides. Unlike conventional rib/ridge waveguides, the photonic crystal waveguides (PCWs) enable slow light phenomenon where a then-record low group velocity of $c/1000$ was achieved by H. Gersen et al. in 2005 [7]. For intensity modulation purposes, the slow light PCWs can be embedded in the two arms of a MZI configuration described above to realize phase interference.

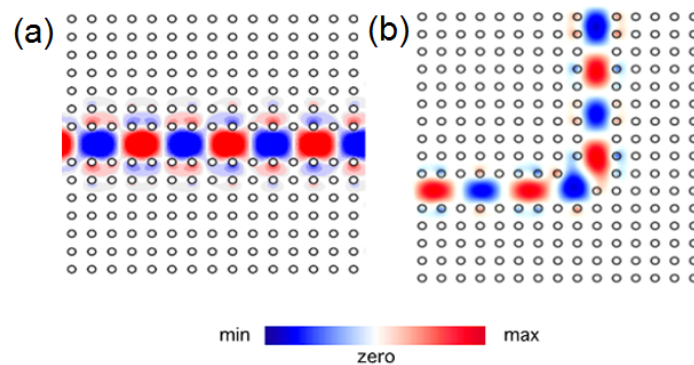


Figure 1.3 Illustration of the idea of (a) a line defect photonic crystal waveguide and (b) a 90 degree bend with theoretically 100% transmission [6].

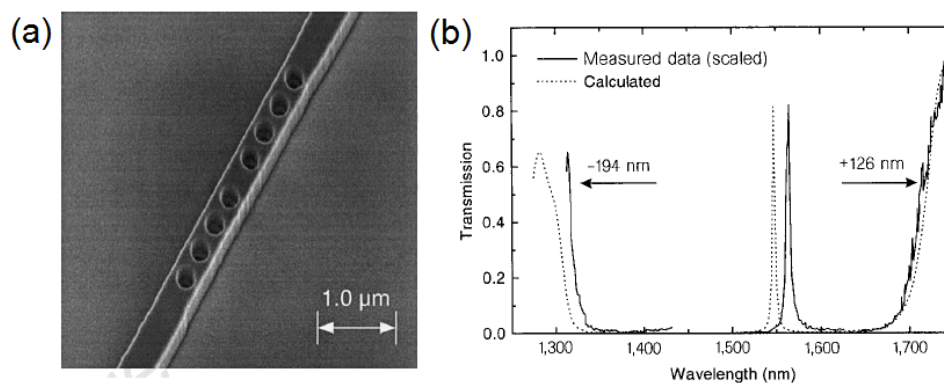


Figure 1.4 A Fabry-Perot microcavity built on a silicon layer [8]: (a) scanning electron microscope (SEM) image of the structure; (b) measured and calculated transmission spectrum of the structure shown in (a).

Another way of enhancing nonlinear interaction is to employ photonic microcavities. The concept of PC microcavities was first proposed by Yablonovitch and Gmitter [9], where they pointed out that if a perfect 3D periodicity is broken by a local defect, local electromagnetic modes can occur within its PBG. Figure 1.4 shows a classic Fabry-Perot (FP) microcavity and its transmission spectrum by J. S. Foresi et al. in 1997 [8], which is among the most compact ways of constructing a photonic resonance medium by PCs. An intensity modulator can therefore be configured through a resonance peak shift due to localized index perturbation, which prohibits the light at the original resonance wavelength from propagation.

1.3 Historical Modulators

Previous work on silicon integrated EO modulators is reviewed in this section [10]. The design philosophy of an integrated EO modulator can be summarized in the diagram shown in Fig. 1.5, where major figures-of-merit (FOM) of the device are listed. Different approaches to the same problem may in turn result in different tradeoff relationships between the major FOMs. In particular, four major categories of approaches are reviewed with representative devices in four independent sections, including silicon waveguide MZI, silicon photonic resonator, polymer waveguide MZI, and finally polymer photonic resonator. Each category has its own strengths and weaknesses, and therefore finds usefulness in its own areas of application.

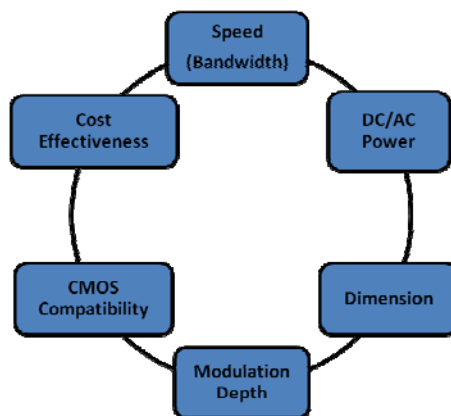


Figure 1.5 Design philosophy of an integrated EO modulator.

1.3.1. Silicon waveguide MZI based devices

Recent research work on silicon MZI modulators can be traced back to 2004 when a research group lead by A. Liu from Intel studied a MOS capacitor based device with modulation bandwidth exceeding 1 GHz [11]. Three years later, the same group announced the world's first 40 Gbps silicon electro-optic modulator [12, 13], Fig. 1.6 (a). The device is based on the waveguide MZI configuration. A

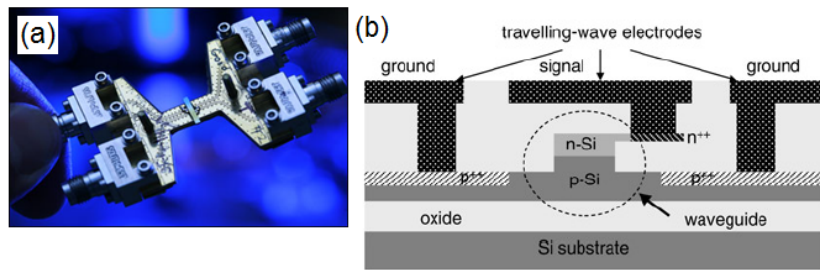


Figure 1.6 Intel's 40 Gbps silicon modulator [12]: (a) Image of the completed device within the package; (b) cross sectional schematic of the phase shifter embedded in one of the two arms.

phase shifter is embedded into one of the two arms, where free carriers of electrons and holes are pulled out from the central p^+ doped silicon active region to change the localized refractive index (both real and imaginary parts) due to the free carrier effect, Fig. 1.6 (b). As a result, the effective index of the guided mode can be changed by reverse biasing one of the two arms to cause π phase difference from the other at the output side of the waveguide. Finally, either constructive or destructive interference is achieved in the modulated optical signal.

The whole device is based on a silicon-on-insulator (SOI) wafer and all the fabrication steps are completely CMOS compatible. Figure 1.7 (a) shows the normalized frequency response data for two modulators, one with a surface mount termination resistor and the other with an on-chip TiN resistor. In both cases, the termination resistance used is $\sim 14 \Omega$, and the resulting 3 dB roll-off frequency is ~ 30 GHz. With the optimal termination resistance of 14Ω , a clearly open optical eye diagram at a bit rate of 40 Gbit/s is obtained, as shown in Fig. 1.7 (b). The measured extinction ratio (ER) of the optical eye is 1.1 dB, given the 4 V/cm phase efficiency of the device and that $> 35\%$ of the drive voltage is lost owing to the driver-modulator ($50\text{--}20 \Omega$) impedance mismatch.

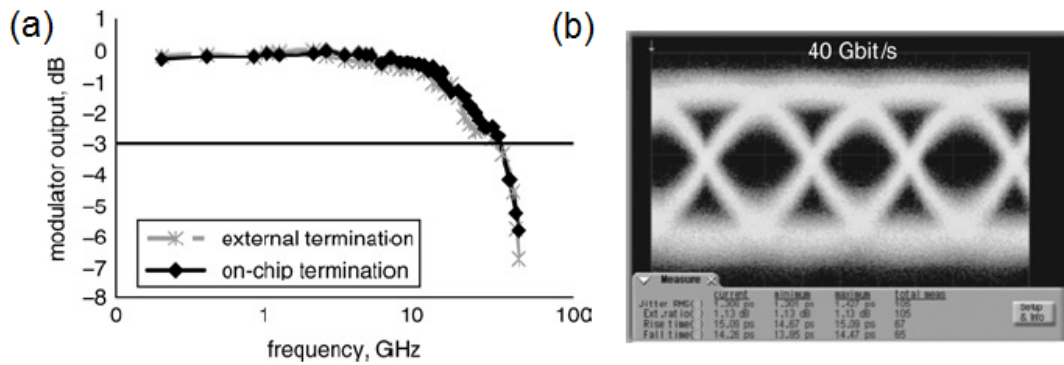


Figure 1.7 Device performance of Intel’s 40 Gbps silicon modulator [12]: (a) normalized optical response of two MZI modulators against RF frequency; (b) optical eye diagram of MZI modulator (shows data transmission at 40 Gbit/s)

The dynamic performance of the device is measured as optical 3-dB roll-off frequency. The signal generator is swept from 100 MHz to 40 GHz, and the photo-receiver output is normalized by the input drive voltage for all frequencies to obtain frequency response. As shown in Fig. 1.7 (b), the MZI modulator has a 3-dB roll-off frequency of ~20 GHz for the 1 mm long phase shifter.

More recently, Feng et al. proposed a lateral P⁺-P-N-N⁺ diode configuration for the phase shifter used in one arm of the MZI [14]. As shown in Fig. 1.8 (a), the highly doped P⁺/N⁺ region is designed to form low resistance driving terminals for the central P-N junction, where the P region is extended partially into the N region to take advantage of the higher free carrier coefficient of holes. The operation mechanism is based on the similar carrier depletion mode discussed in the previous device. The phase modulation efficiency is measured to be 1.4 V·cm, which is an improvement from the Intel’s structure. The 3-dB bandwidth from the dynamic optical response is measured to be 12 GHz for the 1 mm long device and 30 GHz for the 0.25 mm one.

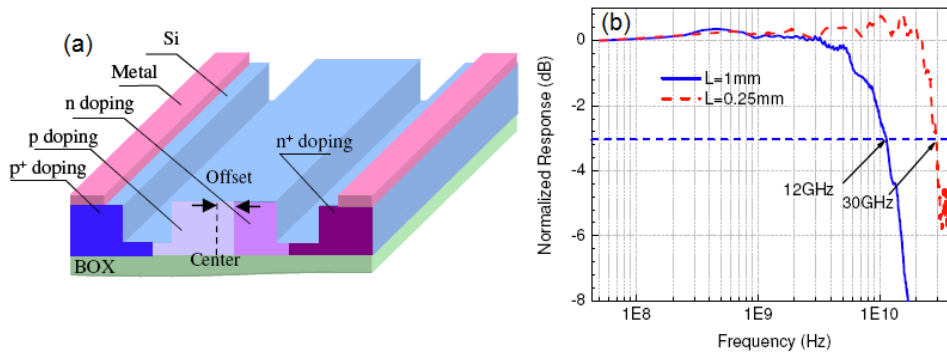


Figure 1.8 (a) 3D schematic of the lateral P+-P-N-N+ diode embedded in the phase shifter; (b) dynamic optical response of the devices with 1 mm and 0.25 mm phase shifters [14].

Apart from these works, a three terminal vertical P-N junction structure was studied by Png et al. in 2004 [15]. Barrios et al. proposed a MOS capacitor based phase shifter in the same year [16] and a multi-silicon on insulator structure in 2006 [17]. Gardes et al. investigated a vertical P-I-N diode structure in 2005 [18]. In 2007, Green et al. from IBM demonstrated 10 Gbps modulation in P-I-N diode based on carrier injection [19]. In the same year, Gu et al. incorporated photonic crystal slow light medium into the MZI structure and reduced the interaction length to 80 μm [20]. Later on, 10 GHz operation speed was also demonstrated by Morini et al. in a P-doped slit embedded P-I-N diode in 2008 [21]. Watts et al. studied a vertical P-N junction based depletion mode modulator in 2010 [22] with 1 V $\cdot\text{cm}$ efficiency at the same speed.

1.3.2. Silicon photonic resonator based devices

As we discussed in the previous section, conventional MZI based optical modulators are capable of a high modulation speed up to 40 Gbps with an acceptable extinction ratio and optical loss. However, the device dimensions and power consumption are still much higher than state-of-the-art CMOS electronic devices. To address this concern, research attention has been focused on photonic microcavities

that have strong temporal and spatial confinement for the optical mode and therefore the interaction between optical signal and nonlinear medium can be significantly enhanced.

In early 2005, Xu et al. first proposed and studied experimentally the well-known microring resonator structure [23] and achieved 12.5 GHz optical modulation in 2007 with carrier injection mode operation [24]. As shown in Fig. 1.9, it consists of a ring resonator with a radius of 5 μm , where a P-I-N junction diode is embedded in and side-coupled to a waveguide. The waveguide and the ring are formed by silicon strips with a height of 200 nm and a width of 450 nm on top of a 50-nm-thick slab layer. The distance between the ring and the straight waveguide is ~ 200 nm. Also from Fig. 1.9, a large resonance peak shift is found in the transmission spectrum when the device is forward biased with a 1.8 V DC voltage where the DC current is measured to be 58 μA .

The dynamic performance of the device is demonstrated with a pre-emphasized non-return-to-zero (NRZ) signal using a low-repetition-rate square-wave signal at the bit-rate of 12.5 Gbit/s. The blue and green lines in Fig. 1.10 (a) show the waveform of the modulated optical output power obtained with a 30-GHz detector. It is shown by adding a pre-emphasis at the transition edges (the red line), the output

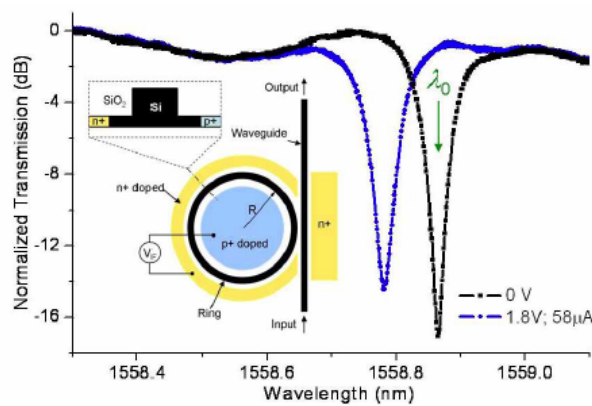


Figure 1.9 Normalized transmission spectra of the modulator along with a schematic of the device structure (inset) [24].

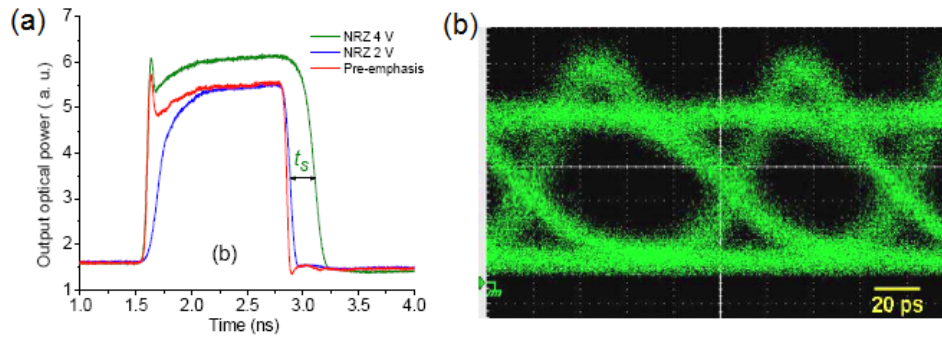


Figure 1.10 (a) The output optical power when the modulator is driven normal and pre-emphasized NRZ signals; (b) eye-diagrams of the modulated optical output at 12.5 Gbit/s with PRBS 210-1 [24].

optical signal has both short rise time and short charge-storage time, allowing for high-bit-rate operation. Then, a pseudo-random bit sequence (PRBS $2^{10}-1$) at 12.5 Gbit/s is composed of a NRZ signal with $V_{pp} \sim 8V$ and pre-emphasis pulses with height $\sim 4V$ at each transition edge. The eye-diagram of the output optical signal is shown in Fig. 2.6 (b), where the extinction ratio of the modulated signal is ~ 9 dB.

Apart from the abovementioned work, Schmidt et al. studied a compact EO modulator that is based on a FP microcavity in 2007 [25]. In 2008, Watts et al. first demonstrated 10 Gbps modulation in a vertical P-N junction based microdisk resonator [26]. Dong et al. and Gardes et al. demonstrated 11 GHz and 19 GHz 3-dB bandwidth optical modulation based on a lateral P^+P-N-N^+ diode embedded ring resonator in 2009 [27, 28]. In the same year, Xu proposed and studied a dual-ring resonator structure and theoretically predicted >40 Gbit/s modulation capacity of the structure [29].

1.3.3. Polymer waveguide MZI based devices

More recently, electro-optic organic materials, especially nonlinear optical (NLO) polymers, have attracted increased research attention for realizing high speed integrated optical modulators due to their strong nonlinear coefficients and instantaneous response to electrical field (E-field) [30]. As a result, the

so-called silicon organic hybrid (SOH) is considered to be a promising platform to provide process and application compatibility with well developed CMOS technology.

As a representative figure in this field, Leuthold et al. proposed and studied several configurations that involve the implementation of the SOH platform [31]. In Fig. 1.11, the first two implementations are based on the modified MZI configuration realized in a conventional SOI system, where nonlinear polymers are incorporated into one of the arms to introduce π phase difference between the two arms depending on the strong nonlinear Pockels field effect. In the second implementation, in particular, the strong optical confinement within the nanoslot of the slot waveguide significantly improves EO overlapped volume from the first approach and therefore the modulation efficiency. The third approach, on the other hand, is based on the slow light MZI configuration where PC lattices are embedded for

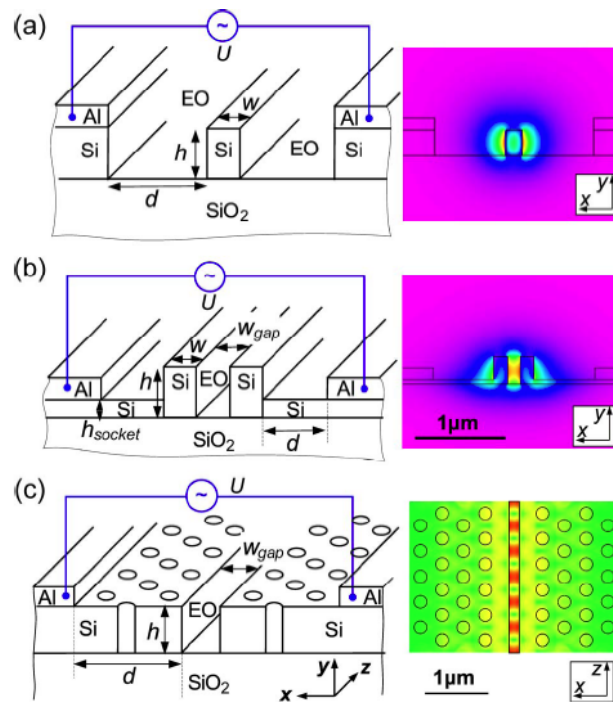


Figure 1.11 Three implementations of silicon organic hybrid electro-optic modulators proposed by Leuthold's group with electric field magnitudes depicted on the right-hand side [31]: (a) traveling-wave strip waveguide structure; (b) traveling wave slot waveguide structure; (c) photonic crystal slot waveguide structure.

photonic bandedge operation. Similar to the pure silicon based design, this configuration can reduce significantly the interaction length for π phase shift. The modulation speed of this kind of modulator is determined by both electrical RC limitation and walk-off limitation, which is formulated in Eq. 1.5, where R and C are the small signal equivalent resistance and capacitance of the slot waveguide respectively. L is the length of the phase shifter while $v_{g,opt}$ and $v_{g,el}$ are the group velocity of the optical signal and electrical RF signal respectively. Assuming perfect phase match both the optical and electrical traveling wave, the upper limit of the device speed will depend only on the RC limitation. Leuthold et al. predicted optical modulators with drive voltage around 1 V and bandwidths exceeding 100 Gbit/s based on the platform proposed.

$$\begin{aligned}
 f_{RC,3dB} &= \frac{1}{4\pi RC} \\
 f_{walkoff,3dB} &= \frac{0.5}{L} \frac{1}{\left| 1/v_{g,opt} \mp 1/v_{g,el} \right|}
 \end{aligned} \tag{1.5}$$

Ding et al. designed and fabricated the “strip-loaded” slot waveguide based polymer EO modulator [32]. As shown in Fig. 1.12 (a), a thin silicon strip is used to make electrical contact from the metal pad to each arm of the slot waveguide. Conservative 10 μm spacing between metal and waveguide was used to allow for fabrication error and avoid excess optical loss. For the frequency range from 200 Hz to 100 MHz, a function generator was used to drive the modulator with a sinusoidal signal with V_{pp} voltage of 2 V. In Fig. 1.12 (b), a 6 dB roll-off point at around 3 GHz is found in the optical response (the 6-dB roll-off point in this case is equivalent to the conventionally defined 3-dB bandwidth in literature).

Major achievements in this field by others should also be mentioned. Early in 2004, Almeida et al. laid the foundation of confining light in void nanostructure [33], which later became one of the most popular photonic media for switching light with nonlinear polymers. In 2006, terahertz (THz) all-optical

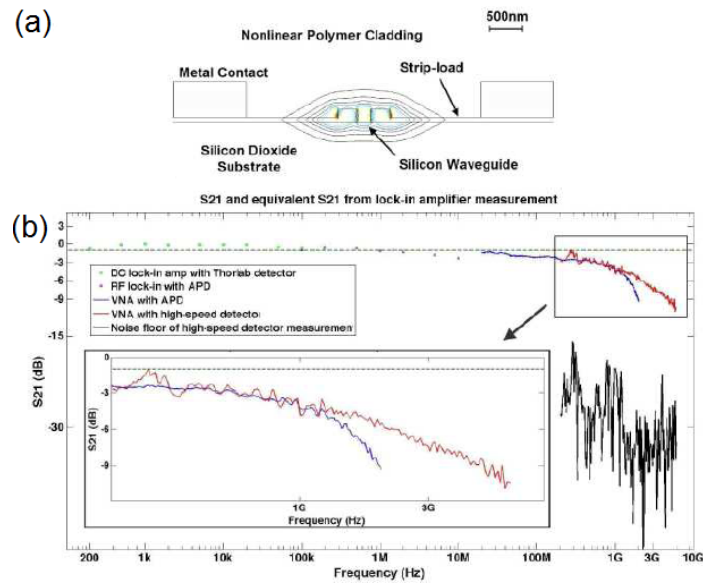


Figure 1.12 (a) Device schematic of the polymer based silicon slot waveguide modulator; (b) S_{21} response of the device at high frequency operation [32].

modulation was demonstrated by Hochberg et al [34]. Hybrid polymer/sol-gel waveguide modulators were studied in 2007 by Enami et al [35]. In 2008, a first principle method was proposed by Robinson et al. to derive gain factor in a high contrast slot waveguide structure [36]. In the same year, Brosi et al. proposed a photonic crystal waveguide embedded MZI structure [37], where in each waveguide arm, a polymer slot is introduced for nonlinear manipulation. Later in 2009, Koos et al. demonstrated all-optical demultiplexing of 170.8 Gb/s data rate in a SOH based silicon slot waveguide modulator [38]. Then in 2010, a polymer infiltrated photonic crystal slot waveguide was demonstrated with 23 dB slow light enhancement by Lin et al. [39].

1.3.4. Polymer photonic resonator based devices

As one of the latest trends in this field, polymer infiltrated photonic resonators have also been studied for optical modulation purposes. At the point of this writing, the experimentally demonstrated

device speeds and bandwidths are much lower than those of the previous three categories of silicon EO modulators, primarily due to practical limitations in device fabrication, parasitic RC limitation, and experimental setup. However, in the long run, sub-THz operation speed can be expected by this approach with negligible energy consumption and miniaturized device footprint.

To begin with, Wulbern et al. proposed a slotted heterostructure resonator for polymer based optical modulation [40], shown in Fig. 1.13 (a). The heterostructure is formed by joining PC waveguides with slightly different lattice constants. The cavity section (PC1) has a larger lattice constant compared to the reflector section (PC2). By creating a heterostructure cavity using a slotted PC waveguide filled with a nonlinear optical polymer, it is possible to shift the position of the resonance peak in the frequency spectrum via modulation of the refractive index of the NLO polymer by means of an external electric field. Later, the same group fabricated their designed structure in Fig. 1.13 (b). According to the measured results in Fig. 1.14, a Q factor of 2600 is experimentally demonstrated in the polymer heterostructure resonator [41]. The passive transmission and EO-modulation spectrum are shown as evidence of the modulation performance achieved.

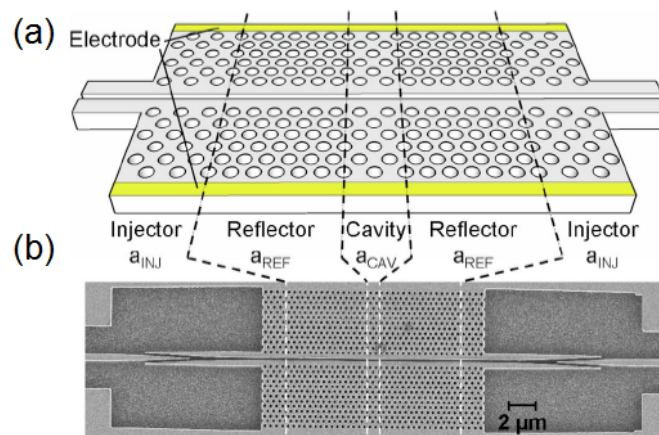


Figure 1.13 The polymer based slotted heterostructure resonator for optical modulation: (a) the 3D schematic of the device layout; (b) the SEM image of the fabricated device [40, 41].

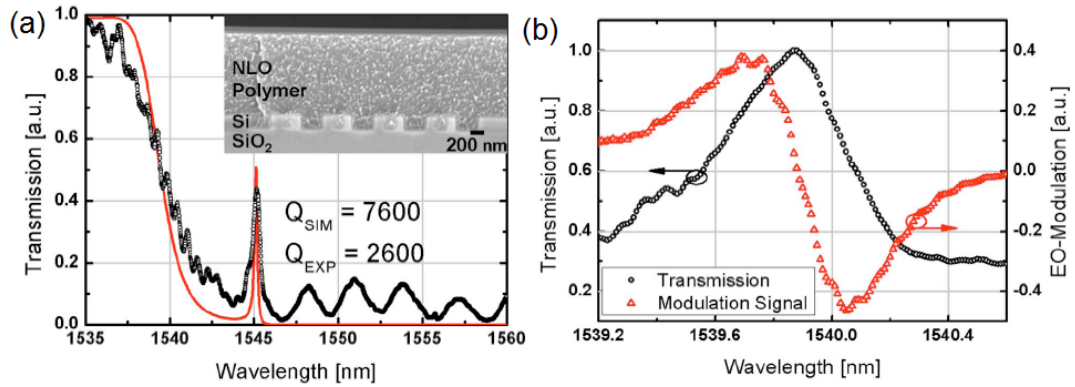


Figure 1.14 (a) Calculated and experimental transmission spectra of the device (inset shows the SEM image of the polymer infiltrated PC lattice); (b) spectral transmission and modulation response after polymer infiltration and poling [41].

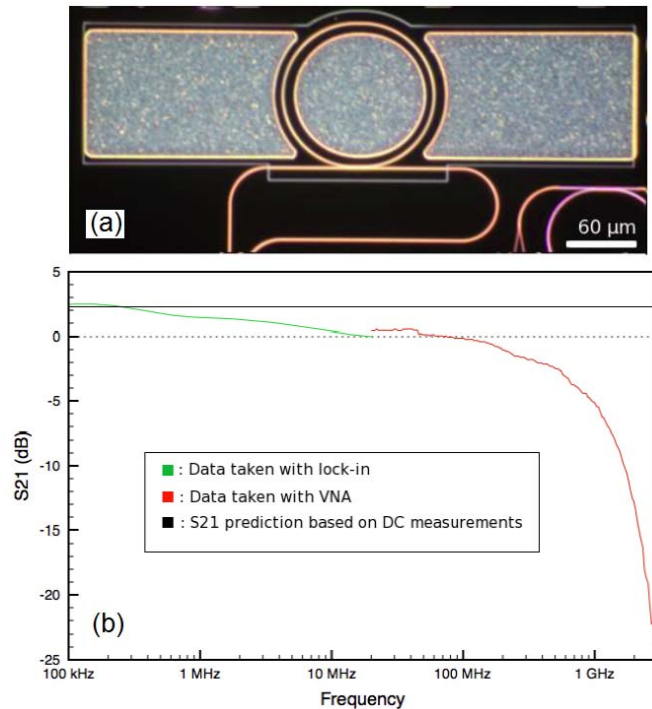


Figure 1.15 (a) Dark field optical micrograph of the device; (b) measured normalized S_{21} spectrum for dynamic performance demonstration [42].

Just a few months before this writing, a polymer ring resonator based approach was studied by Gould et al. [42]. The geometry of the strip-loaded slot waveguide consists of 230 nm wide arms 200 nm wide slot. A ring resonator constructed out of this waveguide with a bend radius of 60 μm is shown in Fig.

1.15 (a) as well as a passive wavelength sweep through the device and grating couplers for coupling on and off chip. Figure 1.15 (b) displays the S_{21} parameter of the device, where 6 dB roll-off in S_{21} (half-power point in the electro-optic response of the device) was determined to be around 1 GHz.

1.4 Research objectives

The research target in this work is to propose and investigate novel photonic bandgap or resonance media for high speed optical modulation in silicon. The main objective of the work is to design and experimentally demonstrate high speed/3-dB bandwidth optical modulators with compact device footprints and low energy consumption so that they can be useful for HDPICs and green photonics related applications [43]. On the electrical side, novel free carrier/nonlinear field based modulation schemes and configurations will also be investigated to further improve device speed and lower energy consumption.

1.5 Outline of the thesis

The outline of the thesis is as follows. In Chapter 2, photonic resonator based EO modulators are discussed, which are first proposed and numerically studied in this work. The photonic resonator can be further categorized into 1D PC and 2D PC based microcavities depending on the complexity of the PC lattices involved. As a result, a detailed design process and numerical results for device performance are given for modulators that are based on FP resonators, cross waveguide resonators, and hybrid-lattice resonators. The background information on the optical and electrical numerical methods, including finite-difference time-domain (FDTD), plane wave expansion (PWE), and physically-based device simulation, is also included. Apart from that, semiconductor process simulation is discussed mainly for ion implantation and rapid thermal annealing (RTA) purposes.

In Chapter 3, the waveguide MZI based EO modulators (phase shifters) studied in this work are first discussed. A nonlinear polymer is introduced to combine with free carrier movement within a compact waveguide cross section that is configured as a polymer infiltrated P-S-N diode capacitor. The device design and performance results are shown to prove higher efficiency of the structure that relies on multiple nonlinear optical effects.

Chapter 4 explains the fabrication process and experimental characterization of the hybrid-lattice resonator based modulator that is electrically configured as a P-I-N diode. First, the preliminary designs for high speed electrodes and ion implantation recipe are discussed. Then, the device process flow and technical background of the various semiconductor process steps are explained in detail. After that, both optical and electrical characterizations are studied where high Q factor resonance and I-V characteristics are demonstrated. The DC power consumption of the device is therefore calculated based on the I-V characteristics.

Finally, in Chapter 5, a performance summary and comparison of all the devices studied in this work is given. Also, a brief discussion of future work possibilities is given in the end.

CHAPTER

2. PHOTONIC RESONATOR BASED ELECTRO-OPTICAL MODULATORS

2.1. Introduction

To miniaturize device footprint, photonic resonators can be used as an approach to compact electro-optic modulation in silicon. The working mechanism of a photonic resonator based EO modulator can be explained by the example shown in Fig. 2.1. Supposing a broad band optical signal is launched to the input side of the modulator, a resonance peak can be found in the output signal. By applying an alternating bias voltage as the modulating signal, free carrier movement can be facilitated within the active region where localized index perturbation can be achieved from the free carrier effect. As a result, the resonance peak of the output signal shifts. Therefore, for a monochromatic light source with an OFF state resonance wavelength, it will be prohibited from propagating through the resonator when the device is at the ON state since it is off resonance, and vice versa. Hence, a transmission contrast can be achieved.

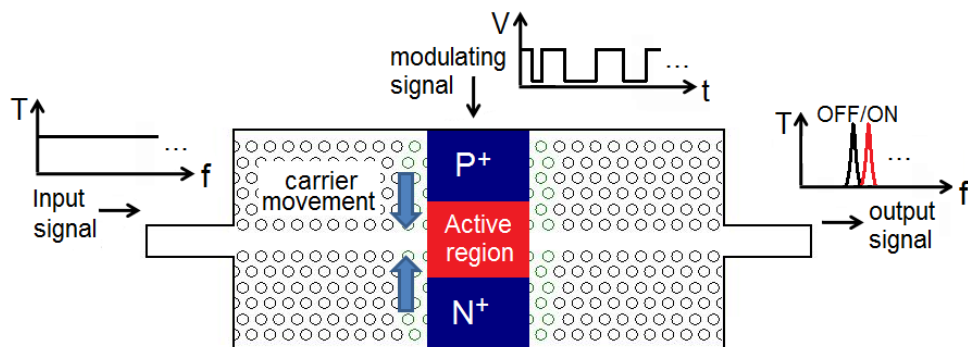


Figure 2.1 Illustration of the active region of an injection mode modulator where the resonance peak shifts due to the free carrier effect.

Due to the slow light enhancement of the interaction between optical resonance mode and the EO active medium, the device dimension as well as energy consumption can therefore be significantly reduced. To be more specific, for a device given cross section, the change in the refractive index of the cavity can be approximated as [25]

$$\Delta n_{cav} \propto \frac{P}{A \cdot L} \quad (2.1)$$

where P is the power required to maintain a certain number of steady-state absolute carriers in a given geometry, which is directly related to the length L of the device at a certain carrier concentration for a given cross-sectional area A . The approximate modulation depth MD is then given by [25]

$$MD \propto \frac{\Delta \lambda_c}{\delta \lambda_{FWHM}} \propto \frac{Q \cdot P}{A \cdot L} \quad (2.2)$$

where $\Delta \lambda_c$ is the absolute shift of the resonance peak, and $\delta \lambda_{FWHM}$ is the full-width half-maximum of the resonance, which is a measure of the bandwidth of the device. Q is the quality factor of the resonator. This proportionality does not include the shape of the resonance, which would determine the exact value of the modulation depth.

A FOM for these modulators is the total amount of bandwidth desired at a certain modulation depth, and the power required to do so. Noting that the modulation depth is proportional to Q , while the bandwidth is inversely proportional to Q , the figure of merit of the device can be expressed in the following equation:

$$FOM = \frac{MD \times Bandwidth}{Power} \propto \frac{1}{V_{eff}} \quad (2.3)$$

where V_{eff} is the effective volume of the refractive index changing cavity region, which is simply $A \cdot L$.

Therefore this figure of merit improves as $1/V_{eff}$.

In short, the device performance can be improved by increasing the Q factor and/or decreasing the modal volume of the resonator. However as a trade-off, the carrier lifetime also increases with Q factor in the following relationship

$$\tau_{ph} = Q/\omega_0 \quad (2.4)$$

where ω_0 is the resonance frequency. Therefore, as a rule of thumb, the quality factor of a practically useful resonator should be capped at $\sim 10^4$ for sub-THz modulation speed in near infrared regime so that the photon lifetime will not be the bottleneck for device speed.

The rest of this chapter is organized as follows. In Section 2.2, the optical and electrical numerical methods for 3D modeling of PC resonator based modulators are discussed. After that, FP resonator, cross waveguide resonator, and hybrid lattice resonator based approaches are explained in detail in Sections 2.3.1, 2.3.2, and 2.4 respectively. A continuous improvement of the device performance, especially in terms of modulation speed and energy consumption, is found by employing a more sophisticated PC cavity design. Finally, performance summary and comparison are made both between the devices studied in this chapter and between the best device and previous works in literature.

2.2. Numerical methods and techniques

In this section, we describe the theoretical background and numerical procedures that have been used in the design of photonic resonator based EO modulators. Generally, the numerical methods consist of two parts: optical and electrical. For the optical part, the FDTD method is used to predict transmission spectrum and resonance peak of the photonic resonator. Based on that, the resonance peak shift of the resonator can be detected to further calculate transmission contrast between OFF and ON states. Moreover, in Section 2.4, the PWE method is used to calculate band diagram of PC lattices with and without defects. As a result, a mode gap can be detected in the hybrid lattice resonator (Section 2.4.1).

On the electrical side, a physically-based device simulator from SILVACO [44] is used to predict static (DC) and dynamic (AC) free carrier (electrons and holes) movement and distribution within the EO active region of the modulator such as the example device shown in Fig. 2.1. The simulator solves the Poisson and continuity equations with appropriate modeling for carrier statistics, mobilities, recombination rates, and carrier lifetimes [45]. Also, major physical phenomena regarding the reverse bias operation, such as bandgap narrowing, band-to-band tunneling, and Selberherr impact ionization [46], are included in both DC and AC simulations. The free carrier profile is then interpreted into the corresponding refractive index profile by Drude-Lorenz model. After that, the index profile is loaded into the FDTD simulator [47] after format conversion so that the optical transmission reflects exactly the localized index perturbation at the device active region under external voltage bias. Finally, both DC and AC currents flow throughout the device are monitored to predict total energy consumption of the device under various bias conditions.

2.2.1. Finite-difference time-domain method

Firstly, the FDTD method [48] is one of the most popular numerical methods used in photonic component design because it provides a rigorous solution to Maxwell's equations. The fundamentals of the FDTD algorithm can be illustrated as follows. Imagine a region of space which contains no flowing currents or isolated charges. Maxwell's curl equations can be written in Cartesian coordinates as six simple scalar equations. Two examples are:

$$\begin{aligned}\frac{\partial H_x}{\partial t} &= -\frac{1}{\mu} \left(\frac{\partial E_y}{\partial z} - \frac{\partial E_z}{\partial y} \right) \\ \frac{\partial E_y}{\partial t} &= -\frac{1}{\varepsilon} \left(\frac{\partial H_x}{\partial z} - \frac{\partial H_z}{\partial x} \right)\end{aligned}\tag{2.5}$$

The other four are symmetric equivalents of the above and are obtained by cyclically exchanging the x , y and z subscripts and derivatives. Maxwell's equations describe a situation in which the temporal change in the E field is dependent upon the spatial variation of the H field, and vice versa. The FDTD method solves Maxwell's equations by first discretizing the equations via central differences in time and space and then numerically solving these equations in software. The most common method to solve these equations is based on Yee's mesh [49] and computes the E and H field components at points on a grid with grid points spaced Δx , Δy and Δz apart. The E and the H field components are then interlaced in all three spatial dimensions as shown in Fig. 2.2. Furthermore, time is broken up into discrete steps of integer spacing representing the computing step. For example, the E field at a time $t=n\Delta t$ is equal to the E field at $t=(n-1)\Delta t$ plus an additional term computed from the spatial variation, or curl, of the H field at time t .

This method results in six equations that can be used to compute the field at a given mesh point, denoted by integers i, j, k . For example, two of the six are:

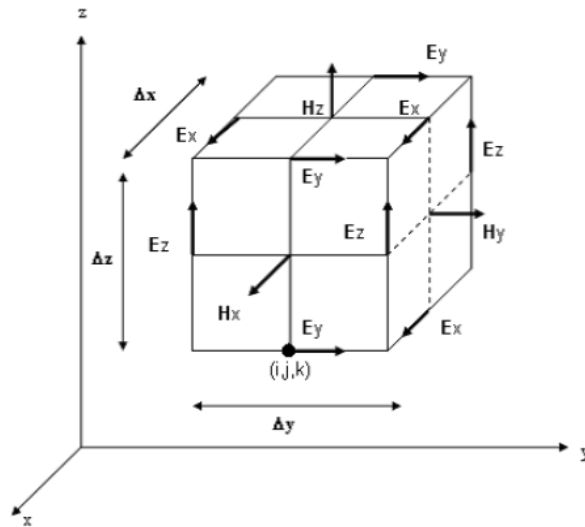


Figure 2.2 In a Yee cell of dimension $\Delta x, \Delta y, \Delta z$, where the H field is computed at points shifted one-half grid spacing from the E field grid points [49].

$$\begin{aligned}
H_{x(i,j,k)}^{n+1/2} &= H_{x(i,j,k)}^{n-1/2} + \frac{\Delta t}{\mu \Delta z} (E_{y(i,j,k)}^n - E_{y(i,j,k-1)}^n) - \frac{\Delta t}{\mu \Delta y} (E_{z(i,j,k)}^n - E_{z(i,j-1,k)}^n) \\
E_{x(i,j,k)}^{n+1} &= E_{x(i,j,k)}^n + \frac{\Delta t}{\varepsilon \Delta y} (H_{z(i,j,k)}^{n+1/2} - H_{z(i,j,k)}^{n-1/2}) - \frac{\Delta t}{\varepsilon \Delta z} (H_{y(i,j,k+1)}^{n+1/2} - H_{y(i,j,k)}^{n+1/2})
\end{aligned} \tag{2.6}$$

These equations are iteratively solved in a leapfrog manner, alternating between computing the E and H fields at subsequent $\Delta t/2$ intervals.

In order to implement FDTD simulators in photonic components design, both physical and numerical parameters are required. The former comes down to two major ones:

- The material parameters, including the relative permittivity $\varepsilon(\mathbf{r}, \omega)$ and relative permeability $\mu(\mathbf{r}, \omega)$ as a function of space \mathbf{r} and/or frequency ω , where \mathbf{r} is the position vector in Cartesian coordinates.
- The electromagnetic field excitation.

The material parameters should be specified in the following two scalar equations, which is appropriate in silicon since it is isotropic:

$$\begin{aligned}
D &= \varepsilon_0 E + P \\
B &= \mu_0 H + M
\end{aligned} \tag{2.7}$$

where

$$\begin{aligned}
\mathbf{P} &= \varepsilon_0 \left[\chi(\omega) \mathbf{E} + \chi^2(\omega) \mathbf{E}^2 + \chi^3(\omega) \frac{I}{1 + c_{sat} I} \mathbf{E}^3 \right] \\
\mathbf{M} &= \mu_0 \left[\chi_m(\omega) \mathbf{H} + \chi_m^2(\omega) \mathbf{H}^2 + \chi_m^3(\omega) \frac{I}{1 + d_{sat} I} \mathbf{H}^3 \right]
\end{aligned} \tag{2.8}$$

Equations (2.7) have four terms each after substituting Equations (2.8), each of which corresponds to a different effect. The first and second terms together are linear index and dispersion. The third term and fourth term in these equations are non-linear terms, and correspond to second order non-linearity and frequency-dependent third-order non-linearity.

Apart from that, in order to perform a simulation, an initial launch condition ϕ_L at $t=0$ is needed, as well as a driving function in time. This consists of both a spatial and temporal excitation, such as

$$\phi_L(\mathbf{r}, t) = f(\mathbf{r}_0)g(t) \quad (2.9)$$

where $f(\mathbf{r}_0)$ is the spatial excitation at the launch plane and $g(t)$ is the temporal excitation. The excitations can be classified into slab mode, fiber mode, Gaussian, rectangular and multimode in terms of spatial field profile; and continuous wave (CW), pulse and impulse in terms of temporal distribution.

There are also a bunch of numerical parameters to be specified in order to get the exact simulation results that are needed. They are listed as:

- A finite computational domain, $\{x \in (x_{\min}, x_{\max})\}, \{y \in (y_{\min}, y_{\max})\}, \{z \in (z_{\min}, z_{\max})\}$.
- The boundary condition(s)
- The spatial grid sizes, Δx , Δy and Δz .
- The temporal grid, or time step, Δt and the length of time for the simulation.

The computation domain should cover the device of interest and leave enough space for the lightwave to radiate away from the structure and be absorbed by perfectly matched layers (PML). The boundary conditions at the spatial edges of the computational domain must be carefully considered. Many simulations employ an absorbing boundary condition that eliminates any outward propagating energy that impinges on the domain boundaries, such as the PML mentioned above, in which both electric and magnetic conductivities are introduced in such a way that the wave impedance remains constant, absorbing the energy without inducing reflections. Periodic boundary conditions, on the other hand, are also important because of their applicability to periodic structures such as PBGs. In these cases, the boundary condition is chosen such that the simulation is equivalent to an infinite structure composed of the basic computational domain repeated endlessly in all dimensions.

In order to produce an accurate simulation, the spatial grid must be small enough to resolve the smallest feature of the field to be simulated. Usually, this is dictated by the wavelength in the materials to be simulated, but in some cases, can be dictated by the geometry of the photonic device. Typically, the grid spacing must be able to resolve the wavelength in time, and therefore usually be less than $\lambda/10$ where λ is not the free space wavelength, but rather the wavelength in the materials. To obtain a stable simulation, one must adhere to the Courant condition which relates the spatial and temporal step size:

$$c\Delta t < \frac{1}{\sqrt{\left(\frac{1}{\Delta x^2} + \frac{1}{\Delta y^2} + \frac{1}{\Delta z^2}\right)}} \quad (2.10)$$

where c is the velocity of light and, for the case of a non-uniform grid, the grid sizes represent the smallest grid size in the simulation.

For example, Fig. 2.3 shows a 3D FDTD layout of the cross waveguide resonator using one of the commercially available simulators [47]. It is shown in Fig. 2.3 (a) that the optical launch (brown bar) is placed inside the waveguide to minimize optical coupling loss and yet kept several lattice constants away

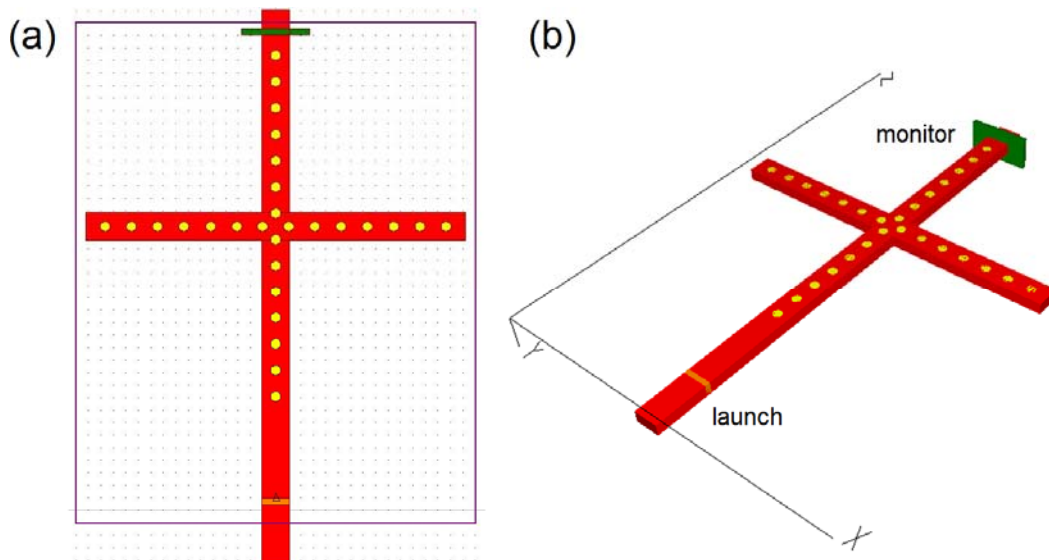


Figure 2.3 3D FDTD layout of cross waveguide resonator: (a) 2D topview of the device showing launch, monitor, and computation domain; (b) 3D schematic of the device that corresponds to (a).

from the first photonic crystal rod for the launched field to reach steady state before hitting the structure. A time monitor (the green bar) is placed at the output waveguide of the resonator to perform either time or frequency domain analysis of the transmitted optical wave. It can be noted that the monitor size is slightly larger than the waveguide cross section in order to include the evanescent field into the total intensity calculation. The computation domain (the purple rectangle) is large enough to include all the device features as well as the launch and monitor, where the boundary condition at the domain walls is set to be thick PML to effectively absorb any optical field that hits the boundary.

The material property of the dielectrics involved in the calculation is specified through a parameter dialog. The geometric RI profile (both real and imaginary parts with possible nonlinearities) of the dielectric components in the three calculation dimensions can be specified to be uniform, formulated, or user customized (based on previous calculations) according to different applications. As for the electro-optic modulator related applications, the OFF state (zero external bias) optical property of the dielectrics (silicon, silicon dioxide, and free space) can be specified using static RI at near infrared frequency range (uniform profile assumed). The RI for doped silicon is specified according to the Drude-Lorenz model with different dopant types and levels. However, for the ON state (non-zero external bias) properties, the silicon index profile can be perturbed corresponding to the free carrier movement profile from the electrical calculation (described in detail in Section 2.2.3). Therefore, the index profile under different bias voltage is specified by a user file that contains localized silicon index along with its coordinates in the recognized data format. For all the resonator based modulators studied in Chapter 2, the whole device is surrounded by silicon dioxide due to the buried oxide layer and presence of cladding for passivation (photonic crystal rods are completely filled with silicon dioxide too).

Then, the launched signal and monitor type can be chosen appropriately for different characterization purposes. For example, to perform frequency domain analysis, i.e. transmission/loss spectrum studies, the launched signal is usually set as an impulse with unit power intensity, which is an ideal Dirac delta function that covers all frequency components with equal amplitude. This is especially

convenient for transmission spectrum study compared to a pulsed launch since the spectrum saved in the monitor can be directly used without normalization to the launched signal. Therefore, the transmission spectrum of a photonic microcavity can be constructed by only normalizing its spectrum to that of a reference waveguide (with same material and geometry) to filter out the propagation loss associated with the plain waveguide.

After that, an optical monitor can be specified to enable discrete Fourier transform (DFT) to perform frequency domain analysis. The frequency range and step can also be specified to only include the resonance peak at an acceptable resolution. Usually, at least ten points are required to reconstruct a resonance peak so the frequency step size can be calculated according to the full-width half maximum (FWHM) pulse width of the peak which is partially determined by the quality factor of the resonator in the relationship $Q = f_c / f_{FWHM}$, where f_c is the resonance frequency.

Finally, the simulation parameters need to be correctly specified for numerical calculation. First, the computation domain should be designed to keep only essential details of the optical circuit to minimize calculation time and resources. The computation grid size needs to be fine enough to resolve the smallest feature of the circuit (usually the radius of the photonic crystal rods in the scope of this work). Then, the time step should be kept smaller than the stability limit according to the Courant condition. The stop time is the total simulation time during which the launched signal propagates throughout the structure. For optical circuitry that involves high Q cavities, the stop time needs to be particularly long enough for all the photons to pass through the cavity and reach stability at the output side. This condition can be verified through preliminary time domain transmission analysis where the transmitted intensity eventually approaches a stable level after long time propagation. Last but not least, the polarization type can be specified for polarization-dependent performance analysis.

It is equally important to point out that the time domain analysis can be performed feeding the structure with a continuous wave signal. This can be done in a similar way to the frequency domain

analysis discussed above. The time domain study is used in Section 2.3.2 to calculate resonance mode profile and modal volume.

2.2.2. Plane wave expansion method

The plane wave expansion method is usually used for theoretical analysis of PBG structures. It makes use of an important principle: normal modes in periodic structures can be expressed as a superposition of a set of plane waves, which is also known as Bloch's theorem [50]. In principle, PWE can be applied to find the time-independent modes of any lossless photonic structure. For the most part, however, it is intended to be applied to structures with some degree of periodicity in the refractive index distribution. Indeed, even when applied to non-periodic structures, the calculation is performed by introducing an artificial periodicity.

The theoretical essence of the method is demonstrated below [51]. By combining Maxwell's equations under the assumption of linear material and time-independent solution forms, we can obtain the vector Helmholtz equation (\mathbf{r} is the position vector):

$$\nabla \times \left(\frac{1}{\varepsilon(\mathbf{r})} \nabla \times \right) \mathbf{H}(\mathbf{r}) = \frac{\omega^2}{c^2} \mathbf{H}(\mathbf{r}) \quad (2.11)$$

Using Bloch's theorem, we have $\mathbf{H}(\mathbf{r}) = \exp(i\mathbf{k} \cdot \mathbf{r}) \mathbf{u}_{\mathbf{k}}(\mathbf{r})$, where $\mathbf{u}_{\mathbf{k}}(\mathbf{r})$ is a function with periodicity of the lattice. Inserting this expression in the Helmholtz equation, we obtain

$$\hat{\mathbf{L}} \mathbf{u}_{\mathbf{k}} = (i\mathbf{k} + \nabla) \times \left(\frac{1}{\varepsilon(\mathbf{r})} (i\mathbf{k} + \nabla) \right) \times \mathbf{u}_{\mathbf{k}} = \bar{\omega}^2 \mathbf{u}_{\mathbf{k}} \quad (2.12)$$

where we have defined the operator $\hat{\mathbf{L}}$ and the normalized frequency $\bar{\omega} = \omega/c$. Equation 3.12 is treated as an eigenvalue equation for the unknown eigenvalue $\bar{\omega}$ and eigenvector $\mathbf{u}_{\mathbf{k}}$. For each value of wave vector, it has an infinite number of solutions labelled by the band number n in order of increasing frequency and

according to group theory, the extreme points of all the bands must occur at points of high symmetry. Thus it is only necessary to examine a small subset of points in the first Brillouin zone.

For each required value of the wavevector \mathbf{k} , the method makes use of a variational statement of Maxwell's equations. Since the operator $\hat{\mathbf{L}}$ is Hermitian then the functional

$$E[\mathbf{u}_k(\mathbf{r})] = \frac{\int d\mathbf{r}^3 \mathbf{u}_k^* [\hat{\mathbf{L}} \mathbf{u}_k]}{\int d\mathbf{r}^3 \mathbf{u}_k^* \mathbf{u}_k} \quad (2.13)$$

is guaranteed to be real and positive for any choice of the magnetic field function \mathbf{u}_k . Moreover, it can be shown that the function which minimizes $E[\mathbf{u}_k(\mathbf{r})]$ is the eigenvector of $\hat{\mathbf{L}}$ of minimum frequency $\bar{\omega}$. The next lowest mode is the function which minimizes $E[\mathbf{u}_k(\mathbf{r})]$ and is simultaneously orthogonal to the lowest mode. Thus we can find as many modes (bands) as required by successively minimizing $E[\mathbf{u}_k(\mathbf{r})]$, and orthogonalizing each mode against all the previously found modes. To implement the minimization, the unknown eigenvector is represented as a Fourier series over plane waves from the reciprocal lattice:

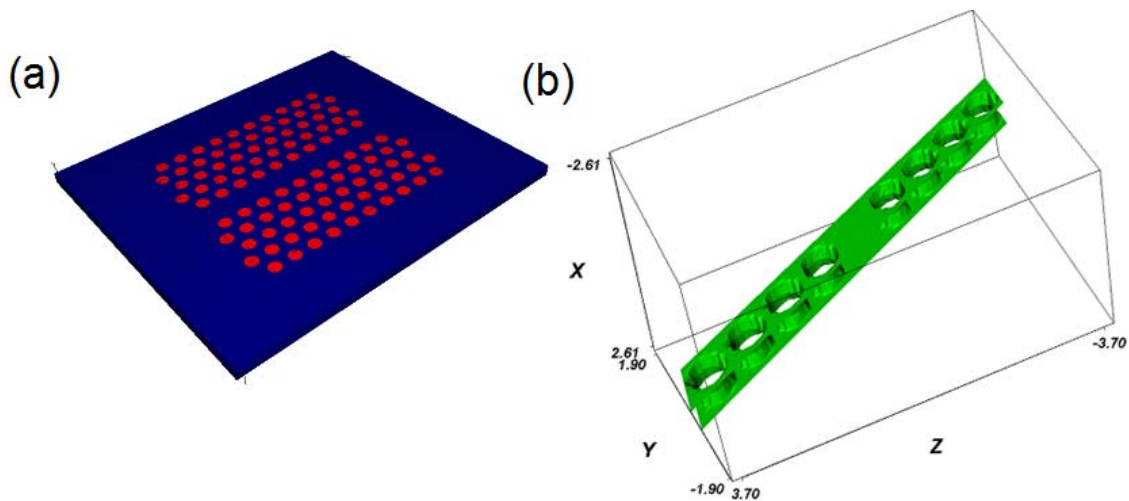


Figure 2.4 (a) 3D schematic of the photonic crystal slab waveguide for PWE method calculation; (b) 3D schematic of the supercell that is used in the band diagram calculation of the structure given in (a).

$$\mathbf{u}_{\mathbf{k}} = \sum_{\mathbf{G},\sigma} c_{\mathbf{G},\sigma} \hat{\mathbf{e}}_{\mathbf{G},\sigma} \exp(i\mathbf{G}\cdot\mathbf{r}) \quad (2.14)$$

where the sum is over all reciprocal lattice vectors \mathbf{G} and polarization states σ , and the $\hat{\mathbf{e}}_{\mathbf{G},\sigma}$ are unit polarization vectors. In the numerical implementation, the sum is truncated at a reasonable resolution and the calculation of $E[\mathbf{u}_{\mathbf{k}}(\mathbf{r})]$ becomes a matrix problem solved using iterative techniques.

In this work, the PWE method is used to calculate the projected band diagrams of the 3D photonic crystal waveguides based on a silicon thin slab (Section 2.4.1). In Fig. 2.4 (a), the photonic crystal lattices with different unit cell dimensions are completely covered by silicon dioxide cladding (holes are completely filled with silicon dioxide) and the slab sits on the silicon dioxide substrate. The waveguide defect bands are calculated using a supercell that covers 1, 4, and 9 primitive units in the x, y, and z directions respectively, shown in Fig. 2.4 (b). So the waveguide is modelled as a 1D photonic crystal lattice with periodicity aligned to y direction. The calculated wave vector \mathbf{k} path covers the edge of the irreducible Brillouin zone of the new lattice. Finally, for 3D problems, the vector Helmholtz equation is not separable into equations for different polarizations and all modes are default as “hybrid”. However, in the structure that possesses one or more planes of reflection symmetry, the modes can be classified as either even or odd, which is parallel to the meaning of TE-like and TM-like classifications. For example, for the W1 photonic crystal waveguide shown in Fig. 2.4 (a), the reflection invariance can be maintained along the central axis of the waveguide defect, i.e. y direction, therefore, the y parity can be set either even or odd to distinguish TE-like or TM-like polarizations. This calculation process is used in Section 2.4.1 to get the mode gap diagram for the hybrid-lattice resonator that consists of PCW stages with different lattice constants, which is shown later in Fig. 2.21 (b).

2.2.3. Physically-based device simulation

As the core part of the modulator, the EO active region of the device is modelled by a physically-based device simulator from SILVACO [44]. The device simulator is employed to predict steady-state and transient free carrier, electric field, and current density profiles throughout the active region in a 2D or 3D temperature-dependent dielectric-insulator-conductor environment. The SILVACO device simulation suite is a multipurpose semiconductor modelling software suite, which consists of a number of different packages that are used in conjunction to analyse device/process physics. The basic structure of the suite is shown in Fig. 3.8. For EO modulator related applications, three major components are involved: ATLAS, DevEdit, and Tonyplot. ATLAS is for device simulation, DevEdit for structure and mesh implementation and Tonyplot as well as other plotting softwares for data analysis.

As we can see from Fig. 2.5, ATLAS is the core of the simulation package which provides insight into the electrical characteristics of the device. As for this work, the simulator is used to predict directly both DC and AC power/energy consumptions, and predict indirectly the localized RI perturbation, overall phase shift, modulation depth, modulation speed, and 3-dB bandwidth of the device by incorporating other optical simulation modules (including those discussed in the previous sections). ATLAS simulates

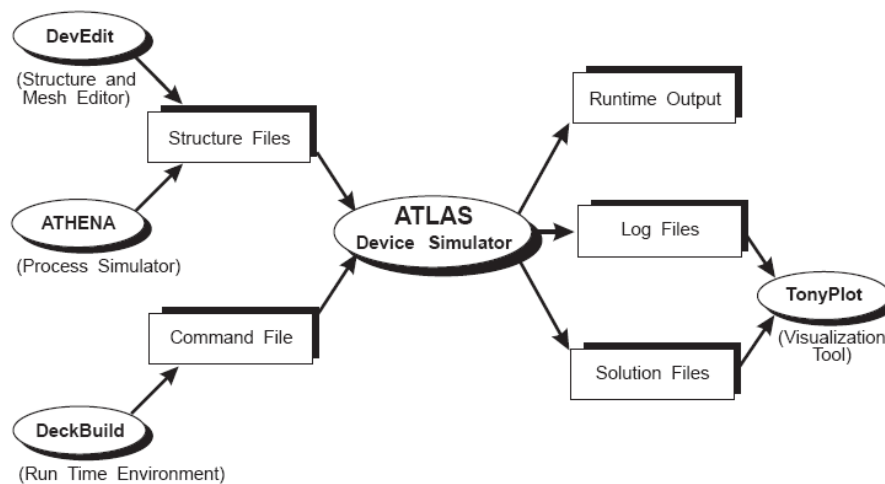


Figure 2.5 The basic structure of the SILVACO device simulation suite [44].

device characteristics by solving Poisson's equations and the continuity equation for electrons and holes, supported by a series of secondary equations that are used to specify particular physical models. At this point of time, only a 2D simulator is employed and hence all structures modelled are assumed to be homogeneous in the third dimension. As we recall from our knowledge of semiconductor fundamentals, Poisson's equation relates changes in electrostatic potential to local charge densities:

$$\nabla \cdot (\varepsilon \nabla \psi) = -qn \quad (2.15)$$

where ε is the local permittivity, ψ is the electrostatic potential, n is the local charge density and q is the unit charge. ATLAS defines ψ as the intrinsic Fermi level. The local net charge density is the sum of the contributions from all mobile and fixed charges, including electrons, holes and ionised impurities. Besides, the continuity equations for electrons and holes are:

$$\begin{aligned} \frac{\partial n_e}{\partial t} &= \frac{1}{q} \nabla \cdot J_{n_e} + G_{n_e} - R_{n_e} \\ \frac{\partial p_h}{\partial t} &= \frac{1}{q} \nabla \cdot J_{p_h} + G_{p_h} - R_{p_h} \end{aligned} \quad (2.16)$$

where n_e and p_h are the electron and hole concentrations, J_{n_e} and J_{p_h} are the electron and hole current densities, G_{n_e} and G_{p_h} are the generation rates for electrons and holes, R_{n_e} and R_{p_h} are the recombination rates for electrons and holes respectively, and q is the unit charge.

Then, secondary equations are used to specify particular models for J_{n_e} , J_{p_h} , G_{n_e} , G_{p_h} , R_{n_e} and R_{p_h} . The ATLAS default model for carrier statistics is the Boltzmann model. The Boltzmann model is an approximation to the Fermi-Dirac model. According to Fermi-Dirac statistics, the probability that an electron occupies an energy state with energy E is:

$$f(E) = \frac{1}{1 + \exp\left(\frac{E - E_f}{kT}\right)} \quad (2.17)$$

where E_f is the Fermi level and k is the Boltzmann constant. The Boltzmann approximation is:

$$f(E) = \exp\left(\frac{E_f - E}{kT}\right) \quad (2.18)$$

For heavily doped materials, however, Boltzmann approximations become less accurate than Fermi-Dirac statistics, so in this work, the Fermi-Dirac model is used for simulations.

The charge transport behaviour is modelled by a ‘drift-diffusion’ model, which assumes that the total current density of free carriers can be represented as the sum of drift current and diffusion current. This model is the default model for charge transport in ATLAS and widely used in our case. However, the model becomes less accurate when the feature size of the device goes below 90 nm.

Free carriers are accelerated by electric fields, but lose momentum as a result of various scattering processes. The scattering mechanisms include lattice vibrations (phonons), impurities, other carriers, surfaces, and other material imperfections. The modeling of carrier mobility in a bulk material involves:

- Characterizing carrier mobility μ as a function of doping and lattice temperature;
- Characterizing saturation velocity v_{sat} as a function of lattice temperature; and
- Describing the transition between the low field mobility and saturated velocity regions.

The simplest mobility model used in SILVACO is the concentration dependent model CONMOB. This model provides mobility statistics based on a lookup table at 300 K for either silicon or GaAs. The lookup table uses a simple power law to evaluate the mobility of electrons and holes at various electron and hole doping concentrations. A doping and temperature dependent low-field mobility model may be specified when modelling variations in lattice temperature on device performance. Klaassen recently proposed another mobility model, which applies different mobilities to majority and minority carriers [52, 53]. The model includes the effect of lattice scattering, impurity scattering, carrier-carrier scattering, and impurity

clustering effects at high concentration and is more accurate than other mobility models provided by SILVACO.

There are three recombination models used in the device modelling [45]. The first is the concentration dependent Shockley-Reed-Hall (CONSRH) model, which is an adapted version of the SRH model and uses concentration dependent lifetimes and the recommended standard model for silicon recombination statistics in ATLAS. The second recombination model is the Auger recombination model. It is important at carrier concentrations above 10^{15} cm^{-3} , where the energy released by a recombining electron is absorbed by another carrier, which emits this energy nonradiatively by collisions with the lattice, generating phonons. The third recombination model is used to account for recombination at semiconductor/insulator interfaces. In ATLAS, this is done by considering a surface recombination velocity, which is specified as a simulation parameter before simulation. It is here to mention that the surface defects and trap centres are also included in both CONSRH and Klaassen mobility model by specifying trap energy and concentration.

The major steps for device simulation in ATLAS are given below. Here, we use the reference hexagonal lattice resonator based modulator as an example to demonstrate the more complex 3D electrical device simulation. Of course, 2D simulation can be performed by following a similar set of procedures. The first step of any device simulation is to specify the device structure by either DeckBuild or DevEdit. The former is the command line style interface while the latter has graphic user interface and therefore more straightforward and controllable. After all, they are equivalent ways of drawing schematics in SILVACO. In this work, the device characteristics such as device dimensions, material composition, dopant profiles and contact electrodes are firstly specified through DevEdit.

Then, a computation mesh needs to be designed for simulation. The conception of mesh here is somewhat similar to the grid size parameter specified in optical simulation in FDTD and is therefore crucial for correct simulation results. A too-coarse mesh is apparently insufficient for acceptable results while a too-detailed one gives rise to an increased simulation time and computation resources.

Consequently, the recommended approach for designing a mesh is to try dense mesh first and then decrease the mesh density gradually. The optimum mesh size is where the simulation results begin to deteriorate significantly. This step can be done in DevEdit. After that, TonyPlot 3D needs to be used to confirm the correctness of the device and mesh setup in a 3D schematic view. So in Fig. 2.6 (a), the active region of the reference hexagonal-lattice modulator is shown, where the holes are completely filled with SiO₂. Aluminium electrodes are placed at the two ends of the highly doped regions to drive the device at far enough away from the photonic crystal waveguide to avoid significant metallic absorption of the guided mode. In Fig. 2.6 (b), the 3D computation mesh is shown where in the z direction, a uniform mesh is used since the device is homogeneous in the vertical direction, while in the x-y plane, a non-uniform mesh is generated automatically to resolve the fine feature sizes near the SiO₂ holes. It is worth pointing out that unlike in FDTD simulators, the electrical device simulator employs a triangular meshing scheme. The software itself has an upper limit for the total number of triangles and mesh points. The physical quantities, such as carrier level, current density, and E-field density, will be calculated only at the mesh points while at anywhere inside the mesh triangle, these values will be averaged by the values at the points of the surrounding triangle. Therefore, usually, one needs to make sure that there is a least one mesh point within the area of interest in order to probe the value precisely.

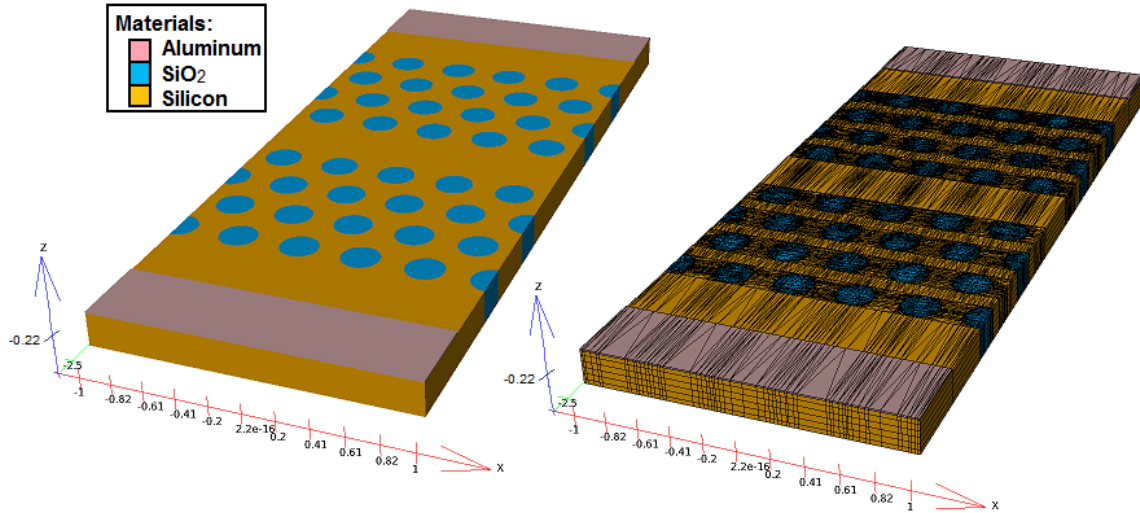


Figure 2.6 3D schematic of the device shown in Fig. 2.4: (a) device schematic that is composed by different material regions; (b) device material schematic with computation mesh (in black lines).

Then, physical models, numerical methods, and simulation parameters should be specified in DeckBuild. First, in the carrier depletion device modelling, we include *bipolar*, *band-to-band tunnelling*, and *impact ionization* models. To begin with, *bipolar* is a set of physical models that describes the basic operation mechanism of bipolar devices, which includes concentration dependent mobility, field dependent mobility, concentration dependent Shockley-Read-Hall (SRH) recombination, Auger recombination, and bandgap narrowing effect. These models are applicable to both injection and depletion mode operations. Additionally, band-to-band tunneling and Selberherr impact ionization [46] models are also included to model the device around or even beyond its breakdown point.

After that, numerical methods should be specified for detailed computation algorithm in the carrier/current calculation at each steady bias voltage (DC) or each transient time point (AC). Here, Newton's iteration method is used since it is the most efficient and robust scheme for solving a nonlinear algebraic system such as the Poisson and continuity equations. Each iteration of Newton's method solves a linearized version of the entire nonlinear system. The size of the problem is relatively large, and each iteration takes a relatively long time. However, the iteration will normally converge quickly (in about

three to eight iterations) so long as the initial guess is sufficiently close to the final solution. Strategies that use automatic bias step reduction in the event of non-convergence loosen the requirement of a good initial guess. Newton's method is also the default for drift-diffusion calculations in ATLAS. However, convergence may be difficult to achieve after many Newton iterations when the problem is poorly defined. For example, the grid may be very poor (i.e., it contains many obtuse or high aspect ratio triangles), or a depletion region may have extended into a region defined as an ohmic contact, or the initial guess may be very poor. In those cases, the input device structure file needs to be modified to fix the relevant problems.

Finally, the major physical parameters, such as carrier lifetime for electrons and holes, intrinsic carrier mobility, energy bandgap, surface recombination rate, and surface charge density, are defined according to silicon electrical properties at 300 K [16].

2.3. One dimensional photonic crystal cavities for EO modulators

The simplest way of constructing an EO modulator based on a photonic resonator is to employ a one dimensional dielectric medium modulation (i.e. 1D photonic crystal) and introduce either a geometric or material defect at the center of the otherwise perfectly periodic structure to trigger photonic resonance. The EO modulation is achieved by optical intensity change at the output waveguide, which results from a resonance peak shift due to a localized refractive index change, preferably at the central defect via nonlinear EO effects such as free carrier refractive and absorptive effects, Pockels effect or all-optical Kerr effect. In this section, the focus is mainly on the free carrier injection (forward bias) based index modulation scheme. The advantages of this operation mode are the following: First, the bias voltage (DC and AC peak-to-peak amplitude) required for high index shift is quite low, usually ~ 1 V, to guarantee high modulation depth in terms of optical transmission. This is due to the low turn-on voltage of the P-I-N diode usually configured to achieve high carrier contrast at the central intrinsic region. Second, since the index shift under carrier injection is quite high compared to other biasing schemes, the requirement for

optical resonance conditions (Q factor and modal volume) can be relaxed to include simple 1D photonic crystal cavities, such as FP cavities and cross waveguide resonators, which have an ultra-compact device dimension for high density integration purposes. However, the disadvantages are also quite apparent. One thing is the high DC/AC energy consumption of the device due to the large forward bias current of the P-I-N diode at the ON state. Another common concern is the significantly limited operation speed and 3-dB bandwidth of the device (on the order of 1 GHz), which is the result of the large carrier injection time associated with a planar P-I-N diode. To sum up, the carrier injection mode modulator faces significant performance limitation and is gradually replaced with more efficient operation modes and optical configurations that promise improved FOMs, which are covered in the remaining sections of this chapter and sections of next chapter.

2.3.1. Fabry-Perot microcavity based design

In this section, a 1D subwavelength Fabry-Perot resonator is designed for silicon EO modulators. The device schematic is shown in Fig. 2.7, where the FP resonator is defined by etching five air holes on both sides of the rib waveguide. A localized optical mode is permitted within the original bandgap, thereby forming a resonance peak due to Bragg reflection. The structure was first proposed by Foresi et al. [8], and later adopted by Schmidt et al. to build a modulator [25]. In this design, the central defect is 580 nm long, only about 1/3 of the resonant wavelength, helping to reduce the doping area and therefore power consumption. The radius of the air holes is 100 nm with a 420 nm lattice constant.

To make it electrically active, an ultra-thin silicon slab (23 nm) below the waveguide is introduced and P⁺ and N⁺ regions are defined by lateral boron and phosphorous doping on each side of the waveguide, each with a doping concentration of $1 \times 10^{20} \text{ cm}^{-3}$, denoted as DOC₁. The ultra-thin silicon slab along with the relatively small waveguide height (200 nm) further reduces doping volume and more

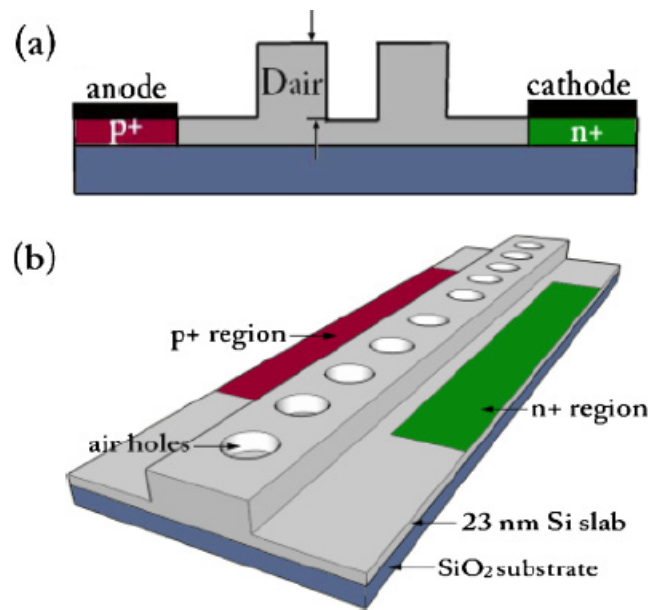


Figure 2.7 Schematic of the resonator-based electro-optic modulator: (a) cross sectional schematic of electrical profile with illustration of electrodes and embedded P-I-N diode; (b) 3D schematic of optical profile with illustration of 1D FP resonator.

significantly, reduces the total number of injected free carriers, whilst maintaining significant modal overlap and the injected free carriers. This special design results in reduced power consumption without sacrificing modulation depth. The width of the waveguide is 470 nm, which, along with the total length of 4.47 μm , indicates 2.1 μm^2 surface area. When the P-I-N diode is forward biased, free carriers of both electrons and holes will be injected into the central intrinsic region and thus cause a sizable perturbation of refractive index, which in turn results in a certain amount of peak shift and finally a significant ON/OFF contrast is realized to achieve intensity modulation. The main advantages of the modulation scheme, when compared with phase modulation using MZI configuration, lie in the facts that, first, the device employs only one waveguide instead of two arms and thus compact in terms of surface area and volume; and second, much less insertion loss is achieved by avoiding additional scattering due to waveguide splitters. However, the drawback is that this design may not be as sensitive as phase modulators due to the absence of phase interferometry.

Electrically, the ATLAS device simulation package described earlier has been used to predict both DC and transient characteristic of the device. The electrical simulator includes SRH, Auger, and direct recombination models. The SRH recombination carrier lifetimes are $\tau_n=700$ ns, $\tau_p=300$ ns, where τ_n and τ_p correspond to a realistic intrinsic epilayer doping concentration of 10^{15} cm⁻³ [18]. According to the electrical simulator, both types of carriers are distributed quite uniformly throughout the originally intrinsic waveguide when a 1V bias voltage is applied to the diode. Hence, it is reasonable to assume a highly uniform index perturbation in the waveguide when the device is turned on. The current-voltage (I-V) characteristic of the embedded P-I-N diode is predicted by a 2D electrical simulator and we assume the device is homogeneous in the longitudinal direction (the direction of propagation), therefore, the driving current of the diode is measured as the transverse current per unit length of the device (mA/mm). The device is biased at 1.18 V, where according to Fig. 2.8, driving current density is the smallest whilst

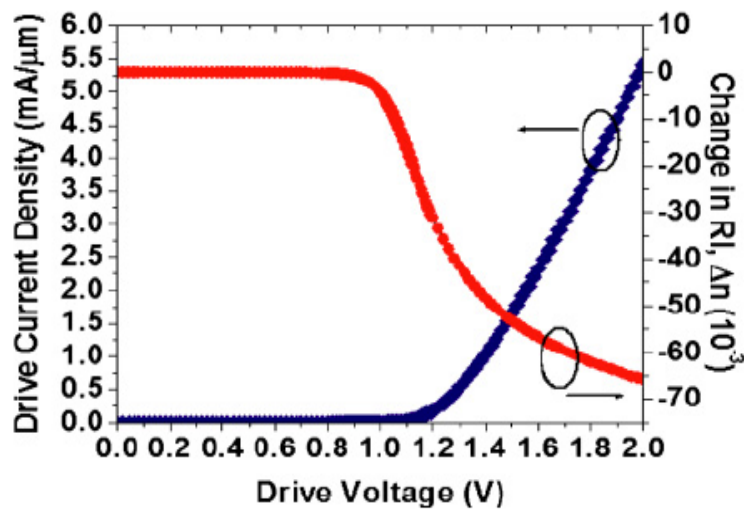


Figure 2.8 I-V characteristic and corresponding RI change of the doped area.

sufficiently large index changes are detected (only real part of the index is plotted). This unique fact indicates that the device is first turned on optically before it is turned on electrically, which makes it possible to achieve a large amount of peak shift at low power consumption.

The physical explanation for this phenomenon lies in the working mechanism of the diode. When the diode is forward biased and the bias voltage is smaller than the threshold value, the total current is dominated by the diffusion current because the field intensity is still too small for carriers to get a big drift velocity; at the same time, carriers begin to diffuse into the intrinsic region, where an acceptable refractive index change can be achieved due to the change of carrier concentration. This situation is similar to the accumulation mode of a MOS capacitor, where carriers accumulate on each side of the oxide when the capacitor is forward biased. However, since the junction capacitance of a P-I-N diode is much smaller than that of the MOS capacitor, the threshold voltage of the diode is quite small and the current increases exponentially with the bias voltage beyond threshold.

Dynamically, the aforementioned SRH, Auger and surface recombination models are included to predict the dynamic behavior of the injected free carriers. In this work, the rise time is defined as the time interval during which the absolute value of index change increases from 10 to 90% of its maximum value;

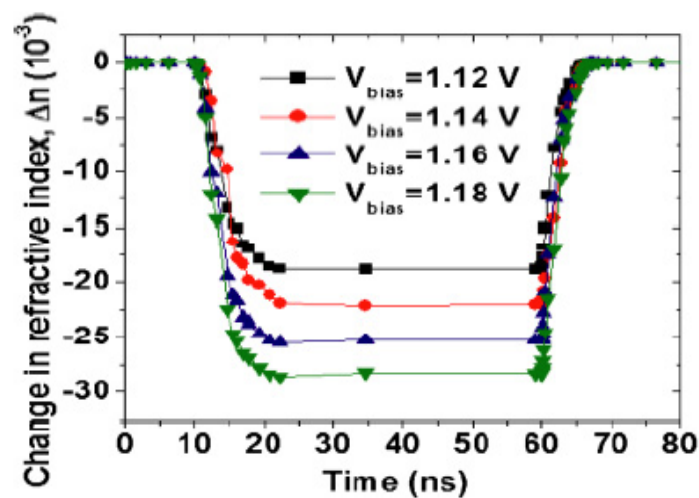


Figure 2.9 Transient characteristic of the modulator at different bias voltages indicates a peak modulation speed of 100 MHz.

and the fall time is the time interval during which the absolute value of index change decreases from 90 to 10% of its maximum value. According to semiconductor physics, the rise/fall time is quite sensitive to carrier mobility; carrier lifetime and surface recombination rate and in the simulations, these parameters

pertain to silicon data at 300 K [16]. It is shown in Fig. 2.9 that the 10-90% rise time and fall time are about 6.2 and 3.8 ns, respectively, and almost unchanged under different bias voltages. Therefore, it is reasonable to expect 100 MHz modulation speed from the device. Optical characterization of the device, on the other hand, involves a 3D FDTD simulator from RSoft photonic component design suite. First of all, the fundamental mode profile of the rib waveguide is solved using beam propagation method (BPM, discussed in detail in Section 3.2.1) and the result, shown in Fig. 2.10, demonstrates that the overwhelming majority of the total field intensity is distributed within the rib, which indicates a high performance of the waveguide in terms of transmission efficiency. Then, doping area was optimized in terms of maximizing peak shift at the same bias voltage. This is achieved by extending the doping area from the central defect to a given hole, numbered starting from 1 from the cavity outwards and denoted as the variable N_{dop} , on each side of the cavity. The resonance peak shift corresponding to different values of N_{dop} at the same voltage bias was measured using the 3D FDTD simulator, which indicates that peak shift

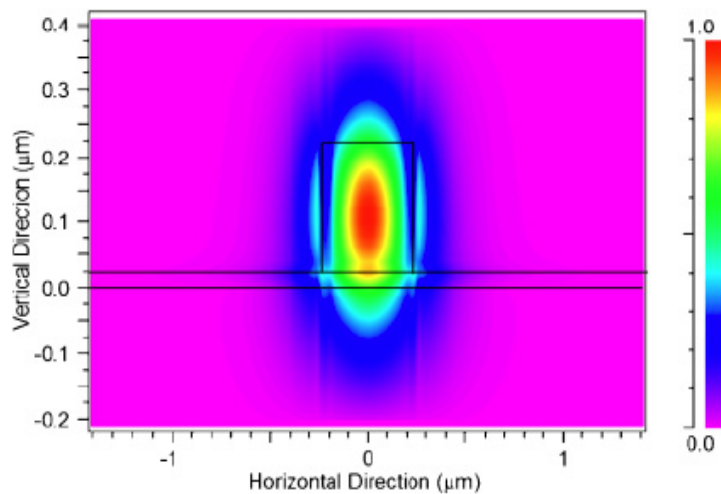


Figure 2.10 Fundamental mode profile of the rib waveguide with the absence of air holes and central doping.

stops increasing when doping area extends to greater than three holes. This explains the design shown in Fig. 2.7 (b).

Further investigations have also been conducted to explore the relationship between resonance peak shift, modulation depth and DC power density, which is defined as

$$P_{DC} = V_{bias} i \quad (2.19)$$

where V_{bias} and i are the bias voltage and current density respectively. By combining information from Figs. 2.9 and 2.11, we expect a 10 dB modulation depth at a speed of 100 MHz with power consumption of 186 $\mu\text{W}/\text{mm}$, where the peak shift is an order of magnitude larger than what was reported by Schmidt et al.

The modulation speed of this device is partially determined by the electrical aspect of the design due to the carrier injection mechanism of the P-I-N diode configuration. Therefore, alternative doping profile of the active region has been tried and this is realized in two respects. Kärtner et al. demonstrated previously that sidewall doping could reduce carrier injection time and improve uniformity of carrier distribution throughout the waveguide while at the expense of a little increase in propagation loss [54]. This strategy is incorporated into the device and illustrated in Fig. 2.12.

Firstly, the thickness of the sidewall doping, designated WT, and the distance from P⁺/N⁺ region to sidewall of the waveguide, DTW, are kept unchanged at 30 and 515 nm, respectively, while the doping concentration, i.e. DOC₂, is increased from 10¹⁸ to 10¹⁹ cm⁻³. According to Fig. 2.13, the fall time is reduced to 0.5 ns and rise time to about 4 ns at the bias of 1.18 V, which indicates a top modulation speed around 220 MHz with the sidewall doping concentration of 10¹⁹ cm⁻³. Although even higher doping

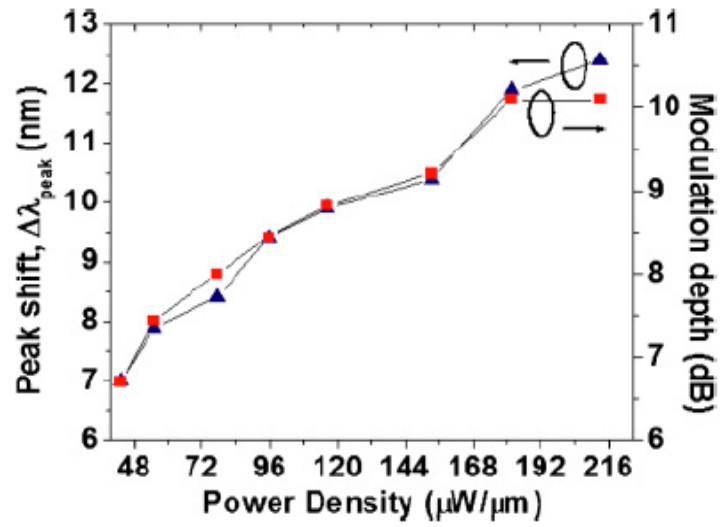


Figure 2.11 Relationship between resonance peak shift, modulation depth, and power density.

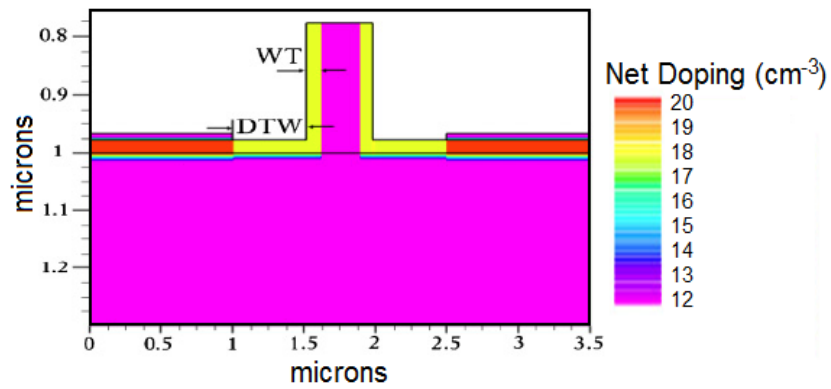


Figure 2.12 Color coded schematic of the net doping profile of the active region located at the center of the waveguide.

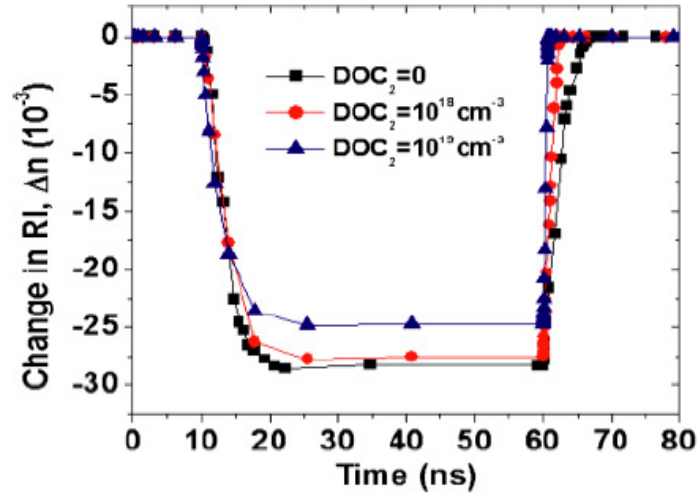


Figure 2.13 Transient performance improvement of the device after the introduction of sidewall doping. A modulation speed of 220 MHz is detected at 1.18 V bias when DOC_2 equals 10^{19} cm^{-3} .

concentration can be used, it is shown that the additional increase in the modulation speed is insignificant while propagation loss becomes dominant and serves as an obstacle for practical purposes. Different WT values have also been tried and no further reduction of either rise or fall time was detected.

According to Fig. 2.14 (a), both a decrease in current density and an increase in RI change are detected at the same voltage bias. That is to say, a higher modulation depth is predicted at a reduced power supply. At a bias voltage of 1.18 V, where the device is operated, the DC power density is further reduced to $86 \mu\text{W}/\text{mm}$. Additionally, according to Fig. 2.14 (b), 10 to 90% rise time and fall time are also reduced to 3 and 0.4 ns, respectively. Therefore, a modulation speed of at least 300 MHz is achieved when the P^+ and N^+ regions are kept 155 nm away from the central rib. In the 2D simulator, we assume no holes in the active region; therefore, the real device can achieve higher speed because no carrier will be injected into air holes. Thanks to the characteristic 23 nm thin slab, the fundamental mode of the rib waveguide, given in Fig. 2.10, does not adopt the conventional “pear like” shape. This is important because negligible field power permeates into either side of the slab. Consequently, the additional loss caused by the close vicinity of the P^+/N^+ region to the central rib is negligible.

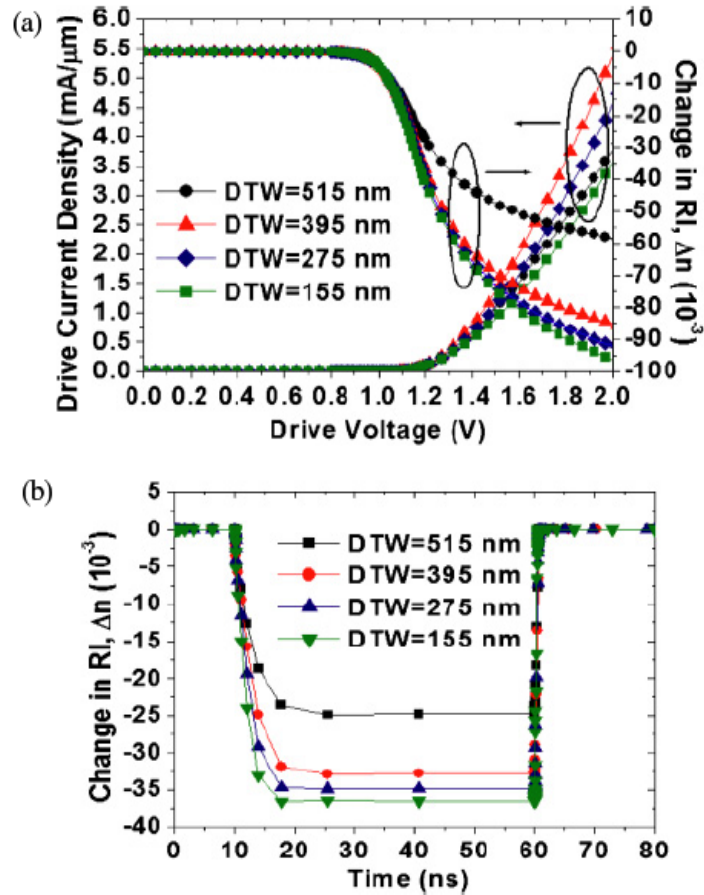


Figure 2.14 Improved performance of the modulator is detected as the value of DTW decreases from 515 to 155 nm. The upper (a) is the DC characteristic of the device, which demonstrates an increase in the modulation depth at a reduced power supply; and transient characteristic in the lower (b) indicates an improved modulation speed of 300 MHz.

To sum up, the FP resonator-based design can be optimized in terms of dopant profile and waveguide geometry. The optimum performance of the device shows a low DC power consumption of 86 $\mu\text{W}/\text{mm}$. The device is modulated at a doped P-I-N junction overlapping the cavity in a silicon waveguide perforated with etched holes. The compact device (surface area only 2.1 μm^2) is capable of a modulation speed of at least 300 MHz after sidewall doping is introduced and suitable for fiber to the home (FTTH) technologies, where speed can be traded for low cost and power consumption. The device does not rely on ultra-high Q, and could serve as a sensor, modulator, or passive filter with built-in calibration.

Although the device studied in this section has the most compact footprint and the lowest required DC bias voltage, its weakness lies in its low modulation speed due to the indirect carrier injection route where a significant amount of carrier momentum is lost when carriers reach the active region of the device. This limitation in the efficiency of carrier injection and device speed will be alleviated in the cross waveguide resonator structure that is discussed in the following section.

2.3.2. Cross waveguide based design

The cross waveguide-based design enables a more efficient carrier injection scheme by alleviating two limitations in the single FP waveguide resonator based approach [25]. Firstly, free carriers in the previous structure take an indirect route when injected from the two ends of the lower slab to the upper central waveguide, thus a sizable part of the total carrier momentum is lost when they reach the intrinsic region. Secondly, the thickness of the slab is quite thin (compared to the height of the waveguide) for high volume carrier injection. The cross waveguide structure, on the other hand, consists of two crossing FP resonators with a defect mode confined at the central intersection. The free carriers then take a direct route from either branch to the central intrinsic region with the presence of an external voltage bias and since the height of the doping branches is the same as the guiding branches, the carrier flow is not confined to a relatively small volume. The overall effect of these is an improved modulation frequency and bandwidth.

The optical model of the device is based on a cross waveguide resonator, where two identical 1D subwavelength FP waveguide resonators [55] are configured perpendicular to each other and therefore a microcavity is formed at the central intersection, shown in Fig. 2.15 (a). The Bragg mirrors in each FP resonator are achieved by etching periodic air holes into the silicon ridge waveguides, which are built on a SOI wafer. A localized transverse-electric (TE) mode will be allowed into the original bandgap due to the

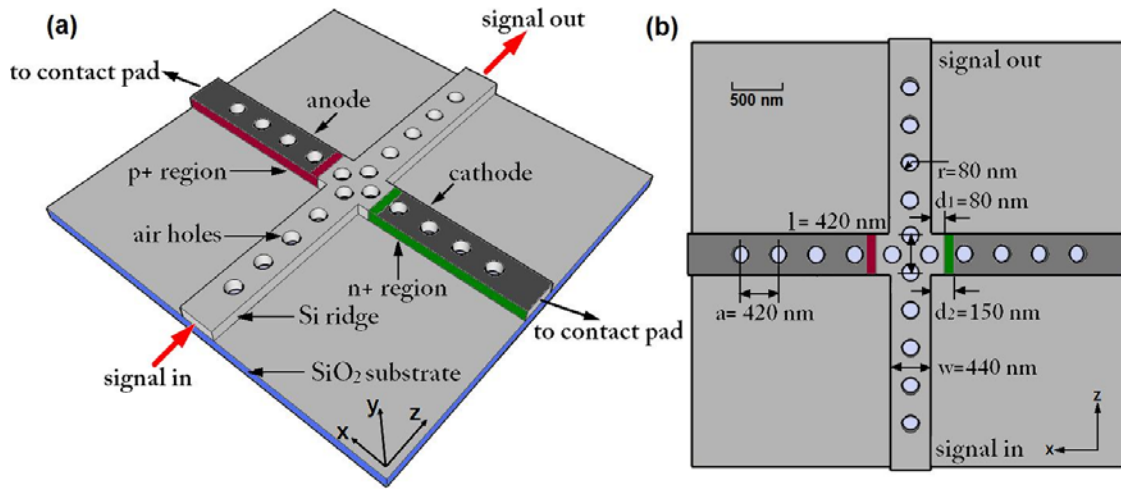


Figure 2.15 (a) 3D schematic of the cross waveguide resonator based modulator; (b) top view of the device with notations of the optimum device dimensions.

central defect and consequently, a resonance peak can be detected in the transmission spectrum. To make the device active, two opposite branches are partially doped to be P^+ and N^+ regions respectively so that a transverse P-I-N diode is embedded into the cross waveguide. When the diode is forward biased by an external voltage supply, free electrons and holes will be injected into the central intrinsic region, where a RI perturbation can be achieved due to the free carrier effect. The RI perturbation will in turn result in a resonant peak shift and therefore significant ON/OFF contrast can be obtained. However, the price paid is the reduced modulation depth due to the lower quality factor of the cross waveguide cavity (~ 190), and the increased electro-absorptive optical loss due to the immediate adjacency of the impurities. The device dimensions are optimized in terms of both optical and electrical responses with the optimum combination shown in Fig. 2.15 (b). The height of the waveguide is 200 nm.

Optically, a 3D FDTD simulator from RSoft is employed to optimize the resonance peak of the cross waveguide microcavity. The study is based on the passive resonator structure without doping. The conventional approach to that involves a 3D parameter scan of hole radius r , lattice constant a , and defect length l . Here, we adopt an alternative two-step strategy. Firstly, since the spectral size and location of the photonic bandgap depend on normalized radius (r/a), we keep hole radius r and defect length l as

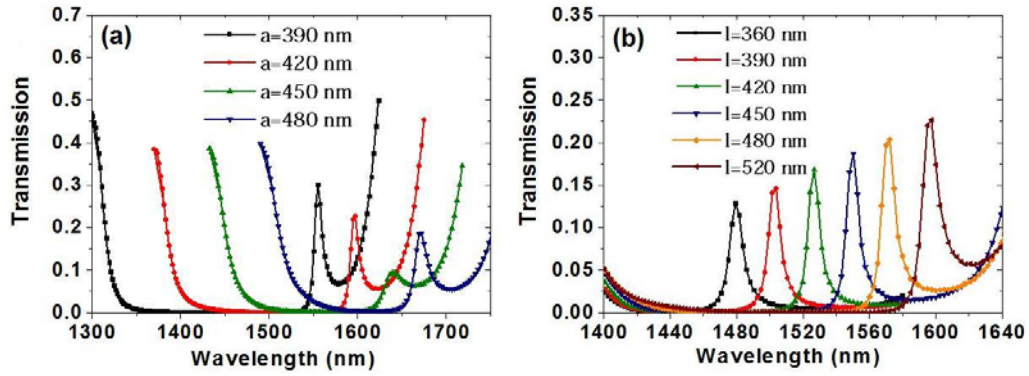


Figure 2.16 Resonance peak optimization: (a) tuning lattice constant a to move mid-gap wavelength to 1550 nm; (b) tuning defect length l to position resonance peak toward the middle of the bandgap.

constants at 80 nm and 520 nm respectively, and tune lattice constant a to 420 nm so that the mid-gap wavelength is around the infrared communication band of 1550 nm, Fig. 2.16 (a). This is because we want to locate our potential resonance peak around 1550 nm while at the same time in the middle of the bandgap in order to optimize pulse shape and EO tunability. Then, we keep the hole radius and lattice constant at 80 nm and 420 nm respectively and tune the length of the central defect l . It is shown in Fig.2.16 (b) that the resonance wavelength decreases with a decrease of defect length. Moreover, the pulse becomes symmetric about resonance wavelength when it reaches the center of the bandgap, which is important because the modulation depth can be improved for the same amount of blue shift of resonance peak caused by the free carrier effect. Therefore, the optimum defect length is kept at 420 nm, which is equal to lattice constant. Further study (decreasing l further down to 360 nm) shows that this coincidental relationship between lattice constant and defect length is neither a sufficient nor necessary requirement for achieving a spectrally symmetric resonance peak. However, the coincidence itself is interesting since it differs from the situation of a single FP resonator, where the optical cavity disappears when lattice constant and defect length are kept the same. The quality factor is calculated to be 190.2 using the fast harmonic analysis (FHA) method [47] and verified by the energy decay method according to the definition $Q = 2\pi(E_S / E_L)$ where E_S is the stored energy and E_L is the energy loss per oscillation. The cavity supports a fundamental mode of 1526 nm in wavelength with mode volume $0.71(\lambda/n)^3$, which

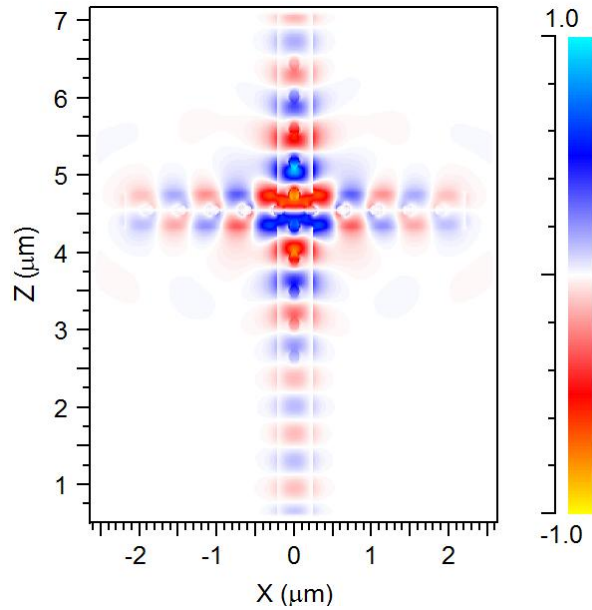


Figure 2.17 Color coded E_x field intensity profile of the cavity mode with resonance wavelength of 1526 nm. The cavity mode penetrates partially into the side branches.

is below the fundamental limit of $(\lambda/n)^3$ so that both device dimension and power consumption can be kept low. The free spectral range (FSR) and finesse of the cavity are around 800 nm and 80 respectively. The field intensity profile of the cavity mode, Fig. 2.17, indicates that the mode energy penetrates partially into the doped branches and will encounter impurity absorption in the active structure.

The electrical response of the device is based on a transverse P-I-N diode, where the P^+ and N^+ regions are defined by lateral boron and phosphorous doping in two opposite waveguide branches. The physical parameters pertain to silicon data at 300 K and the same set of recombination and carrier statistic models in the previous section is used here in this study.

To begin with, according to the cavity mode distribution in Fig. 2.17, the offset distance of doping regions from the central cavity is kept at 80 nm as a tradeoff between modulation speed and carrier induced optical loss and the aluminum electrodes are placed 150 nm from the cavity to reduce shown in Fig. 2.18 (a), accompanied by the RI changes of the intrinsic region under each bias voltage.

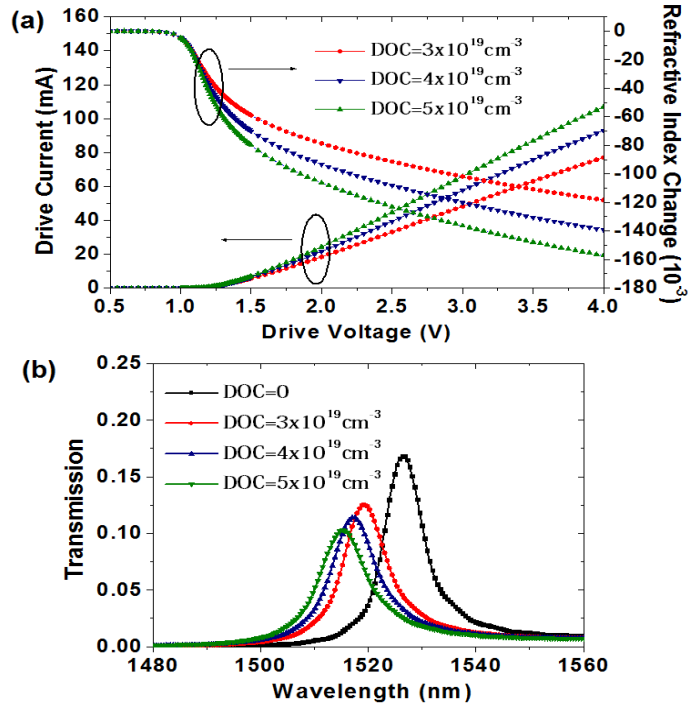


Figure 2.18 Electrical and optical response of the device to different doping concentrations: (a) I-V characteristics of the p-i-n diode shows a lower bias voltage is needed to achieve the same RI change for higher doping concentrations; (b) a blue shift and amplitude decrease of the resonance peak are detected with an increase of the doping concentration.

According to Fig. 2.18 (a), for the same index change, the bias voltage and the corresponding current flow decrease with an increase of doping concentration. That is, heavier doping promises lower power consumption for achieving the same modulation depth. On the optical side, however, the carrier induced optical loss increases with doping concentration, shown in Fig. 2.18 (b), and becomes unacceptable when doping concentration goes beyond $8 \times 10^{19} \text{ cm}^{-3}$. For further modeling of the device, the doping concentration is kept at $4 \times 10^{19} \text{ cm}^{-3}$ in order to suppress thermal-optic competition due to excessive power consumption, while still keeping free carrier absorption acceptable. The carrier induced optical loss is calculated to be 1.68 dB by comparing optical transmission of the passive structure with that of the doped one, Fig. 2.18 (b).

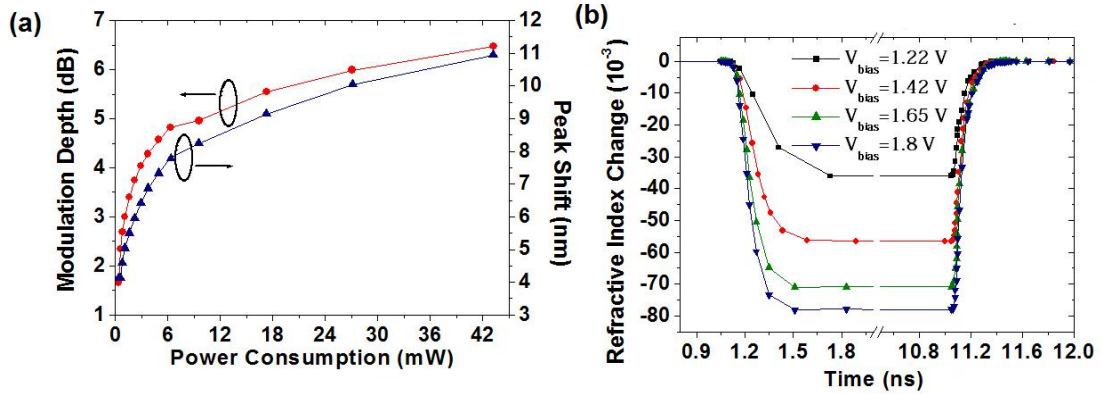


Figure 2.19 DC and transient characteristics of the device performance: (a) the relationship between modulation depth, peak shift and power consumption; (b) refractive index changes with time in response to a rectangular voltage pulse with different amplitudes, and 2.9 GHz modulation speed is indicated at the bias voltage 1.65 V.

The index perturbation information in Fig. 2.18 (a) is interpreted into optical response of the cavity resonator by the FDTD simulator. The bias voltage V_{bias} is changed from 1 to 2 V and the resultant modulation depth and resonance peak shift are given in Fig. 2.19 (a), which indicates unsurprisingly that both modulation depth and peak shift increase with external voltage supply and power consumption. Moreover, both of the aforementioned figures increase dramatically at first and then slowly when power consumption goes beyond 10 mW. This is because the P-I-N diode is turned on when the bias voltage exceeds the threshold voltage V_t and thus the diode current begins to increase quickly. This phenomenon agrees well with the information shown in Fig. 2.19 (a), where a threshold voltage of 1.4 V is indicated. For resonator based optical modulators, FWHM voltage V_{FWHM} is usually defined to measure the bias voltage required to make the resonance peak shift an amount that equals to FWHM width of the original peak [40]. According to Fig. 2.19 (a), the V_{FWHM} of our device is 1.8 V and is suitable for low power applications.

Finally, the aforementioned carrier models are included to predict the dynamic behavior of the free carriers. The rise time is defined as the time interval during which the absolute value of index change increases from 10% to 90% of its maximum value. The fall time is defined in a similar way. Figure 2.19

(b) shows the transient index change of the microcavity in response to a rectangular voltage pulse. The amplitude of the pulse is varied from 1 to 2 V, the same voltage range that was used to study the static performance. According to Fig. 2.19 (b), the modulation speed varies a little bit between different voltage pulses and the top speed hits 2.9 GHz (rise time 0.19 ns and fall time 0.15 ns) when V_{bias} is kept at 1.65 V (P=17.3 mW). The 3-dB bandwidth f_{3dB} is calculated around 4 GHz.

The modulation depth of the device is less than 5 dB before the diode is turned on, Fig. 2.19 (a), which is not very high for silicon modulators. This is mainly because of the less efficient mode confinement at the central cavity as shown in Fig. 2.17. Therefore, the radius of the central 4 air holes r_c is tuned since they are more influential on the major FOM of the cavity, such as quality factor Q and mode volume V_{mode} . The rest of the holes are kept unchanged assuming no change to the carrier injection channel. As is shown in Tab. 2.1, both temporal confinement Q and spatial confinement V_{mode} first increase and then decrease when r_c is varied from 60 to 100 nm similar to the results reviously demonstrated in [56]. In order to understand how Q and V_{mode} affect modulation performance, especially modulation depth, a 1.65 V DC bias is applied to the aforementioned cavities with different r_c . Both resonance peak shift $\Delta\lambda_c$ and modulation depth (MD) vary in a similar trend as that of the cavity confinement, and the maximum depth reaches 5.7 dB at a radius of 85 nm, where Q is the second largest and V_{mode} the largest. This is reasonable because for resonator based intensity modulators, $MD \propto \Delta\lambda_c / \lambda_{FWHM}$, where λ_{FWHM} is full width half maximum pulse width. Also, since index perturbation is almost uniform inside the active region, the optical field with a larger mode volume experiences a larger spatial area of index change and this also helps improve MD. The overall improvement of either $\Delta\lambda_c$ or MD, however, is not very significant since quality factor does not change too much with the radius. Although a much higher Q is achievable by adding more holes in each branch [57], the scattering loss is huge and the transmission becomes too weak to be practically useful. The advantage of a lower quality factor cavity is the less

temperature dependent performance and more efficient channel usage, e.g. in a dense DWDM communication system where the wavelength spacing between two neighboring channels is only 1 to 2 nm. Additionally, the relatively wide peak can tolerate moderate wavelength drift from the light source.

Table 2.1 Cavity optical confinement and response at different r_c under the voltage bias of 1.65 V

r_c (nm)	Quality factor	Mode volume $(\lambda/n)^3$	Peak shift (nm)	MD (dB)
60	175.8	0.44	9.0	4.7
65	181.1	0.53	8.9	5.0
70	185.7	0.58	8.7	5.0
75	188.7	0.66	8.9	5.4
80	190.2	0.71	9.2	5.5
85	189.4	0.74	9.0	5.7
90	185.5	0.67	9.0	5.6
95	177.6	0.57	8.6	5.5
100	166.4	0.48	7.8	4.8

On the other hand, the modulation speed of the device depends on both free carrier lifetime τ_c and photon lifetime τ_{ph} . The former is not tunable for a specific material system at a specific impurity level unless some CMOS incompatible materials known as carrier lifetime killers are introduced, e.g. gold or platinum [15]. The latter, however, can be engineered through the relationship $\tau_{ph} = Q/\omega_0$, where ω_0 is the resonance frequency. Therefore, for low quality factor ($Q \ll 10^4$) modulators, the speed of the device is mostly limited by τ_c rather than τ_{ph} because the former is much larger than the latter.

In this section, a cross-waveguide resonator based silicon EO modulator is studied. The device has a compact surface area of $16 \mu m^2$ ($4 \mu m \times 4 \mu m$) and the modulation speed is predicted to be as high as 2.9 GHz (3-dB bandwidth around 4 GHz). Although the device speed is a noticeable improvement from the FP resonator based device proposed in the previous section, the absolute value of the operation bandwidth is still considered low for high data rate communication applications. Besides, the DC power is 17.3 mW, which is low for a single device but the total power consumption can be unacceptably high when a high integration density silicon chip is considered.

To address the above concerns, in the following section (Section 2.4), a 2D PC cavity is proposed and numerically studied to further improve optical confinement and EO sensitivity of the resonance mode. On the electrical side, a carrier depletion dopant profile is adopted, where the carrier movement is much faster and no longer limited by the slow rising time of the carrier injection operation. As a result, the modulation speed of the device is significantly improved. At the same time, the AC energy consumption is kept ultra-low while the DC energy consumption is negligibly small due to the almost zero leakage current.

2.4. Two-dimensional photonic crystal cavities for EO modulators

Compared to 1D PC cavity based approaches for EO modulation, 2D PCs give additional degrees of freedom for alternative optical confinement and electrical operation schemes. Similar to its 1D counterpart, a 2D PC cavity can be constructed by introducing either a point or line defect to an otherwise perfect 2D PC lattice. The RI at the active region (usually designed at the central defect to maximize EO overlapped volume and therefore sensitivity) can therefore be modulated via various nonlinear EO effects with an external driving signal (DC and AC). The overall effect is the shifted resonance peak and transmission contrast. The exclusive advantages of 2D PC cavities for EO modulators, especially compared to their 1D counterparts, can be summarized into the following few points. First, since the optical confinement of 2D cavities is much stronger (much higher Q factor and more compact modal volume), the requirement for index shift (resulted from free carrier movement) is much lower due to the higher EO sensitivity of the high Q cavities. This makes it possible that alternative modulation schemes with lower level carrier movement can be employed to replace injection mode due to their higher operation speed (3-dB bandwidth on the order of 100 GHz) and lower energy consumption. For example, the depletion mode (reverse bias) and even the breakdown delay-based depletion mode (reverse bias beyond breakdown point) are effective for achieving high transmission contrast although the carrier

concentration contrast at the active region is much lower than that of the injection mode. Another benefit comes from the negligibly small leakage current of the reverse biased P-I-N or P⁺PNN⁺ diode. As a result, the overall energy consumption of the device (either DC or AC) can be kept ultra-low at a few fJs. However, the price paid for this is first a slightly larger device footprint of the 2D PC lattice. Second, for depletion mode operation, the amplitude of the reverse bias voltage is much higher at ~10 V (in terms of peak-to-peak value in the AC case). Practically, this can be challenging for state-of-the-art RF signal generators operating at ~100 GHz. Also, this imposes difficulty on the design of the corresponding driving circuitry.

Within this section, a photonic hybrid lattice resonator based silicon modulator is studied with carrier depletion mode operation. First in Section 2.4.1, the optical and electrical design of the device is introduced. Then in Section 2.4.2, it is found that the tapered PC lattice at the central cavity noticeably enhances the EO modulation efficiency of the device by reducing free carrier scattering at the active region. After that, the modulation performance of the device is analyzed by applying a breakdown delay-based depletion mode operation scheme (Section 2.4.3). This newly proposed operation method is found to be able to achieve deeper carrier contrast without sacrificing device speed or energy consumption due to the quasi-steady state within the breakdown delay. Finally, a summary is provided at the end of the section.

2.4.1. Optical and electrical design of the photonic hybrid-lattice resonator based modulator

According to Fig. 2.20 (a), the cavity is built on a 2D W1 (removing a row of PC holes at the lattice center) waveguide, where the air holes (radius $r=123$ nm) are completely etched down into the silicon layer (thickness $h=217$ nm) in a SOI system. The device surface and air holes should be completely passivated by SiO₂ cladding and filled. The idea of the proposed hybrid lattice mode gap

(HLMG) resonator is to introduce a photonic mode-gap (PMG) [58] by sandwiching a rectangular lattice (PC2, lattice constant a_2) within a hexagonal lattice (PC1, lattice constant $a_1 = 410$ nm). The resultant cavity can provide strong confinement in the x direction for waveguide defect modes whose frequencies lie within the PMG (guided modes in PC2 but evanescent modes in PC1). To improve optical confinement in the y direction, an additional transitional lattice (TL, three periods) is inserted between PC1 and PC2 to guarantee a smooth spatial field variation, and therefore, provide a high proximity to Gaussian-like mode envelop, which has been previously recommended for realizing high Q slab cavities [59]. A top view of the resonator is shown in Fig. 2.20 (b), where the central three columns of PC1 (dashed red circles) are shifted towards the defect center to provide a smooth transition from a hexagonal

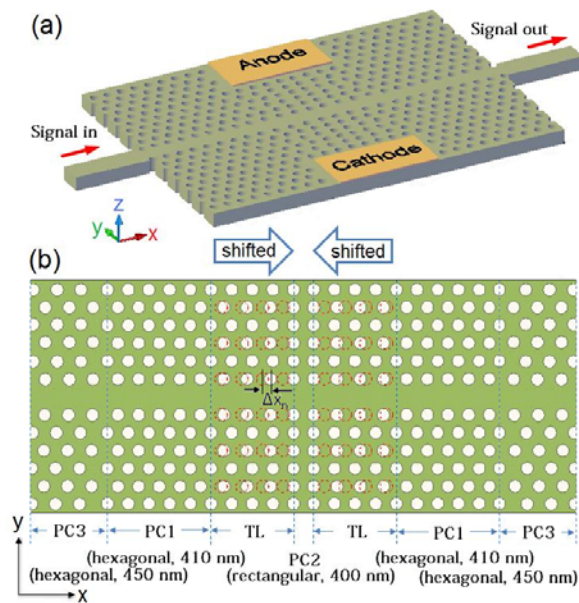


Figure 2.20 (a) 3D schematic of the device showing the planar HLMG resonator and electrode configuration for external driving signal. (b) The magnified 2D demonstration of the HLMG resonator constructed by hybrid PC lattice transition and additional insertion stages.

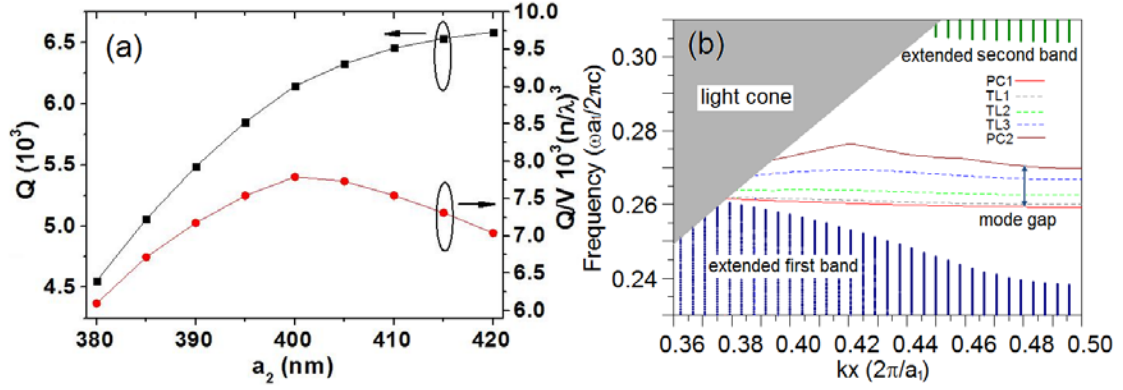


Figure 2.21 (a) The defect lattice constant a_2 is selected at 400 nm for optimized cavity confinement and EO sensitivity. (b) The projected band diagram shows a wide mode gap between PC1 and PC2, which is the origin of the highly confined optical cavity resonance.

to a rectangular lattice [60]. The hole displacement in the x direction is linearly tapered over the TL periods according to the relationship $\Delta x_n = na_1/8$, $n = 1, 2, 3$, where Δx_n is the displacement of the n^{th} column (TL_n) from the adjacent PC1. In the y direction, the lattice constant is homogeneous to satisfy the lattice matching condition.

Then, the cavity is optimized in terms of EO sensitivity η_{EO} , which is defined as the modulation depth achieved per square index change. According to the detailed mathematical calculations in Appendix A, η_{EO} is found to be proportional to $(Q/V_{\text{mod}})^2$ for a specific material system and operating wavelength (Q and V_{mod} are quality factor and mode volume respectively). In Fig. 2.21 (a), the defect period a_2 is first studied and is kept at 400 nm for maximized Q/V_{mod} . Then, the TE-like mode band diagram of the mode gap cavity is calculated by the 3D PWE method and plotted in Fig. 2.21 (b), where the waveguide defect mode is found blue-shifted when the lattice deforms from hexagonal to rectangular through the TL layers, which opens up a mode gap $\Delta f = 7.3$ THz near the projected Brillouin zone edge (scaled up for $a_1 = 410$ nm). According to the 3D FDTD calculation, the gap accommodates a resonance mode at

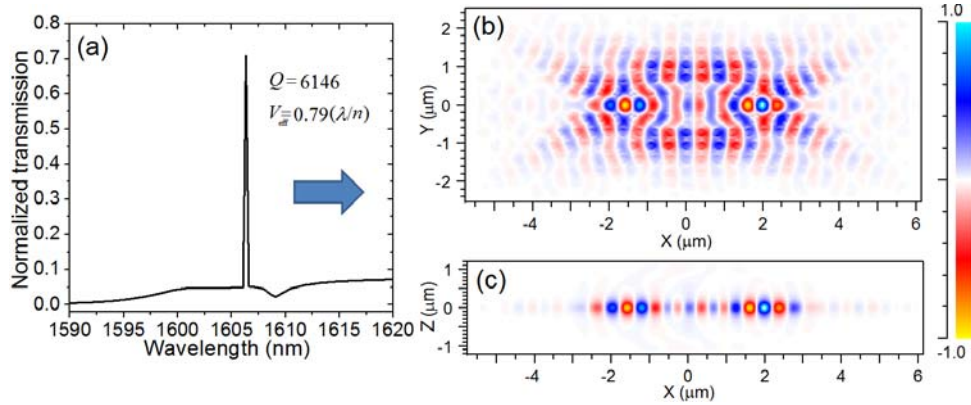


Figure 2.22 (a) Transmission spectrum of the HLMG resonator indicates a highly confined resonance mode in the NIR range. (b) 2D profile of the resonance mode in the xy plane. (c) 2D profile of the resonance mode in the xz plane.

1606 nm with high optical confinement: $Q = 6146$ and $V_{\text{mod}} = 0.79 (\lambda / n)^3$, shown in Fig. 2.22 (a). The mode profiles shown in Fig. 2.22 (b) and (c) indicate two separated field maxima located symmetrically at the PC1-TL boundaries. Each field maximum follows a Gaussian-like mode envelop due to the TL periods and therefore, only a small amount of out-of-plane radiation is detected in Fig. 2.22 (c).

Finally, since the HLMG cavity would normally have high insertion loss due to a group velocity mismatch between the PC waveguide and a conventional ridge waveguide, an additional insertion stage (PC3) has been designed for use between the ridge waveguide and PC1 for a smooth group velocity transition, as illustrated in Fig.2.20 (b). Two approaches were previously proposed about the design of the tapering stage: reduced hole radius [61] and increased lattice constant [40, 62]. To avoid the fabrication error usually related to patterning smaller feature sizes, the latter approach is used here. In Fig. 2.23, both lattice constant a_3 and the number of tapered periods are studied. It is shown that insertion efficiency is about 3% (-15 dB) without tapered lattices (i.e. $a_3 = a_1$) and can be enhanced to 56% (-2.5 dB) with 6 periods of PC3 when $a_3 = 450$ nm, where the defect modes of PC1 and PC2 at resonance frequency are

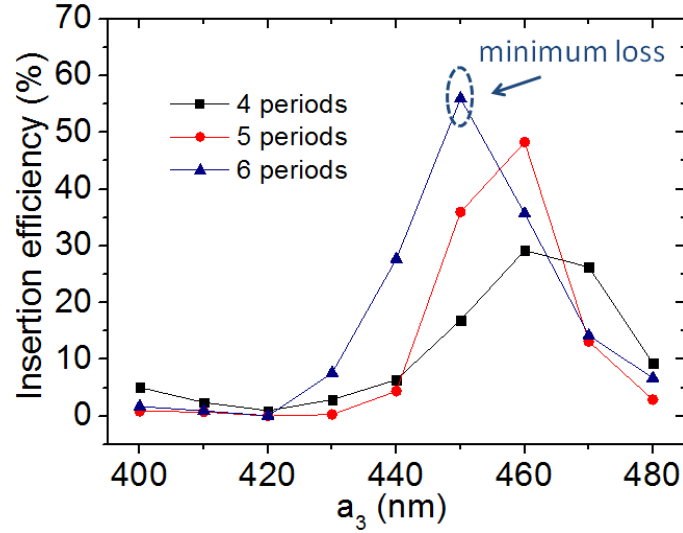


Figure 2.23 Significantly improved insertion efficiency is detected with 6 periods of PC3 when a_3 is kept at 450 nm.

shifted to the fast light regime from the slow light regime. The result found is consistent with previous studies on PCW injectors with tapered lattice constant [40].

Electrically, a P^+PNN^+ diode is created at the cavity center for free carrier based index modulation. It is shown in Fig. 2.24 (a) that the diode is designed asymmetrically in size and dopant concentration with P region extended off center by 117 nm to take advantage of the higher free carrier coefficient of the holes. The highly conductive P^+/N^+ regions are defined by 10^{20} cm^{-3} boron/phosphorous impurities for driving the diode externally while P/N regions are doped to $N_p = 3 \times 10^{18} \text{ cm}^{-3}$ and $N_n = 9 \times 10^{18} \text{ cm}^{-3}$ respectively. The diode width covers 7 periods of SiO_2 holes in the x direction to include only the two resonance field maxima of the cavity mode shown in Fig. 2.24 (b) and (c), which makes a total dopant area as compact as $14 \mu\text{m}^2$. This design is to achieve a maximized overlapped volume between the EO active region and the optical mode while at the same time keep the impurity loss within an acceptable level ($\sim 2.3 \text{ dB}$ for the dopant level specified above). It is important to note that in this work, the planar design of the diode is adopted by using a silicon slab (zero aspect ratio) rather than a high aspect ratio rib waveguide [14, 27, 28]. As compared in Fig. 2.24 (b) and (c), this design will facilitate

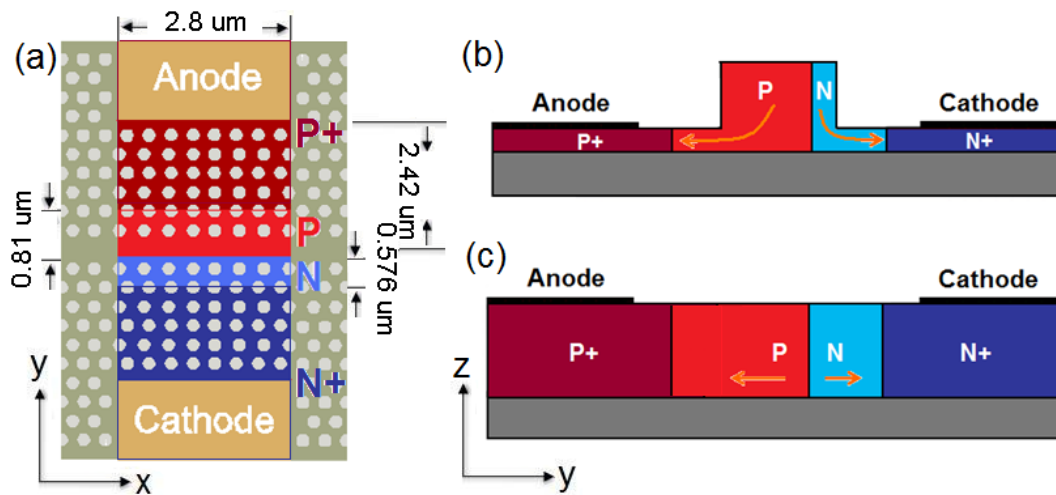


Figure 2.24 (a) 2D schematic of the lateral P^+PNN^+ diode embedded in the HLMG cavity. yz cross section of the embedded diode shows (b) indirect carrier depletion path in a rib waveguide based diode (not recommended) and (c) direct depletion path in the planar diode design that we employ instead.

more efficient carrier depletion/extraction from the central active region by removing the sharp sidewall corners as barriers. Therefore, the carriers take a direct depletion route without significant loss in their momentum when reaching the P^+/N^+ side. The same condition applies to the recovery of the carriers at the center of the P/N region with the release of the external bias. This is also one of the major reasons for the much higher switching speed achieved in the device.

2.4.2. Reduce electrical scattering by lattice transition

The main advantage of the HLMG resonator described in Fig. 2.20 over previously studied double heterostructure (DHS) resonators [40, 58] is that the electrical scattering of the free carriers can be reduced by the rectangular lattices located at the center of the cavity. Although PC-based silicon free carrier modulators have been studied quite extensively [20], the scattering effect of the embedded PC holes/columns to the momentum of the free carriers is still not fully explained either experimentally or theoretically. It is found in this work that the significance of this undesired scattering is dependent on the

lattice pattern of the PC and is large enough to be taken into consideration when predicting free carrier profile under reverse bias. To achieve that, the following work is carried out by the device simulator from ATLAS. The asymmetric P⁺PNN⁺ diode in Fig. 2.24 (a) is reverse biased by a DC voltage swept from 0 to -8 V. In Fig. 2.25 (a), the hole concentration probed near the waveguide center (x=0, y=-50 nm, z=0) is plotted for PC free, HLMG and DHS embedded diodes. The dimension of the DHS cavity is kept according to ref. [40], where the central cavity is formed by one period of hexagonal lattice with a slightly larger lattice constant (a₂=420 nm). It is shown that although much shallower carrier depletion is found in either PC embedded diodes compared to PC free design, carriers are extracted from the P/N region more efficiently for the HLMG cavity at the same bias voltage compared to others. This may come from the different gradients of quasi-Fermi levels (within the depletion region) as well as drift mobility μ of the free carriers in the two cavities. According to Matthiessen's rule [45]

$$\frac{1}{\mu} = \frac{m^*}{q} \left(\frac{1}{\tau_{mi}} + \frac{1}{\tau_{mo}} \right) \quad (2.20)$$

where q and m^* are electron charge and carrier effective mass respectively; τ_{mo} is the mean free time corresponding to the major scattering events (phonon, impurity, etc.) while τ_{mi} is introduced here as the mean free time corresponding to the additional insulator scattering. It is postulated that the lower scattering effect in the HLMG cavity increases τ_{mi} and therefore carrier mobility assuming similar phonon/impurity scattering in both cases. The collective effects are the higher carrier contrast and uniformity. The latter is demonstrated in Fig. 2.25 (b) and (c) for a bias voltage of -8 V, where almost homogenous carrier distribution is found in the HLMG cavity in the x direction while in the DHS cavity, a periodically modulated carrier concentration is found in the same direction. The periodicity of the

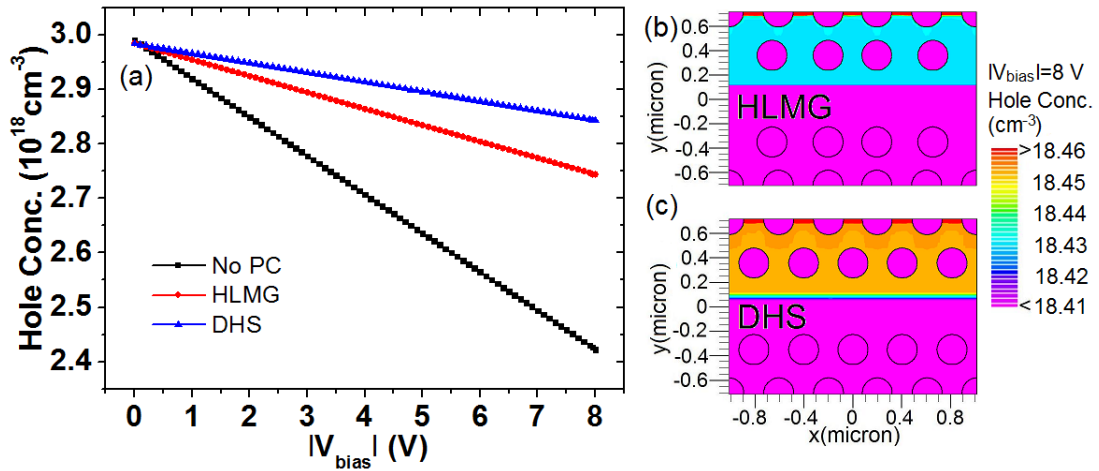


Figure 2.25 (a) Static carrier level near the center of the waveguide shows different hole contrasts at the same bias voltage for diodes embedded in different lattice patterns. 2D hole profiles at -8 V indicate in the x direction (b) highly uniform carrier distribution for the HLMG cavity and (c) periodically modulated concentration for the DHS cavity.

carrier modulation matches that of the embedded PC lattice and therefore can be clear evidence for free carrier scattering and compensation due to the embedded PC lattices.

2.4.3. Breakdown delay-based depletion mode operation

Delayed-breakdown diodes have previously been studied for high power electrical switching and pulse generation. In these types of diode, the “breakdown delay” is caused by a superfast impact ionization front propagating at a speed much higher than the saturated carrier drift velocity [63]. In other words, such diodes would normally breakdown, but have insufficient time to do so in this mode of operation. Till now, this technique has not been applied to optical switching and modulation. In this section, the idea is applied to integrated optical switching by transiently biasing a depletion mode diode *beyond its static breakdown point* before breakdown takes place, i.e. breakdown delay-based depletion mode (BDDM) operation. It is found that high concentration contrast picosecond (ps) level carrier movement can be achieved at the quasi-steady state within either tunneling or avalanche breakdown delay,

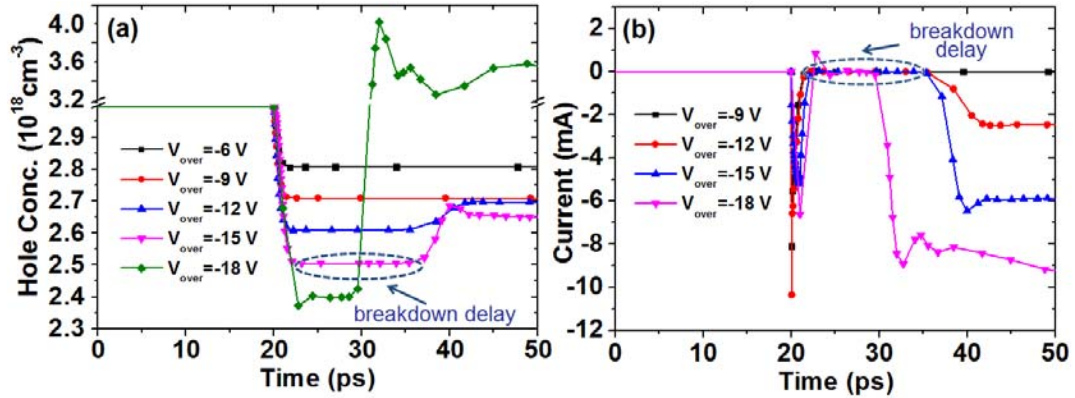


Figure 2.26 (a) A finite breakdown delay time is found in the post breakdown operation regime where the carrier level can be further depleted with increase of the bias voltage. (b) The leakage current is found to be negligible within the breakdown delay and increases drastically after breakdown takes place.

where only negligible leakage current flow is found. The outstanding electrical performance from the new operation regime can be applied to the hybrid lattice resonator based modulator described in Section 2.4.1 to achieve high modulation depth due to the resonance wavelength shift of a cavity mode supported in the photonic resonance medium.

In Fig. 2.26 (a), a negative voltage step is applied to the device for duration much larger than the transit time of the diode. The carrier concentration is probed at the same location as in the previous paragraph. The amplitude of the step is swept from -6 V to -18 V to include all operation regimes of the reverse biased diode. It is shown for low voltage steps $V_{\text{over}} = -6 \text{ V}$ and $V_{\text{over}} = -9 \text{ V}$, stable carrier concentration jumps are detected which indicate conventional DC carrier depletion can be achieved when the voltage is kept much lower than the static breakdown point of the diode. As the magnitude of the reverse step increases to -12 and -15 V, the depleted carrier level only holds for a finite duration before it jumps back to and stays at a higher level. This process can be understood as device breakdown mostly due to a band-to-band tunneling process caused by the bandgap narrowing effect. The critical breakdown field E_m at the depletion region probed is 1.2 MV/cm which is slightly smaller than the theoretical value predicted in silicon abrupt junctions [45]:

$$E_m = \frac{4 \times 10^5}{1 - (1/3) \log_{10}(N / 10^{16})} \quad (2.21)$$

According to Eq. (2.21), a reduced critical field can be caused by the embedded intrinsic PC lattice which reduces the effective dopant level of the P/N region by a factor proportional to the filling ratio of the holes. As the voltage step further increases to -18 V, the DC carrier depletion is even less stable and completely compromised by the avalanche multiplication process after a short period. The carrier analysis of the post breakdown operation is confirmed by the leakage current results shown in Fig. 2.26 (b), where appreciable and significant current flows are detected in tunneling and avalanche breakdown conditions respectively.

Optically, this decreased (or temporally instable) carrier contrast is undesired since it will lead to reduced (or fluctuating) ON/OFF transmission contrast which may in turn result in a higher bit error rate (BER) in PRBS based communication systems. However, still in Fig. 2.26 (a), a finite breakdown delay is detected during which the carrier contrast still increases with the magnitude of the reverse voltage at the same carrier transition speed. In this work, this is called quasi-steady state since it follows the static behavior of the diode under pre-breakdown bias. At a bias voltage of -18 V, for example, the carrier contrast is $6 \times 10^{17} \text{ cm}^{-3}$, which is 2 times the value at -9 V for the same location. Moreover, negligible leakage current ($\sim -10 \text{ nA}$) is found within the breakdown delay in Fig. 2.26 (b). Therefore, it is possible to transiently bias the device beyond its static breakdown point within the delay for a deeper carrier depletion level without sacrificing either switching speed or energy consumption. In the tunneling breakdown case, the breakdown delay Δt_{BT} is measured to be 16 ps, which is associated with the tunneling time of the free carriers governed by the time dependent Schrodinger equation in semiconductor nanostructures [64]. For the avalanche breakdown case, the delay time Δt_{BA} is much shorter ($\sim 7 \text{ ps}$) and is usually interpreted as the avalanche build-up time, which is caused by the high voltage ramp $dV_{\text{over}}/dt = 1.8 \times 10^{14} \text{ V/s}$ from unbiased to reverse biased operation [63]. The voltage ramp needs to

satisfy the critical condition (Eq. (2.22)) in order to excite superfast impact ionization fronts travelling in a velocity that exceeds the saturated drift velocity of free carriers (usually $v_s=1.1\times 10^7$ cm/s) [65]:

$$dV_{\text{over}} / dt > 2v_s \sqrt{qN_B(V_{\text{bi}} - V_{\text{over}}) / 2\epsilon} \quad (2.22)$$

where q and N_B are the electron charge and dopant concentration of the base region where fronts propagate through, respectively; V_{bi} and ϵ are the built-in potential of the junction and permittivity of the material, respectively. For biasing the device around -18 V, the critical voltage ramp is calculated as $\sim 1.5\times 10^{13}$ V/s.

In this work, the biasing point of the device is set within the tunneling breakdown regime for two practical concerns. First, the carrier contrast within the tunneling delay is strong enough to guarantee significant MD in the optical part (10 dB is used as a benchmark for ON state definition); and second, the tunneling delay Δt_{BT} is about 8 times longer than the carrier rise time (~ 2 ps) and therefore safe enough for transmitting a binary sequence of up to 8 consecutive “1”s in a multi-GHz PRBS system without degeneration in signal-to-noise ratio (SNR), whose probability is less than $0.5^8=0.4\%$. Unlike injection mode EO modulators, the carrier distribution is usually not uniform within the depletion region of the reverse biased diode due to the continuously bent quasi-Fermi levels. Therefore, it is necessary to investigate carrier profile within the active region and interpret it into the corresponding index profile for optical transmission study.

In Fig. 2.27 (a) and (b), 2D hole profiles are shown in the xy plane ($z=0$) and yz plane ($x=0$) at $V_{\text{over}}=-15$ V for the quasi-steady state before breakdown. Both carrier profiles indicate a well-presented depletion belt whose width is slightly modulated in the x direction with the periodicity of the embedded PC lattice while uniform in the z direction with the homogeneous electrical medium. To precisely measure the location and width of the depletion region, a 1D outline is made along the y direction at $x=0$, $z=0$ for both holes and electrons. In Fig. 2.28 (a), the hole/electron outline under bias is plotted against the

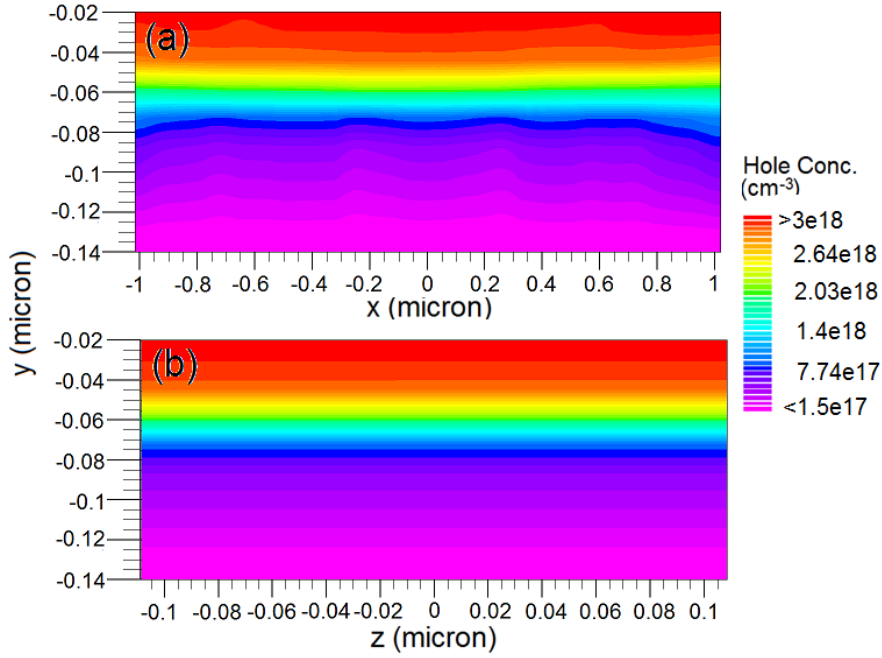


Figure 2.27 Magnified 2D hole profiles at -15 V indicate the depletion region (a) in the xy plane and (b) in the yz plane.

zero bias condition to demonstrate the externally modulated depletion width with respect to the bias voltage, which follows the theoretical model

$$W_D = W_{Dp} + W_{Dn} = \sqrt{\frac{2\varepsilon(N_p + N_n)}{qN_p N_n} \left(V_{bi} - V_{over} - \frac{2kT}{q} \right)} \quad (2.23)$$

It is shown in Fig. 2.28 (a) that the total depletion width increases from 50 to 120 nm when the diode is biased to -15 V. The hole/electron concentration contrast is highly dependent on the y coordinate due to the smooth concentration tails at the boundaries of the depletion region. The peak carrier contrast is detected at $y=-80$ and $y=-125$ nm for holes and electrons, respectively, as shown in Fig. 2.28 (b), where the electron contrast peak is higher due to the higher N_n . However, the hole contrast covers a wider range with the FWHM pulse width $W_{FWHMp}=35$ nm ($W_{FWHMn}=28$ nm) due to the lower N_p . Compared with the mode profile in Fig. 2.22 (b), it is clear that the carrier contrast peaks are completely covered by the

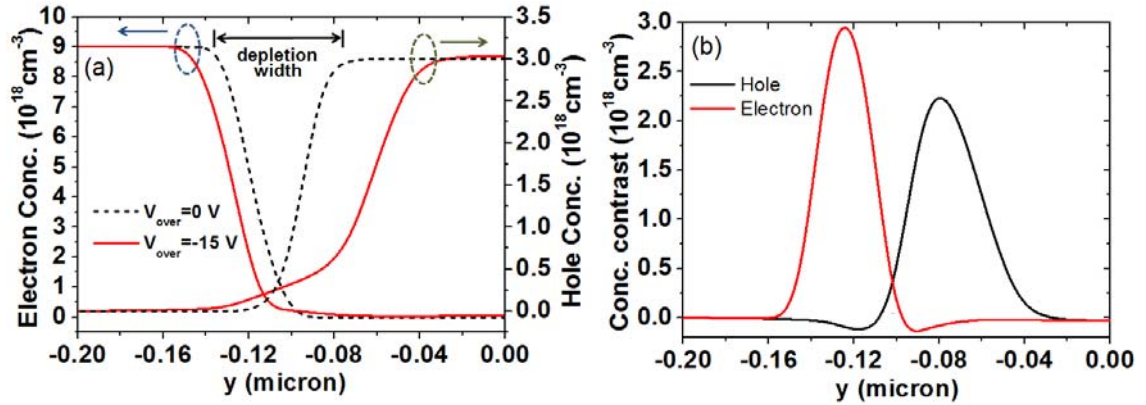


Figure 2.28 (a) 1D cutline of the hole/electron concentration along the y direction indicates the depletion width movement at -15 V bias. (b) 1D carrier contrast profile between 0 and -15 V within the depletion region.

optical field maxima. Therefore, it is possible to further improve the EO sensitivity of the cavity by increasing the depletion width of the diode, which can be achieved by lowering the dopant level of the P/N region.

The dynamic performance of the device is characterized by a voltage pulse with pulse width smaller than the breakdown delay of the diode for quasi-stable carrier depletion. Due to the non-uniform carrier profile in the xy plane, the carrier movement is probed at different locations throughout the active region (within the plane of $z=0$). First, V_{over} is kept at -15 V. It is shown in Fig. 2.29 (a) that the carrier evolution is identical in the x direction while in the y direction, the carrier contrast varies and agrees with the distribution in Fig. 2.27 (b). More importantly, the rise/fall time (10% to 90%) of the carrier transition is almost the same at $t_r = t_f = 2.1$ ps regardless of the probe coordinate, which corresponds to a uniform switching speed of 238 GHz of the device. For depletion mode EO modulators, the upper limit of the device speed f_{UL} is partially determined by the time constant of the equivalent RC circuit, as shown in Fig. 2.29 (b):

$$\begin{aligned}
f_{UL} &\equiv \frac{1}{t_r + t_f} \approx \frac{1}{4.4\tau_{RC}} \\
&= \frac{1}{4.4(R_{p^+} + R_p + R_n + R_{n^+})C_D} \approx \frac{W_D}{4.4\varepsilon(\rho_{effp}L_p + \rho_{effn}L_n)}
\end{aligned} \tag{2.24}$$

where C_D and $R_{p,n}$ are the depletion layer capacitance and P/N region resistance respectively; W_D is given in Eq. (3.26). R_{p^+,n^+} can be neglected since it is much smaller than $R_{p,n}$. Therefore, higher device speed may be achievable with a reduced C_D by lowering the P/N dopant level. However, this would be compensated by an increased P/N effective resistivity $\rho_{effp,n}$. Another way of improving speed is to reduce the dopant length of the P/N region $L_{p,n}$, and overall transmission can be reduced as a tradeoff due to the extended P⁺/N⁺ region.

Apart from the major limitation from carrier rise/fall time, other aspects of the device physics may also play an important role in practical device performance and data capability. For the high Q factor photonic resonator based modulator studied in this section, the photon lifetime $\tau_{ph} = Q/\omega_0 = Q/(2\pi f_0)$, which is around 5.1 ps and close to one modulation cycle of the device operated around 200 GHz. As a result, the photon lifetime imposes additional limitation on the transmission speed that the device is capable of achieving. For more conservative estimation, the upper limit of the device can be calculated from a combined effect of both carrier movement time and photon lifetime $f_{UL} = 1/((\max(\tau_{ph}, t_r) + t_f))$, which means that the rise time of the output signal should be long enough for photons to escape from the cavity center, while fall time of the signal can still be governed by the carrier movement (carrier fall time) since the output signal is cut off almost instantly when the operation wavelength is off resonance. This gives a data transmission speed of around 139 GHz. Another practical limitation may come from the passband bandwidth of the cavity, which is $f_{FWHM} = f_0/Q = 1/(2\pi\tau_{ph})$ and around 30 GHz. In real applications, transmitted data bandwidth is dependent on the actual modulation scheme that is used in a

specific application area. For double-sideband transmission, for example, the data bandwidth will double the base band signal and become 400 GHz in this case (278 GHz for the more conservative estimation). One can notice that the difference between f_{FWHM} and f_{UL} is the $1/2\pi$ scalar that gives even more limited speed estimation and usually ignored in general transmission capacity estimations, such as in ref. [40]. However, for achieving high ON/OFF contrast (modulation depth) against background noises, the full data bandwidth is suggested to fit the FWHM linewidth of the cavity passband and as a tradeoff, this may further sacrifice the transmission capability of the device.

Then, V_{over} is swept from 0 to -15 V to study the tradeoff relationship between bias voltage and MD. At each voltage step, the 2D carrier profile (both for holes and electrons) is interpreted into the index profile for the optical simulator to measure resonance peak shift and transmission contrast. According to Fig. 2.29 (c), while 11 dB ON/OFF contrast can be achieved at -15 V, it is still possible to reduce the voltage to -9 V for a slightly degraded contrast at 7 dB, where the device works at the conventional depletion regime with a similar speed, Fig. 2.26 (a).

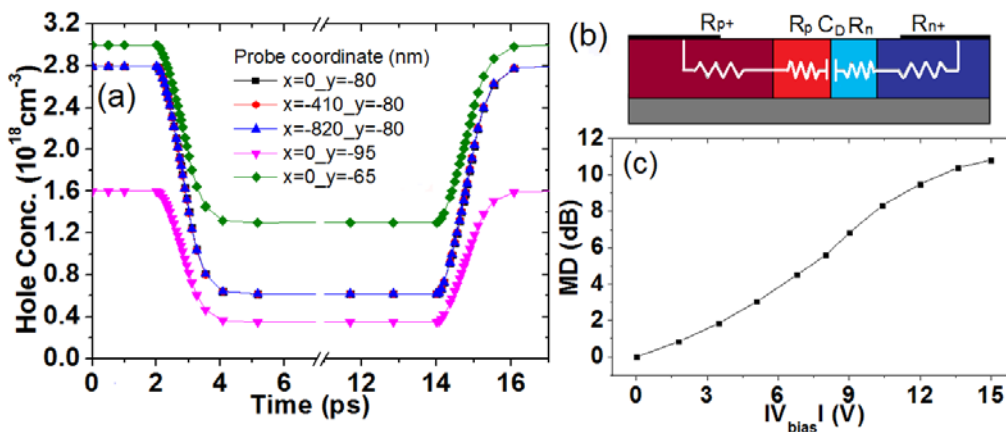


Figure 2.29 (a) The transient carrier response at different locations of the depletion region at -15 V indicates uniform switching speed of 238 GHz. **(b)** Equivalent RC circuit of the embedded P^+PNN^+ diode. **(c)** Tradeoff relationship between MD and bias voltage among different operation regimes.

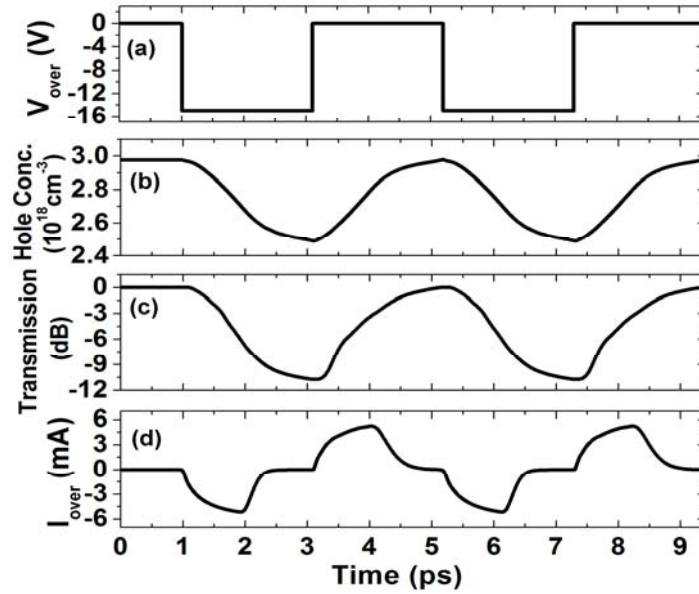


Figure 2.30 (a) The applied 238 GHz RZ voltage signal switching between 0 and -15 V. (b) The representative hole response at the center of the waveguide. (c) The 3D FDTD interpreted transmission evolution of the HLMG resonator corresponding to (b). (d) The transient current flow of the device at voltage transitions.

Then, the device is biased with a 238 GHz RZ signal with $V_{pp}=15$ V, as shown in Fig. 2.30 (a). In Fig. 2.30 (b), the carrier is probed at the center of the waveguide to represent the uniform device speed while the relative transmission and overall current flow are shown in Fig. 2.30 (c) and (d). The transient carrier variation and the corresponding transmission evolution indicates a deeply modulated ($MD>10$ dB) optical signal from the red shift of the resonance peak. In Fig. 2.30 (d), the capacitive I-V characteristic is found at both 0-1 and 1-0 voltage transitions. Since the bit duration here is much longer than the transit time of the diode and yet shorter than the breakdown delay, the AC current cuts off at the end of each bit in a similar way to a step recovery diode (SRD), where abrupt corners are found as carrier depletion reaches the quasi-stable level. Finally, since energy consumption only happens at the 0-1 transition where both current and voltage are non-zero, the averaged energy consumption of the device is calculated as 26.6 fJ per bit through Eq. (2.25) [26]

$$E_{\text{bit}} = 1/4 \int_{0-1} V_{\text{over}} I_{\text{over}} dt \quad (2.25)$$

Due to the material nature of silicon photonic devices, the modulator proposed in this work suffers from thermal-optic instability as $dn/dT=1.8 \times 10^{-4} \text{ K}^{-1}$. The temperature fluctuation may happen both internally or externally. According to the calculated ultra-low energy consumption, the localized heat generation will be at minimum, and mainly concentrated in the EO active region where carrier movement takes place. However, since the RI changes in the same positive direction when both temperature increases and carriers deplete, the slightly generated heat will only increase modulation depth, which leads to performance enhancement. Externally, on the other hand, the high Q cavity based design inevitably results in a narrow optical bandwidth around the FWHM peak width. Therefore, the resonance peak will be sensitive to either environmental temperature fluctuations or fabrication errors. In the former case, a temperature controller can be used to curb the temperature shift within an acceptable range. For the latter, the OFF state voltage is not necessarily kept at 0 V and can be pre-calibrated to pull back the resonance wavelength to its designed value. Depending on the amount of red or blue deviation of the peak spectral position, a positive or negative DC voltage can be applied to the bias tee to compensate for the fabrication imperfections. Then, the device can be driven by the new NRZ signal with a slightly modified V_{pp} .

To sum up, a compact silicon optical modulator has been introduced that functions within a new BDDM operation regime, which enables much higher carrier speed and extraction efficiency with minimum current flow. This mode of operation can be realized in a planar P^+PNN^+ diode embedded hybrid lattice resonator for integrated optical modulation in pure silicon. The demonstrated device speed is as high as 238 GHz at the cost of 26.6 fJ/bit energy consumption. The operation mode combined with the miniaturized photonic medium can eventually lead to the realization of high speed silicon modulation components in a HDPIC and work towards the goal of green photonics.

2.5. Performance summary and comparison

In Tab. 2.2, we summarize and compare the performance of the devices that have been discussed in this chapter. Several major figures-of-merit are selected as performance indicators for EO modulators. First, it is shown that the device footprint increases by about 30 times when the cavity design changes from simple FP resonator to much more complex 2D hybrid lattice resonator. At the same time, the peak-to-peak bias voltage also increases by more than 10 times when the modulation scheme changes from

Table 2.2 Performance summary and comparison between EO modulators studied in Chapter 2.

Structure	FP resonator (injection)	Cross waveguide (injection)	Hybrid lattice resonator (depletion)
Section	2.3.1	2.3.2	2.4
Footprint (μm^2)	2.1	16	69
Speed	300 MHz	2.9 GHz	238 GHz
V_{pp} (V)	1.18	1.65	15
Energy (fJ/bit)	86 $\mu\text{W}/\mu\text{m}$	17.3 mW	26.6
MD (dB)	>10	5.7	10
Loss (dB)	-	1.68 (impurity loss)	2.5 (insertion)

injection to depletion mode. However, it is clear that with 2D photonic crystal cavities with stronger optical confinement, depletion mode operation is made possible which shows a highly improved device speed. More specifically, the device speed improves by almost three orders of magnitude due to the introduction of the breakdown delay-based depletion mode operation. At the same time, the energy consumption of the device is kept ultra-low at 26.6 fJ/bit due to the negligibly small transient current throughout the planar diode. Throughout the studies, a 10 dB modulation depth is kept as a benchmark value to guarantee significant signal to noise ratio and therefore high noise tolerance.

Then, comparison is also made between the best device in this chapter (mainly in terms of speed and energy consumption) and devices studied previously in literature. Some of the major achievements in the development of silicon EO modulators based on PC, ring resonator (RR), or rib waveguide MZI, are listed in Tab. 2.3. As one can tell from Tab. 2.3, the research trend in EO modulator design witnessed a transition from injection/accumulation to depletion mode diode configuration where significant speed improvement is achieved from 1 GHz to 238 GHz in the best design of this chapter. Moreover, nonlinear polymer has also been introduced to form a so-called silicon organic hybrid, based on which high speed/efficiency nonlinear field effects, such as Pockels and Kerr effect, can be incorporated into a pure SOI platform to replace the conventional free carrier effect that is limited by carrier speed and contrast. A price paid for this is a more complicated fabrication process and low fabrication tolerance to narrow slots with smooth side-wall conditions. A more practical concern is the low thermal stability of the state-of-the-art polymers used to build the modulator, whose refractive index can be changed due to the poling effect and become unpredictable to designers when considering impedance and phase matching conditions. Therefore, the overall walk-off frequency can be limited by the amount of the polymer index shift which is determined by a complex combination between poling field, time, and temperature. Finally, for either carrier depletion or nonlinear polymer based design, the DC energy consumption of the device is almost negligible due to either the ~ 0 leakage current in either case. Additionally, the device footprint reduces drastically by more than 100 times when slow light or photonic resonance medium is involved to replace MZI configuration and enhance nonlinear interaction between guided/resonance mode and EO active medium (i.e. free carriers and nonlinear polymers). These two points are especially favorable for high density photonic integrated circuits and green photonics related applications where the energy/heat and footprint budget for each device are extremely limited.

Table 2.3 Detailed device performance comparison between the best device in Chapter 2 and previous work in the literature.

Year	Author	EO structure	Carrier Mechanism	Speed (GHz)	DC Power (mW)	AC Energy (fJ/bit)	Length (μm)
2003	Png [15]	P-I-N/MZI	Inject	1	0.56	N/A	>500
2004	Liu [11]*	MOS/MZI	Accum	1	~0	N/A	10000
2005	Xu [23]*	P-I-N/RR	Inject	1.5	~0	N/A	14
2005	Liao [66]*	MOS/MZI	Accum	10	~0	N/A	3500
2005	Gan [67]	P-I-N/MZI	Inject	24	2500	N/A	1000
2005	Gardes [18]	PN Junction/MZI	Deplete	36	~0	N/A	2500
2007	Liu [13]*	PN Junction/MZI	Deplete	40	~0	N/A	~1000
2009	Dong [27]*	PN Junction/RR	Deplete	100	~0	50	~1000
2009	Gardes [28]*	PN Junction/RR	Deplete	19	~0	N/A	>10
2010	Feng [14]*	PN Junction/MZI	Deplete	12.5	~0	N/A	3000
2011	Xin	PN Junction/Hybrid lattice cavity	Deplete	238	~0	26.6	16

* Fabricated devices

CHAPTER

3. PHOTONIC WAVEGUIDE BASED MODULATORS

3.1. Introduction

The EO modulators presented in the previous chapter are solely based on the free carrier effect, where the transmission contrast at the output side of the waveguide is achieved by localized RI perturbations due to the carrier movement within the active region of the devices. As a result, the speed of the devices is ultimately restrained by transient momentum and recombination velocity of free carriers. By employing the BDDM operation mode in the hybrid lattice resonator configuration (Section 2.4.3), the upper limit of a free carrier effect based EO modulator is pushed where direct depletion route is designed with minimized carrier scattering effect. To further improve device performance, especially operation speed, other NLO media and effects need to be investigated. Recently, EO organic materials, especially nonlinear optical polymers, have attracted increased research attention for realizing high speed integrated optical modulators due to their strong nonlinear coefficients and instantaneous response to electrical field (E-field) [37, 38, 68, 69]. As a result, the so-called silicon organic hybrid is considered a promising platform to provide process and application compatibility with the well developed CMOS industry. In particular, the polymer infiltrated or deposited slot waveguide (SWG) system has been studied intensively, where 170 Gb/s all optical signal processing has been demonstrated [38].

However, the devices proposed previously mostly rely on strong optical confinement within a nonlinear slot in such a way that extremely high EO overlap can be achieved for optimized modulation efficiency [30, 33]. This usually involves narrowing down the slot width and reducing the slab thickness to keep a high aspect ratio slot waveguide geometry, which is extremely challenging even for state-of-the-art nano-fabrication techniques. More importantly, the device speed can therefore be significantly limited by the large slot capacitance and slab resistance due to RC limitations. Therefore, in this chapter, a

polymer P-S-N diode capacitor structure is studied that is, for the first time, able to combine the advantages of both nonlinear Pockels and free carrier effect. Based on that, a much higher device speed is achieved with a compact device footprint and ultra-low energy consumption.

To be more specific, in Section 3.2, numerical methods involved in the design of the polymer P-S-N diode capacitor modulator are first introduced. Then in Section 3.3, detailed discussions of the device design, operation mechanism, and performance analysis are provided with numerical backups. Finally in Section 3.4, a performance conclusion and comparison is made between the device studied in this chapter and some of milestone achievements made in this field previously.

3.2. Numerical methods and techniques

In this section, both optical and electrical numerical methods are described that have been used for modeling waveguide based optical devices particularly for EO modulation purposes. On the optical side, instead of the FDTD method, the beam propagation method is used to model devices with dimensions above the order of $10^3 \mu\text{m}$, such as the rib waveguide based MZI modulators/phase shifters studied in this chapter [70]. The main reason is that the FDTD method calculates propagation behavior of the optical mode based on each discretized time step, which needs to be smaller than the Courant limit that is determined by the grid sizes in the x, y, and z directions. For large devices, the resultant computation time will be impractically long for single simulation to complete. Also, the memory required usually exceeds the hardware capacity of a normal workstation. Therefore, the usefulness of the method is limited to compact devices with the largest dimension smaller than $\sim 10 \mu\text{m}$. The BPM method, on the other hand, is conceptually straightforward, allowing rapid implementation of the basic technique. In addition to its relative simplicity, BPM is generally a very efficient method, and has the characteristic that its computational complexity can, in most cases, be optimal, that is to say the computational effort is directly proportional to the number of grid points used in the numerical simulation. Therefore, this

method is especially useful for calculating devices whose structure is homogeneous in the propagation direction and the resultant reflection is only negligible.

On the electrical side, the ATLAS device simulation suite is also used to model carrier movement and electric field evolution for the polymer slot waveguide studied in Section 3.3. Since this part of the work is similar to that has been described in Section 2.2.3, so the details are not repeated here. The only difference is that since the slot waveguide structure is homogeneous in the propagation direction, only 2D electrical modeling is needed for the device cross section perpendicular to the propagation axis. Also, regarding the physical models, the band-to-band tunneling and Selberherr impact ionization model are not required.

3.2.1. Beam propagation method for rib waveguide based MZI modulators

The BPM is most useful for calculation of mode profile within a waveguide which is homogeneous in the propagating direction since conventional BPM does not take into consideration the reflected wave components [71] (Bi-directional BPM is recently proposed that treats reflected waves as separate, though coupled, part of the problem). The result is time-independent and only reliable when a convergence is achieved before the total length of propagation. Theoretically, scalar BPM is a particular approach for approximating the exact wave equation for monochromatic waves, and solves the resulting equations numerically. The approximation here is the scalar field assumption which allows the wave equation to be written in the form of the well-known Helmholtz equation for monochromatic waves:

$$\frac{\partial^2 \phi}{\partial x^2} + \frac{\partial^2 \phi}{\partial y^2} + \frac{\partial^2 \phi}{\partial z^2} + k(x, y, z)^2 \phi = 0 \quad (3.1)$$

Here the scalar electric field has been written as $E(x, y, z, t) = \phi(x, y, z)e^{-i\omega t}$. Aside from the scalar assumption, the above equation is exact. Considering that in typical guided-wave problems the most rapid variation in the field is the phase variation due to propagation along the guiding axis, and assuming that

axis is predominantly along the z direction, it is beneficial to factor this rapid variation out of the problem by introducing a so-called slowly varying field u via the approximation

$$\phi(x, y, z) = u(x, y, z)e^{-i\bar{k}z} \quad (3.2)$$

Here, \bar{k} is a constant number to be chosen to represent the average phase variation of the field ϕ , and is referred to as the reference wavenumber. At this point the above equation is completely equivalent to the exact Helmholtz equation, except that it is expressed in terms of u . It is now assumed that the variation of u with z is sufficiently slow so that the first term above can be neglected with respect to the second; this is the familiar slowly varying envelope approximation and in this context it is also referred as the paraxial or parabolic approximation. With this assumption and after slight rearrangement, the above equation reduces to:

$$\frac{\partial u}{\partial z} = \frac{i}{2\bar{k}} \left(\frac{\partial^2 u}{\partial x^2} + \frac{\partial^2 u}{\partial y^2} + (k^2 - \bar{k}^2)u \right) \quad (3.3)$$

Based on that, polarization effects can be included in BPM by recognizing that the electric field E is a vector, and starting the derivation from the vector wave equation rather than the scalar Helmholtz equation [72].

The detailed simulation procedures are listed below. Here, we use the polymer infiltrated P-S-N diode capacitor (Section 3.3) as an example. To begin with, the device structure is defined in the graphic user interface of the RSoft design suite in a similar way to the FDTD method described in Section 2.2.1, so the details are not repeated here. Then, the major BPM simulation parameters need to be specified. First of all, since the calculated mode profile and the associated effective index are highly sensitive to the grid size in the x , y , and z directions, the grid sizes need to be first optimized for a converged mode profile and effective index. Then, the optimized grid sizes should be used throughout the study for reasons of consistency. The BPM option is selected to be semi-vectorial which differentiates TE-like and TM-like mode calculation in a separate way. Therefore, interference between the two modes is not taken into account, which is consistent with practical experiments with the polarization of an incident wave being

precisely controlled by a polarizer [70]. Then in the mode options, the numerical method is set as iterative which is recommended for most standard waveguide problems to calculate the less-radiating fundamental mode. The effective index tolerance is the convergence criterion used in the BPM iterations, which is set to 10^{-7} and much smaller than the smallest effective index change from EO modulation. Last but not least, the boundary condition is set to transparent in order to let the radiated mode intensity leave the computation domain so that the radiation loss can be taken into consideration when calculating the total propagation loss of the waveguide.

3.3. Polymer-infiltrated P-S-N diode capacitor based EO phase shifter

In this section, we propose and study a polymer infiltrated P-S-N (“S” refers to the slot) diode capacitor structure for EO phase shifters. In the new configuration, an optical phase shift is realized based on index perturbation both inside the slot via Pockels nonlinearity [40] and within the silicon ridges via the free carrier effect (carrier depletion) [28] simultaneously. Therefore, the overall EO overlap can be noticeably improved from the one that relies on either of the individual NLO effects alone (Section 3.3.1). Additionally, the device speed can be significantly elevated with the introduction of free carriers as they are found to respond faster to the external driving signal than the E-field due to the smaller experienced transient capacitance. By correctly choosing the suitable polarization type for propagation, the advantage of this improved EO overlapped volume as well as the response speed can be applied, for example, to a class of low aspect ratio slot waveguides, which are also studied in this work to improve the modulation speed by reducing the time constant of the small signal equivalent circuit. According to the numerical results, the combination of the polymer diode capacitor configuration with the low aspect ratio slot waveguide system leads to a promising method of constructing sub-THz speed optical modulators without sacrificing either modulation efficiency or energy consumption. To be more specific, by optimizing the waveguide geometry (Section 3.3.2) in terms of a balance between effective index shift and device speed,

at least 269 GHz bandwidth can be achieved with a high modulation efficiency of 5.5 V-cm when the diode capacitor is reverse biased by an external radio frequency (RF) voltage signal between the electrodes (optical propagation loss is acceptably low at 4.29 dB). The device FOMs are found encouraging enough when compared to either depletion mode or polymer SWG based designs (Section 3.3.3). These are conservative numerical results, and as will be shown, are grounded in well-understood physical phenomena.

Admittedly, since the device is based on the less tightly confined TM-like mode propagation, its overall EO conversion efficiency may still be considered less competitive than that of the slot waveguide only optimized for Pockels nonlinearity. This may lead to a larger device length and/or propagation loss. However, the original and ultimate motivation of the proposed structure is to explore and demonstrate a way of constructing a low cost high speed (269 GHz bandwidth) modulation component where for the first time, the RC limitation may no longer be the bottleneck for RF response so that the potential of the ultra-high bandwidth polymers can be unleashed. While at the same time, by optimizing the waveguide geometry, it is still possible to keep the device length comparable to the conventional polymer phase shifters and propagation loss acceptable for optical communication purposes. Additionally, it can be experimentally important that the device does not rely on the high aspect ratio sidewall condition of the slot, which gives considerable fabrication tolerance in terms of nano-patterning, etching, and cladding (infiltration). Instead, the major portion of the SWG cross section is engaged to explore the ultimate limitation of the multiple EO overlaps within the waveguide for highly efficient modulation purposes. Therefore, the usefulness of the electrical configuration shown here in the polymer infiltrated P-S-N profile can also be applied to slow light or optical resonance media, e.g. RRs, to realize much more compact silicon modulation/switching [23] and lasing [73] components that are more suitable for photonic integrated circuits. Additionally, the device consumes almost zero DC energy and ultra-low AC energy (5.83 picojoules per bit, pJ/bit).

3.3.1. Device structure and EO overlap

The phase shifter is based on a strip-loaded vertical slot waveguide, where a thin silicon slab ($n_{\text{si}} = 3.472$) is maintained as the EO active channel at the Si/SiO₂ interface. Electrically, a lateral P-S-N diode capacitor is embedded into the vertical slot waveguide by introducing high level anti-symmetric (opposite types of) impurities into the left and right silicon wings. As shown in Fig. 3.1 (a), the whole P/N silicon wing is divided into three parts with an ascending level of boron/phosphorous impurity from central slot to side electrodes (denoted as P/N, P⁺/N⁺, and P⁺⁺/N⁺⁺ regions respectively). Finally, the waveguide and the slot are completely covered and infiltrated with the NLO polymer ($n_{\text{poly}} = 1.54$ for the AJSP-series EO polymers [32], Pockels coefficient $r_{33} = 65$ pm/V) in the following simulations.

Previously, both uniform and symmetric impurity profiles (same type of dopant is used in both left and right silicon wings) have been incorporated into high aspect ratio slot waveguide based polymer modulators only to reduce the resistance of the silicon thin slab [74]. This kind of device relies on strong optical confinement for TE-like polarization (E-field mostly in the x direction) in a vertical slot or TM-like polarization (E-field mostly in the y direction) in a horizontal slot. In either case, the effective index change of the fundamental mode is highly sensitive to the overlap integral of the optical intensity within the slot and the group velocity of the guided mode:

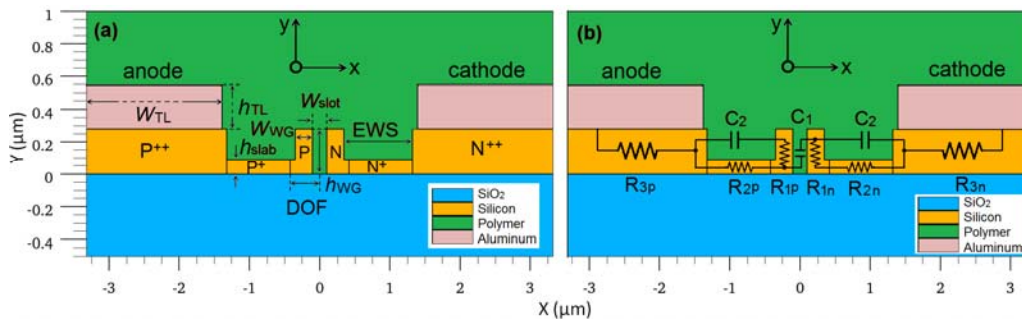


Figure 3.1 (a) 2D schematic cross section of the device showing the lateral polymer infiltrated P-S-N diode capacitor configuration. (b) The small signal equivalent circuit corresponding to (a) showing the RC limitation of the phase shifter.

$$\Delta n_{\text{eff}} = \Gamma_S \Delta n_{\text{poly}} = \frac{n_g}{n_s} \frac{\iint_S \varepsilon |\mathbf{E}|^2 dx dy}{\iint_{\infty} \varepsilon |\mathbf{E}|^2 dx dy} \Delta n_{\text{poly}} \quad (3.4)$$

where Γ_S is the confinement factor of the slot; n_g and n_s are the group index of the mode and bulk index of the active region (slot) respectively [36, 73]. Δn_{poly} is the refractive index change of the polymer caused by the electrical biasing field

$$\Delta n_{\text{poly}} = n_{\text{poly}}^3 r_{33} E_{\text{bias}} / 2 \approx n_{\text{poly}}^3 r_{33} V_{\text{bias}} / 2W_{\text{slot}} \quad (3.5)$$

where V_{bias} is the external bias voltage. As one can tell from Eq. (3.4), only a minor portion of the total waveguide cross section is EO active and hence responsible for the effective index and phase shift, which results in a limited EO conversion efficiency.

Compared to the symmetric impurity profile, the anti-symmetric dopant scheme, i.e. the P-S-N diode capacitor, not only reduces potential drop within the silicon wings, but more importantly, enables high level fast carrier depletion within the silicon ridge, where the free carrier index shift can be added constructively to the Pockels index shift of the polymer by correctly aligning the direction of the poling field with the diode capacitor (in the negative x direction for the configuration shown in Fig. 3.1 (a)). Hence, the overall effective index change of the guided mode can be increased to

$$\Delta n_{\text{eff}} \equiv \Delta n_{\text{eff,poly}} + \Delta n_{\text{eff,si}} = \frac{n_g}{n_s} \frac{\iint_S \varepsilon |\mathbf{E}|^2 \Delta n_{\text{poly}} dx dy}{\iint_{\infty} \varepsilon |\mathbf{E}|^2 dx dy} + \frac{n_g}{n_R} \frac{\iint_R \varepsilon |\mathbf{E}|^2 \Delta n_{\text{si}} dx dy}{\iint_{\infty} \varepsilon |\mathbf{E}|^2 dx dy} \quad (3.6)$$

where n_R is the bulk index of the silicon ridges. The total index change consists of two parts, $\Delta n_{\text{eff,poly}}$ and $\Delta n_{\text{eff,si}}$, from Pockels effect inside the nonlinear slot and free carrier effect within the P/N silicon ridges respectively. Δn_{si} is the localized silicon index change from the Drude-Lorenz model and at a wavelength of 1.55 μm formulated in Eq. (1.3), which is repeated here in Eq. (3.7).

$$\Delta n_{\text{si}} = -8.8 \times 10^{-22} \Delta n_{\text{e}} - 8.5 \times 10^{-18} (\Delta n_{\text{h}})^{0.8} \quad (3.7)$$

where Δn_{e} and Δn_{h} are electron and hole contrast, respectively. In Eq. (3.6), both Δn_{poly} and Δn_{si} are inside the numerator integration because of the non-uniform biasing field and carrier contrast distribution within the nonlinear slot and silicon ridges respectively. Consequently, both P/N region and the slot are EO active in the P-S-N diode capacitor configuration, where the overwhelming majority of the optical intensity is confined. Therefore, the total EO overlapped volume can be increased significantly due to the presence of multiple EO active media.

Although the EO response of the $\chi^{(2)}$ nonlinear polymer is almost instantaneous (\sim femtoseconds [75], fs), the upper frequency limit of the polymer SWG modulator f_{UL} lies in the transient evolution of the biasing field E_{bias} inside the slot, which is partially governed by the RC time constant τ_{RC} of the small signal equivalent circuit. According to Fig. 3.1 (b), the speed limitation can be formulated as

$$f_{UL} = \frac{1}{2\pi\tau_{RC}} = \frac{1}{2\pi \sum_{i=1}^3 (R_{ip} + R_{in}) C_1} \approx \frac{W_{\text{slot}} h_{\text{slab}}}{2\pi\epsilon_{\text{poly}} (\rho_{p^+} L_{p^+} + \rho_{n^+} L_{n^+}) h_{WG}} \quad (3.8)$$

where ρ_{p^+,n^+} and L_{p^+,n^+} are the resistivity and length of the P⁺/N⁺ region respectively. Therefore, to unleash the speed potential by reducing τ_{RC} , the slot capacitance C_1 and slab resistance $R_{2p,n}$ need to be further reduced, which can be achieved by increasing the slot width W_{slot} and/or slab thickness h_{slab} relative to the waveguide height h_{WG} as one can tell from Eq. (3.8). This results in so-called low aspect ratio slot waveguides. To start with, the slot width and slab thickness are kept at 200 and 90 nm respectively in the reference model (RM), and the rest of the geometric and dopant parameters shown in Fig. 3.1 (a) are listed in Tab. 3.1.

Table 3.1 List of the major design parameters in the RM device.

Name	Description	Value (RM)	Unit
W_{slot}	nonlinear slot width	200	nm
h_{slab}	silicon slab thickness	90	nm
h_{WG}	waveguide ridge height	280	nm
W_{WG}	waveguide ridge width	245	nm
W_{TL}	electrode width	50	μm
h_{TL}	electrode height	10	μm
EWS	electrode-waveguide spacing	1	μm
DOF	dopant offset from the waveguide center	420	nm
N	dopant concentration of the P/N region	10^{17}	cm^{-3}
N^+	dopant concentration of the P^+/N^+ region	5×10^{17}	cm^{-3}
N^{++}	dopant concentration of the P^{++}/N^{++} region	10^{20}	cm^{-3}

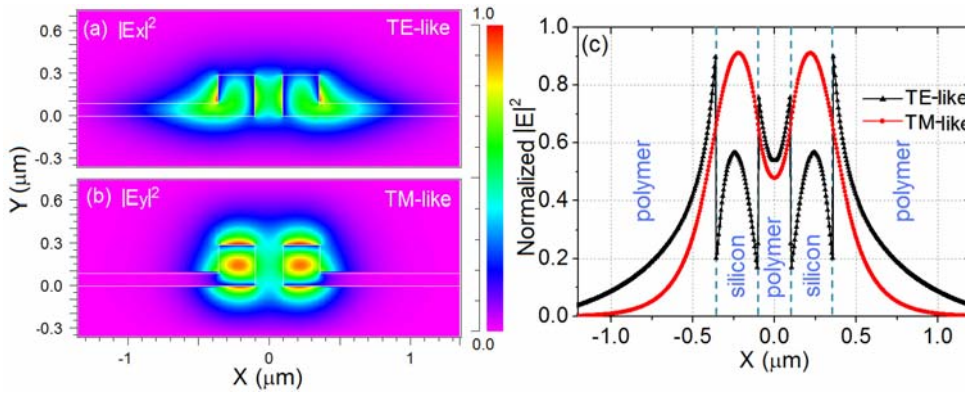


Figure 3.2 The fundamental mode profile cross section of the RM SWG: (a) TE-like polarization and (b) TM-like polarization. (c) E-field intensity cutlines of the TE-like and TM-like mode profiles in the x direction across the waveguide center, which show a large portion of the total intensity located within the silicon ridges.

In Fig. 3.2 (a) and (b), the fundamental mode of the RM waveguide is calculated for both TE-like and TM-like polarizations using a 3D semi-vectorial BPM [18, 76], which is accurate enough for calculating each polarization separately instead of the coupling between them [70]. One can tell that in the case of either polarization, the E-field intensity is weakly confined in the central slot and penetrates extensively into the silicon ridges and slabs. In Fig. 3.2 (c), the intensity cutline at the waveguide center ($y=0.14 \mu\text{m}$) indicates that the nonlinear slot only confines 16.1% of the total intensity for the TE mode and 14.9% for the TM mode, while 28.6% and 55% of the total intensity are distributed in the left and right silicon ridges for TE- and TM-like modes, respectively. Therefore, it is clear that by incorporating

the P-S-N diode capacitor configuration, a larger portion of the optical intensity within the silicon ridges can be engaged in the free carrier based EO medium to compensate for the degraded slot confinement factor associated with the low aspect ratio slot waveguide design.

To illustrate the point, the device is reverse biased by an external DC voltage signal (-10 V is used as a benchmark voltage in the following study unless stated otherwise) between the electrodes, and the E-field and free carrier distributions are predicted by the electrical device simulator from ATLAS. In Fig. 3.3 (a), highly confined E_{bias} distribution is found within the nonlinear nanogap (only the x component is plotted and is responsible for the EO effect) although a higher degree of non-uniformity is detected due to the widened slot. On the other hand, a sizable depletion region is found in the carrier profile in Fig. 3.3 (b) (only hole profile is plotted due to the dopant anti-symmetry). The width of the carrier depletion layer in Fig. 3.3 (b) is ~ 100 nm and is larger than that of the accumulation layer reported previously in forward bias operation [16], which is limited to $C_1 V_{bias} / \Delta n_{e,h}$. The corresponding EO index shift profiles due to the Pockels and free carrier effects are calculated and are shown in Fig. 3.3 (c) and (d), respectively. In Fig. 3.3 (d) in particular, the profile shows a combined index shift from both hole and electron depletion (electron depletion is not plotted here since it is the mirror image of the hole depletion), where an asymmetric Δn_{si} profile is found in the left and right silicon ridges due to the larger free carrier coefficient for holes, shown in Eq. (3.7). The Δn_{si} profile is calculated from the carrier profile under bias since the depletion width at zero bias is negligibly small (discussed in the paragraphs below). However, unlike rib waveguide based EO active components [14, 28], it is not viable to take advantage of the higher index perturbation efficiency of the holes by extending the P region into the N region because of the polymer nanogap, which acts as an optical barrier for mode intensity to change continuously in the x direction. As

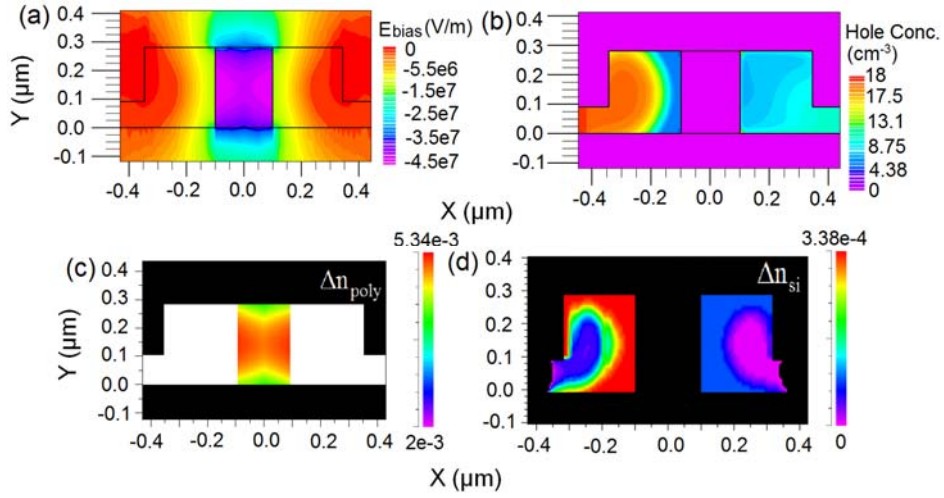


Figure 3.3 (a) E-field (x component) profile within the nonlinear slot when the diode capacitor is reverse biased. (b) Free carrier (hole) concentration profile within the silicon ridges under the same bias. (c) Localized index perturbation corresponding to (a) via Pockels effect. (d) Localized index perturbation corresponding to a combined effort of hole and electron depletion via free carrier effect (the value below the lower end of the color scale is shown in black).

a result, the confinement factor will decrease quickly while propagation loss increases for an unbalanced P/N region. Finally, although the localized index change from free carrier effect is much smaller than that from the Pockels effect (comparing Fig. 3.3 (c) and (d)), the relative contribution of these two effects to the overall effective index change also depends on the mode distribution according to Eq. (3.6) and therefore can be very different from the respective localized index change within each governing domain (explained in detail in the paragraphs below).

3.3.2. Parameter study and optimization

The two most sensitive geometrical parameters of the low aspect ratio slot waveguide, i.e. slot width W_{slot} and slab thickness h_{slab} , are next studied for optimized tradeoff between individual FOM of the device while other parameters are fixed according to Table 3.1. Although TE-like polarization is usually preferred for strong optical confinement in vertical slot waveguide systems, the low aspect ratio design

proposed in this work may cause significant deformation in its mode shape so that its suitability for propagation and switching can be highly dependent on the respective geometrical dimensions. In this regard, both TE-like and TM-like polarizations are first considered when studying the effect of W_{slot} on the effective index change Δn_{eff} , device speed, and propagation losses. The same physically based modeling is used here to predict both static carrier distribution and dynamic carrier movement within the silicon waveguide as well as the biasing field profile within the nonlinear slot. The 2D E-field and free carrier profiles are then interpreted into Δn_{poly} and Δn_{si} profiles using Eq. (3.5) and (3.7), which are inserted into the 3D BPM simulator for the calculation of Δn_{eff} and losses. In this section, the dynamic carrier movement is used to represent device speed since similar trends are found in the E-field evolution when geometric parameters are varied.

First, the W_{slot} is scanned from the lower fabrication limit of 120 nm up to 300 nm while h_{slab} is kept at 90 nm. It is shown in Fig. 3.4 (a) that higher Δn_{eff} (ON state is defined by -10 V) can be achieved in TE-like modes when the slot width is pushing the lower limit, where high EO overlap is available through strong optical confinement within the slot as suggested in previous studies [33]. However, as W_{slot} increases, its index change reduces quickly and becomes smaller than that of the TM-like modes when W_{slot} exceeds 160 nm. This reduction in the effective index of the TE-like mode can be partially explained by the reduced overlap between mode intensity and the nonlinear slot. In Fig. 3.4 (b), it is shown that the intensity fraction within the slot decreases from 20% to only 8% for TE-like polarization while the same fraction increases from 10% to ~20% for the other polarization. Since the nonlinear coefficient is higher for the polymer than the free carriers at the same bias voltage, the overall effect is a degraded Δn_{eff} . As a result, it is clear that TM-like polarization is more suitable for high efficiency EO modulation in the low aspect ratio slot waveguide systems, which is somewhat counter-intuitive for vertical slot waveguide systems. Still in Fig. 3.4 (a), the polymer component of the effective index change $\Delta n_{eff,poly}$ is also plotted which is

derived from a symmetric dopant profile waveguide (same geometrical dimensions) with the absence of carrier movement. One can tell, for either polarization, that the total index is improved noticeably with introduction of carrier depletion by the P-S-N diode capacitor profile. In particular, for the TM-like polarization, Δn_{eff} is optimized at 1.78×10^{-4} when W_{slot} is kept at 240 nm, where the free carrier effect contributes 45.2% of the total index change due to the large portion (49.3%) of the optical intensity confined within the left/right silicon ridges. For W_{slot} above 240 nm, the optical mode becomes more and more weakly confined within the silicon ridges as an increasing portion of the evanescent field penetrates and interacts with the cladding polymer, which causes an overall decrease in Δn_{eff} although the intensity fraction in slot keeps increasing gradually, as shown in Fig. 3.4 (b). It is also worth noting that $\Delta n_{\text{eff,poly}}$ does not follow exactly the same trend as intensity fraction within the slot during the slot width scan. This is because effective index shift from the polymer is also proportional to the group index of the guided mode, Eq. (3.6). As a result, it is shown in Fig. 3.4 (a) that the $\Delta n_{\text{eff,poly}}$ decreases when W_{slot} goes beyond 270 nm (TM-like) due to the faster decrease of the group index (widened slot with lower index) although the intensity fraction continues to increase.

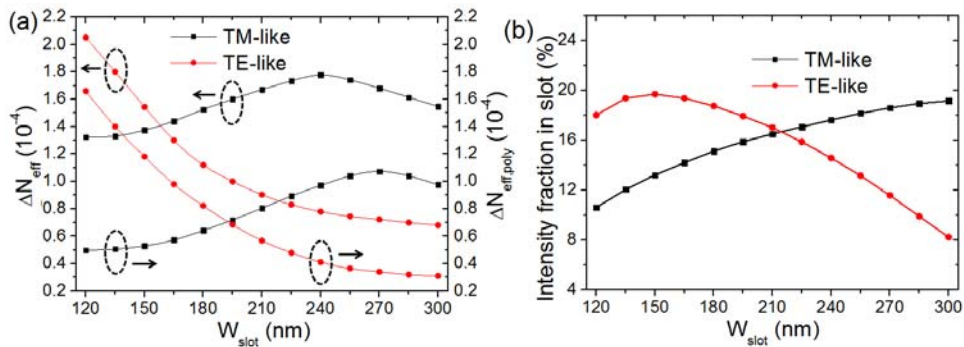


Figure 3.4 (a) Δn_{eff} and $\Delta n_{\text{eff,poly}}$ changes when W_{slot} is varied for both TE- and TM-like polarizations. (b) Change of the intensity fraction within the slot for both polarizations when W_{slot} is swept over the same range.

On the other hand, the device speed is predicted by one carrier movement cycle (depletion and recovery) within the silicon waveguide. The carrier concentration information (only hole concentration is plotted as the electron concentration is its mirror image) is taken inside the depletion region ($x = -0.05 - W_{slot}/2$, $y = 0.14$, in μm) to make sure the dynamic behavior of free carriers are monitored at the same location relative to the edge of the slot, where complete carrier depletion can be achieved and therefore a fair speed comparison can be drawn at the same ON/OFF concentration contrast level. According to Fig. 3.5, the 10% to 90% carrier rise time (during which carriers deplete from 90% to 10% of their unbiased level) is almost fixed at 1.1 ps while fall time (during which carriers recover from 10% to 90% of their unbiased level) reduces significantly from 4.3 to 2 ps when W_{slot} increases from 120 to 300 nm. The improvement in the carrier response time agrees well with Eq. (3.8) and therefore confirms that the RC speed limitation can be relieved by reducing the slot capacitance in the low aspect ratio design. The fact that the fall time improvement is much larger than the rise time through the geometric modification reflects the different carrier mechanisms involved within one operation cycle. When the reverse voltage is released at the falling edge, the device undergoes a process akin to the accumulation

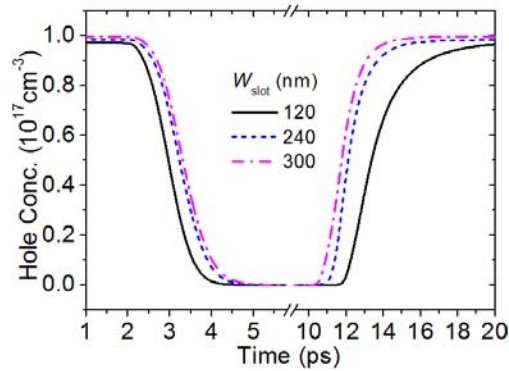


Figure 3.5 The carrier concentration evolution with time indicating a reduced device response time with an increase of W_{slot} .

phase. This will inevitably cause a slower response compared to the rise time, during which the device experiences the depletion phase. The unbalanced effect is more pronounced when the geometry approaches the high aspect ratio end where the RC limitation is more significant.

Considering both optical and electrical performance, W_{slot} is kept at 240 nm as a tradeoff between speed and effective index change. Then the slab thickness h_{slab} is varied from 50 to 170 nm for TM-like mode propagation. Unlike the relationship found in W_{slot} , it is shown in Fig. 3.6 (a) that Δn_{eff} decreases monotonically as the slab thickness increases and more quickly when h_{slab} exceeds 130 nm, which is around half the waveguide height h_{WG} . It can be said from the mode profile that an increasing portion of the total intensity is found in the silicon slab as it becomes more and more prominent, where the localized index change Δn_{si} is at minimum according to Fig. 3.3 (d). Hence, the EO overlap between optical mode and free carrier perturbation is reduced. On the other hand, the total propagation loss consists of two parts: free carrier absorption and radiation loss [77]. In the BPM calculations, the absorption effect due to the high dopant levels is included in the material property through the imaginary part of the refractive index, where the absorption coefficient is derived from the Drude-Lorentz relationship. The Eq. (1.3) is repeated here in Eq. (3.9).

$$\Delta\alpha_{si} = 8.5 \times 10^{-18} \Delta n_e + 6.0 \times 10^{-18} \Delta n_h \quad (3.9)$$

The radiation loss mainly results from coupling of the evanescent field of the guided mode into the polymer cladding and/or the buried oxide layer, which is taken into consideration by specifying full transparent boundary condition to effectively let the radiated intensity pass the boundary and leave the computation domain [70]. As a result, it is shown in Fig. 3.6 (a) that the total propagation loss increases rapidly with h_{slab} partially due to the fact that a larger portion of the optical intensity is distributed within the silicon slab (P^+/N^+ region), where the impurity absorption is much higher according to Eq. (3.9). The larger propagation loss also comes from the higher radiated intensity into the polymer cladding due to the

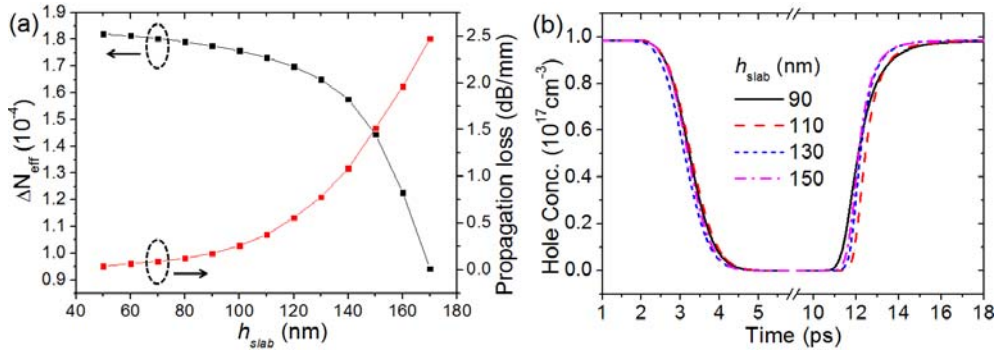


Figure 3.6 (a) Δn_{eff} decreases as propagation loss increases with an increase of h_{slab} . (b) The device response time further reduces with an increase of h_{slab} .

weaker lateral confinement inherent in the lower aspect ratio geometry. On the dynamic side, the rise time changes only slightly with an increase of h_{slab} while the fall time continues to decrease from 2.2 to 1.3 ps, which comes from the reduced slab resistance $R_{2p,n}$ formulated in Eq. (3.8). As a tradeoff between Δn_{eff} and speed, h_{slab} is kept at 130 nm where the propagation loss is acceptably low at 0.78 dB/mm.

3.3.3. Modulation performance and transmission line design

Then, the EO modulation and microwave (driving signal) propagation behavior of the device is discussed based on the optimized phase shifter from previous discussion. First, it is found that free carriers respond faster to the external RF voltage signal than the E-field due to the smaller depletion layer capacitance for the former, which reemphasizes the importance of the introduction of free carriers to further improve device speed as well as modulation efficiency. Then, both static (DC) and dynamic (AC) performance of the device are characterized, where the tradeoff relationship between phase shift and bias voltage as well as the dynamic energy consumption of the device are analyzed in detail. Finally, practical concerns regarding microwave propagation (impedance and phase matching conditions) are addressed by

proper design of the transmission line (TL). Fabrication related issues are also discussed at the end of this section.

The modulation mechanism of the device proposed in this work involves the combination of two different kinds of NLO effects: E-field based Pockels effect and free carrier effect. Although the response time of the two respective effects are quite uniform within each domain (polymer slot for Pockels effect and silicon ridge for free carrier effect), the response time of the two effects is not found to be equal. In Fig. 3.7 (a), an NRZ voltage pulse (peak-to-peak voltage $V_{pp}=10$ V) is applied between the electrodes. The 10% to 90% rise and fall time of E_{bias} (at the center of the slot, i.e. $x=0$, $y=0.14$, in μm) are measured to be 2.5 and 2.8 ps respectively, which are slightly more than twice the rise/fall time for free carriers (taken at the same location of the DC study). The reason behind this is that the E-field and free carrier experience different transient capacitance and resistance when externally driven by the same voltage pulse. The slot and depletion layer capacitance per unit length can be formulated as follows for E-field and free carrier respectively

$$C_{slot} = \frac{\epsilon_{poly} h_{WG}}{W_{slot}} \quad 1/C_D = 1/C_{slot} + 1/C_{Dp} + 1/C_{Dn} = \frac{W_{slot}}{\epsilon_{poly} h_{WG}} + \frac{W_D}{\epsilon_{si} h_{WG}} \quad (3.10)$$

where W_D is the biased depletion width following the relationship [22]

$$W_D = W_{Dp} + W_{Dn} \quad W_{Dp,n} \approx \sqrt{\frac{\epsilon_{si}^2}{C_{slot}^2} + \frac{2\epsilon_{si}|V_{bias}|}{qN_{P,N}}} - \frac{\epsilon_{si}}{C_{slot}} \quad (3.11)$$

where $N_{P,N}$ is the dopant concentration of the P/N region. Eq. (3.11) is modified from the depletion region modeling of a biased metal-insulator-semiconductor (MIS) capacitor, where it can be calculated that the depletion width under zero bias is negligibly small due to the abrupt discontinuity of the work function between doped silicon and the polymer insulator (therefore, built-in potential is ~ 0). In Fig. 3.7 (b), a carrier level cutline is made across the center of the waveguide ($-0.365 < x < 0.365$, $y=0.14$, in μm) where optical intensity is at maximum to demonstrate the depletion width shift of the diode capacitor under bias.

It is confirmed that the depletion width at zero bias is only negligible and therefore the total carrier contrast between ON and OFF states can be approximated by the depletion width under reverse bias. Due to the same dopant level being used in both P and N regions, a symmetric depletion region is found where the depletion width at the P/N side (at -10 V) is around 120 nm and the total depletion width is comparable to the slot width. Therefore, for free carriers, the depletion layer capacitance C_D is noticeably reduced compared to C_{slot} for the E-field. Similarly, for free carriers, the silicon ridge resistance is also reduced to

$$R_{1p,n} = \rho_{p,n} \frac{W_{WG} - W_{Dp,n}}{h_{WG}} \quad (3.12)$$

The overall effect is a reduced time constant and hence improved device speed associated with the free carriers, which was previously limited by the E-field. According to the rise/fall time of the free carriers, the device 3-dB bandwidth is estimated to be at least 269 GHz using $f_{3dB} = 0.35 / \max(t_r, t_f)$ [78, 79], where the E-field ON/OFF contrast suffers by 34% from its maximum value according to Fig. 3.7 (a) and the resultant Δn_{eff} decreases from 1.65×10^{-4} to 1.4×10^{-4} by BPM calculation. Therefore, the device length associated with a π -phase shift ($L_\pi = \lambda / 2\Delta n_{eff}$) increases from 4.7 to 5.5 mm, which results in a phase modulation efficiency $V_\pi L_\pi = 5.5$ V-cm. The modulation efficiency shown here is comparable to

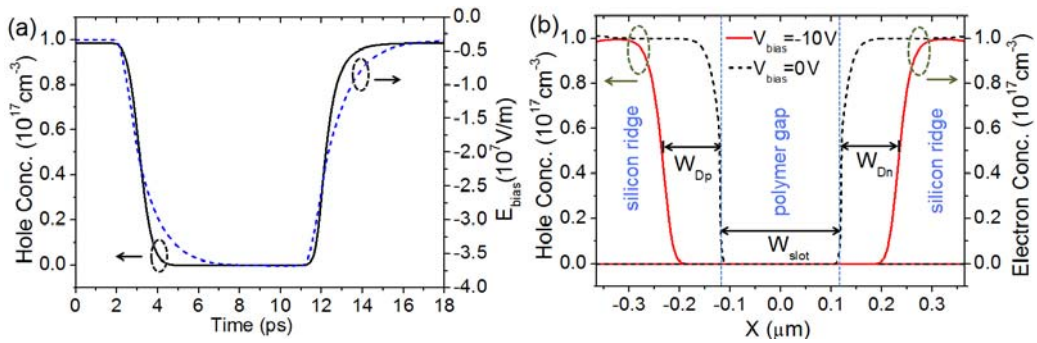


Figure 3.7 (a) Faster response is found for free carriers than E-field due to the reduced transient capacitance. (b) The carrier cutline along the x direction indicating the depletion width shift under reverse bias.

state-of-the-art polymer phase shifters while the speed potential of our device is almost 2 orders of magnitude higher [32]. It is important to point out that the abovementioned device figures of merit are highly conservative to illustrate the idea of a phase shifter working with multiple NLO effects. Therefore, only a modest Pockels coefficient is used here while recent progress in polymer science has demonstrated much higher nonlinear coefficients with high thermal stability: $r_{33} = 170$ pm/V in hybrid polymer/sol-gel [35] and $r_{33} = 300$ pm/V in self-assembled molecular glasses [80]. In either case, the modulation efficiency can be significantly improved without sacrificing the high speed demonstrated in the low aspect ratio slot waveguide design. The total propagation loss is calculated as 4.29 dB.

The performance of the phase shifter is then investigated both statically and dynamically when its active length is kept at 5.5 mm. First, a DC voltage scan is applied from 0 to -12 V to study the tradeoff relationship between phase shift and bias voltage. As shown in Fig. 3.8 (a), an almost linear dependence of the phase shift on the bias voltage is found at the two ends of the voltage scan where carrier depletion is either well below its turn-on threshold or reaches full capacity and the phase shift increases only with the increase of E_{bias} within the nonlinear slot according to Eq. (3.6). At the center part of the scan ($2 < |V_{bias}| < 10$), the phase shift increases nonlinearly due to the combined effort of E-field and free carrier contrast improvement. The S-shaped curve indicates the bias voltage can be further reduced at the expense of a larger device length to practically reduce the difficulty in designing the driver circuitry for sub-THz modulation.

Then dynamically, a NRZ signal with $V_{pp}=10$ V is numerically applied between the electrodes. The period and duty cycle of the signal are 2.4 ps and 46% respectively to match the rise/fall time of free carriers to maximize EO conversion efficiency, as shown in Fig. 3.8 (b). Although the NRZ signal with frequency up to ~ 400 GHz is still quite a challenge for state-of-the-art RF signal generators, the rectangular pulse has been a well-acknowledged way of numerically predicting dynamic device

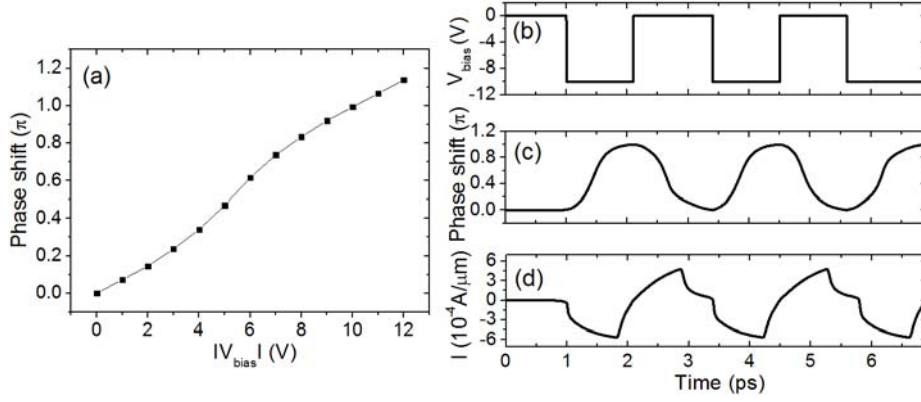


Figure 3.8 (a) The tradeoff relationship between bias voltage and phase shift. (b) The RF driving signal with $V_{pp}=10$ V and period of 2.4 ps. (c) The modulated phase shift in response to (b). (d) The transient current flow within the P-S-N diode capacitor in response to (b).

performance with speed up to 1 THz [34], and therefore serves as a reliable guidance to related experiments that will become routinely achievable in the near future. The resultant transient evolution of the phase shift is shown in Fig. 3.8 (c) where smooth transitions are found at the voltage transit points as carrier depletion approaches its saturated level with gradually reduced depletion rate, which agrees with previous study of a depletion mode phase shifter [18]. Although the diode capacitor experiences negligibly small DC leakage current and therefore consumes almost zero DC energy due to the insulating slot, noticeable AC current flow is found in capacitive characteristics as the RF energy flows back and forth between the electrodes. In Fig. 3.8 (d), sharp turning points of the AC current are found at each 0-1 voltage transit point as the free carriers are accelerated with soaring momentum upon the sudden potential drop between the electrodes. Since energy consumption only happens at 0-1 transitions where both current and voltage are non-zero, the averaged energy consumption per unit length is calculated as low as 1.06 fJ/ μ m·bit through Eq. (3.13) [26], while the total dynamic (AC) energy consumption of the device is 5.83 pJ/bit by multiplying by the device active length.

$$E_{bit} = 1/4 \int_{0-1} V_{bias} Idt \quad (3.13)$$

Generally, for EO active devices such as the phase shifter studied in this work, there are both electrical and optical waves propagating co-directionally through the device. Therefore, the transmission line needs to be properly designed to avoid undesired interference between them. The interference may come from the following five aspects. First, the aluminum electrodes can be a significant source of optical absorption for the guided mode. Here in this work, this potential metallic loss is avoided by keeping a large horizontal clearance between electrodes and waveguide (1 μm as shown in Tab. 3.1), where according to Fig. 3.2 (c), the optical intensity drops by more than 25 dB for TM-like polarization and 14 dB for TE-like polarization (similar results are found for the optimized geometry). Vertically, the electrodes are placed higher than the waveguide by an amount that equals waveguide height, where the total intensity drop can be even larger. Therefore, the spacing (horizontal and vertical) is safe enough to keep metallic loss negligibly small as also suggested in the previous studies of EO modulators based on a similar structure [31, 74].

Second, since the travelling-wave electrodes extend much longer in the propagation direction than in the transverse direction, the device speed can be further limited by the walk-off bandwidth that is determined by the group velocity difference between electrical and optical waves in the following relationship [37] (assuming π phase difference in the electrical and optical signal envelopes)

$$f_{walkoff,3dB} = \frac{0.5v_{g,opt}}{L_{\pi} \left| 1 - v_{g,opt} / v_{g,elec} \right|} \quad (3.14)$$

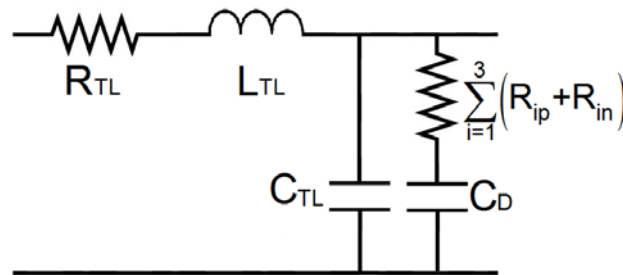


Figure 3.9 Equivalent circuit of the TL loaded with the P-S-N diode capacitor.

where $v_{g,opt}$ and $v_{g,elec}$ are the group velocity of optical and electrical waves respectively. Therefore, to maximize walk-off bandwidth, the group index of the microwave TL needs to be designed to equate that of the SWG to satisfy the so-called phase matching condition, where the device bandwidth is mostly limited by the intrinsic RC time constant of the SWG, $C_D \sum_{i=1}^3 (R_{ip} + R_{in})$.

The equivalent circuit for the infinitesimal TL segments can be simplified and shown in Fig. 3.9, where R_{TL} , C_{TL} , and L_{TL} are the resistance, capacitance, and inductance of the unloaded TL respectively [74]. From Fig. 4.12, the effective index of the TL can therefore be calculated as

$$n_{TL,eff} = c_0 \sqrt{C_{TL} L_{TL} + C_D L_{TL} \frac{1}{1 + i \frac{f}{BW}}} \quad (3.15)$$

where c_0 is the speed of light in vacuum; f and BW are the operating frequency and intrinsic bandwidth of the SWG ($1/2\pi C_D \sum_{i=1}^3 (R_{ip} + R_{in})$) respectively. For the TL loaded with the P-S-N diode capacitor, the RF signal can be significantly slowed down due to the large depletion capacitance C_D and TL self-inductance L_{TL} so that $n_{TL,eff}$ can be much larger than the effective index of the waveguide ($n_{eff} = 2.02$ for the optimized waveguide geometry). In this work, $n_{TL,eff}$ is lowered by first employing the low aspect ratio slot waveguide design to reduce the depletion layer capacitance C_D and operating the device at a much higher speed (higher RF frequency). Then, the width and height of the electrodes are increased to 50 and 10 μm respectively to reduce the L_{TL} so that the total $n_{TL,eff}$ can be reduced to match n_{eff} according to the extrapolated finite element calculation performed in ref. [74].

Experimentally, RI difference has been reported for nonlinear polymers before and after poling, and several methods have been proposed to measure the exact index of polled polymers [81-83]. Therefore, even for the optimized TL design ($v_{g,opt} = v_{g,elec}$), the walk-off bandwidth may be reduced due to the $v_{g,opt}$ change from the polymer index shift after poling effect, denoted Δn_{poling} . Based on previous studies, here a probable index variation range from -0.1 to 0.1 is studied while the exact amount of index change is highly dependent on the combination of the polling field, time, and temperature, and therefore yet to be measured in the real experiment. The effective index change of the guided mode is calculated accordingly by the BPM simulator to further calculate the walk-off bandwidth using Eq. (3.14) and $v_{g,opt} = C/n_g \approx C/n_{eff}$ in a low dispersion environment. As shown in Fig. 3.10, the walk-off bandwidth at both ON and OFF states overlaps with each other and reduces to 20 and 13 THz when Δn_{poling} goes up to -0.1 and 0.1 respectively, which is at least 48 times larger than the operation speed of the device. Therefore, the device speed is still primarily governed by the RC effect of the RF circuitry and highly tolerant to polymer index shift after the polling effect.

Third, the characteristic impedance for the loaded TL can be formulated in Eq. (3.16) using the equivalent circuit given in Fig. 3.9.

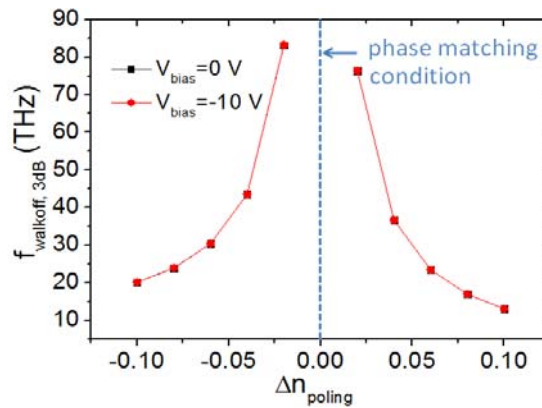


Figure 3.10 The walk-off bandwidth (ON and OFF states) reduces with the increase of the polymer index shift from polling effect.

$$Z_c = \frac{1}{2} \sqrt{\frac{1}{\frac{C_{TL}}{L_{TL}} + \frac{C_D}{L_{TL} \left(1 + i \frac{f}{BW}\right)}}}} \quad (3.16)$$

For the slot waveguide with optimized TL design (phase matching condition satisfied), the TL impedance Z_c increases almost linearly with the slot width [74]. As a result, for the optimized waveguide geometry ($W_{slot} = 240$ nm), the Z_c is estimated to be around 42 Ω (extrapolated from the finite element solver for Eq. (3.16)). Therefore, the optimized phase shifter can be connected to a 42 Ω RF terminator (or a more commonly available 50 Ω one) in order to minimize the RF rejection (reflection) resulted from the possible impedance mismatch.

Fourth, the parasitic coupling effect is also one of the practical factors that will perturb device performance at high operation speed. To be more specific, the effect may come in two folds. First, the parasitic capacitance/resistance between the two electrodes will become more prominent at RF operation speed [13, 84, 85]. In addition to the waveguide slab and slot capacitances/resistances that have already been included in the electrical modeling part of the study, the parasitic components of the RC equivalent circuit are highly dependent the electrode geometry and configuration and may further increase the time constant and lower the dynamic response of the device. Second, higher order parasitic modes may exist in the substrate and cause signal distortion through microwave coupling with the traveling coplanar waveguide (CPW) modes. This is more commonly the case in LiNbO₃ based broadband devices, where the relatively high permittivity results in the generation of higher order parasitic modes at lower frequencies than the modulation bandwidth [86]. As a more precise way of device modeling, especially in the electrical part of the work, the commercial package of HFSS could be used in designing the traveling wave electrodes with minimized parasitic capacitances and resistances.

Last but not least, For the polymer infiltrated P-S-N diode capacitor based modulator, transmission line loss of the traveling electrodes is another common phenomenon associated with the resistivity and capacitivity of silicon at radio frequency operation domain [13, 45, 74]. More specifically,

the excess transmission losses induced in the resistive silicon can be modeled as the power dissipated by the series resistance of the waveguide. According to the RF equivalent circuit (Fig. 3.9 in the revised thesis), the transmission line loss (absorption coefficient in dB/length) can be formulated as [74]

$$\alpha = \frac{10}{\log(10)} \frac{\omega^2 C_D^2 \sum_{i=1}^3 (R_{ip} + R_{in})}{1 + \left(\frac{f}{BW}\right)^2} \quad (3.17)$$

where C_D and $\sum_{i=1}^3 (R_{ip} + R_{in})$ are the depletion capacitance and series silicon resistance respectively, while f and BW are the operation frequency and intrinsic bandwidth of the slot waveguide respectively. While the estimated RF loss is around 80 dB/cm at the operation speed of 260 GHz by extrapolating the HFSS calculated results given in [7], a more detailed RF attenuation study can be performed when the RF computation resource is available.

Finally, device fabrication, although not carried out here, can be completely based on well-developed CMOS compatible processing techniques. The fabrication starts with an SOI wafer where the dopant regions can first be patterned and defined by deep ultraviolet (DUV) lithography and ion implantation (followed by RTA). Then, the SWG is defined by reactive ion etching (RIE) where the thin silicon slab can be maintained by controlling the etching rate and time of the process. Another RIE process is needed after that to open a complete slot to the silicon/insulator interface. Then, the aluminum contacts can be deposited by e-beam evaporation followed by annealing to enhance conductivity. After that, the device is spin-coated with EO polymer and the polymer needs to be cleared from the contact pad by laser ablation [42]. As a final step, the polymer is poled by applying a certain combination of poling field, time, and temperature.

In short, in this section, a polymer-infiltrated P-S-N diode capacitor structure has been studied for high speed EO phase shifters. The structure explores a way of constructing a low cost high speed modulation component where the RC limitation is effectively alleviated in a group of low aspect ratio slot

waveguides. By incorporating multiple nonlinear effects within the waveguide cross section, the numerical results show a much higher 3-dB bandwidth of 269 GHz modulation is achievable at the high efficiency of 5.5 V-cm for the optimized waveguide geometry. The encouraging device performance relies on the high EO overlap within the major portion of the waveguide cross section rather than the strong optical confinement of the nano-slot which formed the basis for previous studies. Therefore, the fabrication tolerance for nano-patterning, etching, and infiltration has been significantly relieved. Additionally, the device consumes almost zero DC energy and ultra-low AC energy and hence is suitable for green photonics related applications.

3.4. Performance conclusion and comparison

In this section, a summarized performance of the polymer phase shifter is given in comparison with other key polymer based EO/all optical modulators that have been proposed and studied in literature. As we can see in Tab. 3.2, the 3-dB bandwidth of the polymer phase shifter is 269 GHz and therefore a significant improvement from the previously studied devices based on a similar configuration. This is because of the low aspect ratio waveguide geometry used to alleviate RC limitation. The peak-to-peak voltage of the driving signal is 10 V. In Tab. 3.2, all the devices can be categorized into MZI and photonic resonator based approaches, where a significantly reduced device length is found in the latter. In order to realize optical modulation, both Pockels and Kerr nonlinearities have been studied for EO and all optical operations. The difference in the nonlinear mechanism resulted from the different kinds of polymers incorporated into the silicon hybrid platform. It is shown that, in the long run, all optical polymers with strong Kerr nonlinearity are especially promising for high speed modulation purposes where the device speed is not longer limited by the RC time constant of the small signal equivalent circuitry of the phase shifter cross section. However, the average power of the optical pump is still kept much higher than the electrical driving signal in the EO modulator cases (Pockels effect). As far as our device is concerned,

two different kinds of nonlinearities (free carrier and Pockels effects) are incorporated into a single device cross section, so that the resultant device speed can be enhanced by lowering the geometric aspect ratio of the conventional slot waveguide without sacrificing EO overlapped volume. The device speed predicted is even much higher than the all optical polymer based modulators. And the device length is also considered as relatively small for MZI based devices.

Table 3.2 Detailed device performance comparison between the device studied in Section 3.3 and previous works in literature.

Year	Author	EO structure	Nonlinear Mechanism	Speed (GHz)	DC Power (mW)	AC Energy (fJ/bit)	Length (μm)
2006	Hochberg [34]*	Polymer/Slot MZI	Kerr effect	1000	30 (optical pump)	N/A	10000
2007	Bortnik [87]*	Polymer/RR	Pockels effect	165	N/A	N/A	122
2008	Brosi [37]	Polymer/PC embedded MZI	Pockels effect	78	~0	N/A	80
2009	Wulbern [40]	Polymer/PC resonator	Pockels effect	100	~0	N/A	~30
2009	Koos [38]*	Polymer/Slot WG	Kerr effect	170	48 (optical pump)	N/A	4000
2010	Ding [32]*	Polymer/Slot MZI	Pockels effect	3	~0	N/A	1000
2011	Gould [42]*	Polymer/Slot RR	Pockels effect	1	~0	N/A	80
2011	Xin	Polymer/PSN diode capacitor	Pockels effect & Depletion	269	~0	5830	5500

* Fabricated device

CHAPTER

4. DEVICE FABRICATION AND EXPERIMENTAL CHARACTERIZATION

4.1. Introduction

Previously in Section 2.4, a hybrid lattice resonator based EO modulator was studied. Here in this chapter, the fabrication process and experimental characterization of that device will be discussed. Out of the four device structures described in previous sections, this device was selected for fabrication because of its optimized optical confinement, EO sensitivity, and carrier movement route for high speed and efficiency modulation. At the same time, unlike the polymer based approach, the device process is completely CMOS compatible and therefore well established with acceptable fabrication errors. At the time of device fabrication, the design of the depletion mode based dopant profile was still in progress. As a result, the fabricated device is targeted for injection mode operation via an embedded P-I-N diode configuration, and the optical configuration of the device is based on the optimized hybrid-lattice resonator structure discussed in Section 2.4.1. The schematics of the fabricated device are shown in Fig. 4.1 (a) and (b). One of the main goals presented in this chapter is to confirm and verify the numerical design and theoretical analysis carried out in the previous sections. For brevity, the detailed numerical results for the injection mode modulator are not shown here in this chapter and one may refer to the conference proceeding (Proc. SPIE **7943**, 794318, 2011) listed in Appendix B for details. Therefore, the rest of the chapter is organized as follows. In Section 4.2, the device fabrication is first introduced, which includes detailed discussions on preliminary designs of electrodes and doping recipe, as well as process flow. Then, in Sections 4.3 and 4.4, the optical and electrical characterizations are covered respectively,

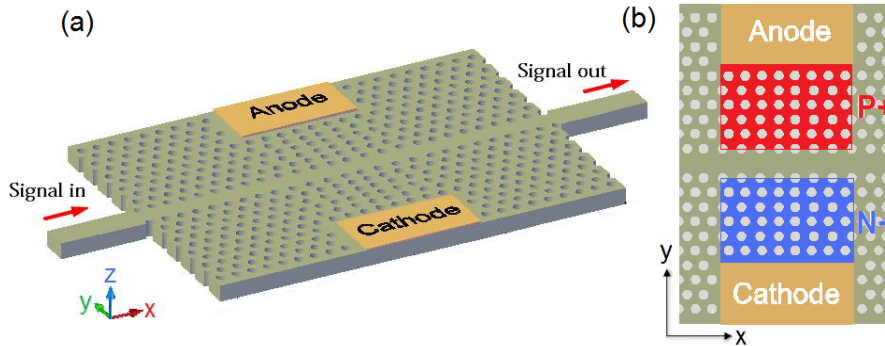


Figure 4.1 Schematics of the device fabricated in Chapter 4. (a) 3D schematic of the whole device; (b) 2D schematic of the device showing dopant profile for injection mode operation.

where both measurement set up and results are included in comparison with theoretical study results.

Finally, a summary of the chapter is given in Section 4.5.

4.2. Device fabrication

In this section, the device fabrication process is introduced. The whole fabrication process was carried out using the standard CMOS compatible processing facilities and techniques in the collaboration institute (IME). Due to the limited access to the facilities and information that the institute chose to disclose, the process parameters are described throughout the chapter with as much detail as possible according to the best of our knowledge and experience. Since the detailed process recipe still varies from equipment to equipment, we think the description below is accurate enough for readers from a broad area of interest to have a technically informative insight into the process of an EO modulator such as the one designed in the previous chapters of the work. First, in Section 4.2.1, the preliminary design of high speed electrodes for signal generator and RF terminator is discussed. Then, the doping recipe for both P⁺ and N⁺ regions are developed using the ATHENA process simulator. After that, a detailed description of the process flow is given in Section 4.2.2. Finally, the completed device is shown and described in Section 4.2.3.

4.2.1. Preliminary design

Before going through the actual fabrication steps, there are preliminary design steps involved to bridge the gap between numerical design and device fabrication. These design steps cover high speed contact pads, device spacing, alignment marks, chip layout, and dopant recipe. The design tool used is the L-Edit module from Tanner EDA Software Tools [88], which is an efficient tool for multi-layer hierarchy

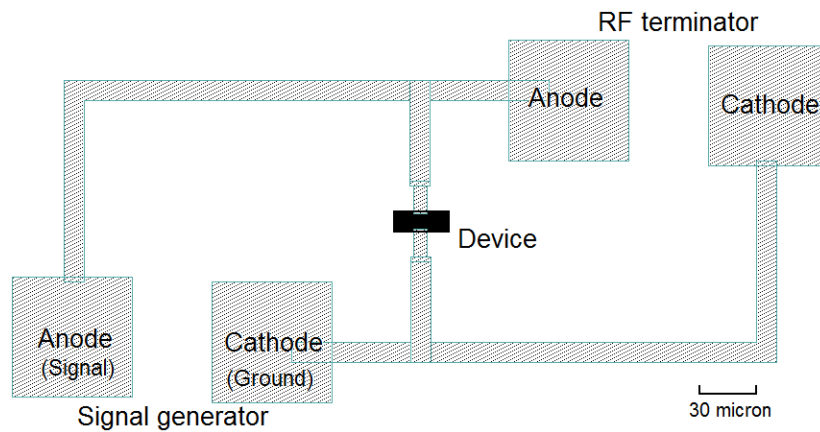


Figure 4.2 Aluminum contact pad schematic as it appears in L-Edit design module.

design. Each layer is then an independent mask layout that is compatible for mask fabrication. In this work, the passive hybrid lattice resonator schematic and dopant window are first setup in two separate layers in L-Edit gds file. The detailed design parameters for these two layers have already been discussed in Section 3.4.2 and are not repeated here. The high speed aluminum contact pad design is first discussed and the L-Edit schematic is shown in Fig. 4.2.

As one can tell from Fig. 4.2, two pairs of electrodes are made: one for signal generator connection and the other reserved for RF terminator connection. The RF terminator is in parallel connection to the device and is of critical importance to achieve impedance matching for high speed modulation demonstration. The spacing between the electrodes is designed to be 100 μm to match the pitch size of ground-signal-ground RF probes. The size of the electrode is designed to be $100 \times 100 \mu\text{m}^2$ for probing and testing purposes.

A total number of 13 devices (including one reference waveguide) are put in parallel with each other on a single chip. The device spacing is kept at 220 μm to eliminate potential interference between two neighboring devices. In Fig. 4.3 (a), the magnified schematic of a single hybrid-lattice resonator based modulator is shown which includes multiple layers for device core area, dopant window, extended electrodes, electrode platform, and coupling waveguide. In Fig. 4.3 (b), the whole set of devices with various design dimensions is shown, where “S” shaped waveguide bends are designed to introduce a

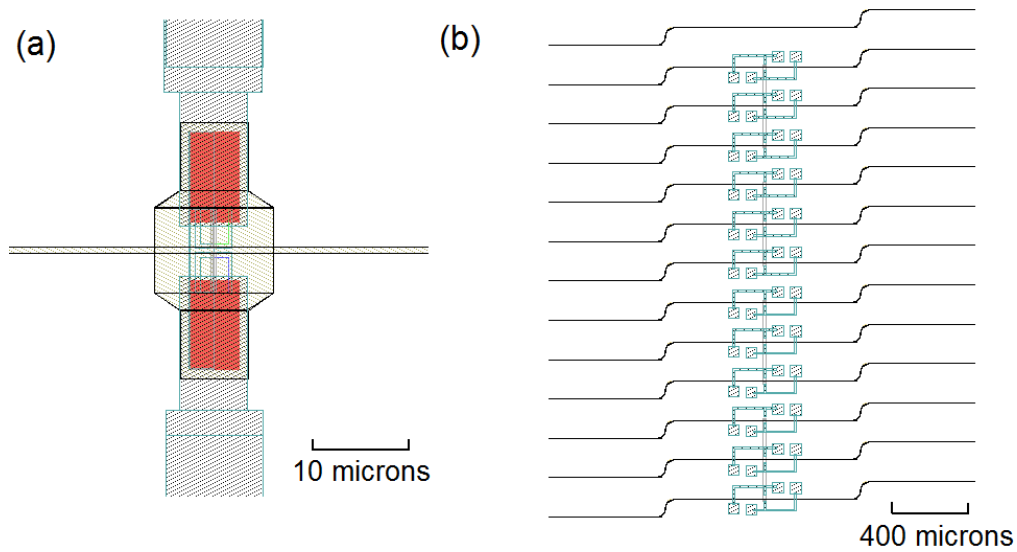


Figure 4.3 Completed device layout design using L-Edit: (a) the magnified schematic of a single device that is defined in a multi-layer hierarchy; (b) the view of the whole set of devices with different dimensions for chip layout.

mismatch between input and output waveguides so that the two optical waves will not interfere with each other.

The other side of the preliminary design is for ion implantation and RTA recipe. It is worth mentioning that the designed dopant profile is for a P-I-N diode based carrier injection mode operation, and therefore is different from the one discussed in Section 2.4.1. (The depletion mode design is still in progress at this time). The target dopant concentration for the P⁺/N⁺ region is $2 \times 10^{19} \text{ cm}^{-3}$ and in the implantation step, a two-step approach is used to introduce more flexibility and accuracy in the final profile. The 2D process simulator from SILVACO ATHENA [89] is used to model the fabrication

processes. The purpose of the simulation is to predict the resultant geometric and/or dopant imperfections in the device structures, based on which, highly accurate process recipes such as ion implantation and RTA can be developed for real experimental characterization.

First of all, ion implantation is the main method used to introduce high level dopant impurities into semiconductor device structures at low temperature. The resultant 2D dopant ion profile in both longitudinal and transverse directions is usually determined by a combination of spatial ion beam angle, dose, and energy. The profile is also dependent on the ion type because different ions have different effective masses which results in different ion momentum and implantation trajectories even for the same dose and energy levels. Here in this work, the SIMS-Verified Dual Pearson (SVDP) model is used. The model uses tables that contain dual Pearson moments for boron (B), difluoroborane (BF₂), phosphorus (P) and arsenic (As) ions extracted from high quality implantation experiments conducted by the University of Texas at Austin. The Pearson model uses the Pearson IV function to predict implantation profile in the longitudinal direction, which is generally preferred over the Gaussian distribution because real profiles are asymmetrical in most cases.

To activate the implanted ions and anneal out the damage to the substrate, rapid thermal annealing is usually conducted soon after the implantation process. As a side effect, the RTA process also reshapes dopant profile noticeably through the carrier diffusion process due to the carrier concentration gradient throughout the doped region. Therefore, accurate modeling of the RTA process is also essential to the whole ion implantation process. In order to heal the substrate damage and interstitials while minimizing carrier diffusion by the process, usually high temperature and short annealing time are used.

In this work, the fully coupled diffusion model is used for the thermal diffusion process. The model relies on the concept of pair diffusion, which means that a dopant atom cannot diffuse on its own and it needs the assistance of a point defect (a silicon self interstitial or a lattice vacancy) in the near vicinity as a diffusion vehicle. Therefore, the dopant diffusivity within the scope of the model actually means the diffusivity of the pair as a whole. As a result, a two-way interaction between the diffusion of

dopants and the diffusion of point defects is used in the calculation, which takes into account most of the major physical effects involved in the thermal diffusion process.

After optimization of the major process parameters involved, the ion implantation and RTA recipes for the optimized dopant profile are shown in Tab. 4.1. The resultant dopant profile in the longitudinal direction is shown in Fig. 4.4 (a) and (b) for the P⁺ and N⁺ regions respectively, where the dopant profile extends almost uniformly into the device depth and the dopant level is highly close to the designed value.

Table 4.1 Dopant recipe for the injection mode hybrid-lattice resonator based modulator that is fabricated in Chapter 4: (a) P⁺ region; (b) N⁺ region.

(a)

P ⁺ region definition	Dose (10 ¹⁵ cm ⁻²)	Energy (KeV)	Temperature (degree C)	Time (mins)
Step 1 (implantation)	0.25 (boron)	15	N/A	N/A
Step 2 (implantation)	0.45 (boron)	60	N/A	N/A
Step 3 (RTA)	N/A	N/A	1030	2

(b)

N ⁺ region definition	Dose (10 ¹⁵ cm ⁻²)	Energy (KeV)	Temperature (degree C)	Time (mins)
Step 1 (implantation)	0.2 (boron)	45	N/A	N/A
Step 2 (implantation)	0.3 (boron)	140	N/A	N/A
Step 3 (RTA)	N/A	N/A	1030	2

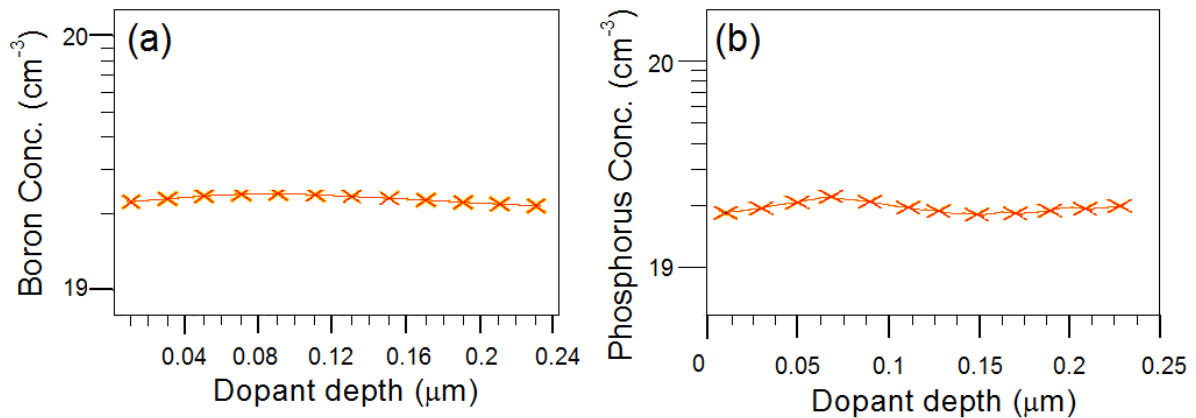


Figure 4.4 The dopant profile in the longitudinal direction after ion implantation and RTA calculation from ATHENA.

4.2.2. Process flow and technical background

The major steps of the device process flow are listed below in Fig. 4.5 (simplified and not plotted in exact scale to the real device dimensions). The process starts with a SOI wafer from Soitec with crystal orientation at $\langle 100 \rangle$ direction and buried oxide layer thickness of 3 μm . The top silicon layer thickness is 220 nm and matches the silicon photonic crystal slab thickness of the design. To begin with, the alignment marks are patterned and etched for precise alignment between multiple etching, ion implantation, and metal deposition steps. Each step has a different mask that corresponds to each independent layer in the L-Edit gds file. Therefore, the alignment masks need to be etched deep enough (usually at least 1 μm into the substrate) so that they will not be worn out after multiple steps of device processing. Then, the background P/N type doping is performed by ion implantation with targeted dopant concentration at 10^{15} cm^{-3} . After that, the N^+/P^+ dopant area is first patterned and then the implantation is done, followed by an RTA process according to the recipe given in Tab. 4.1 (a) and (b). The resultant device cross section is shown in the simplified schematic of Fig. 4.5 (b).

Then, the hybrid-lattice resonator structure is first patterned by DUV lithography to resolve the finest feature size of 246 nm (hole diameter). As we know, the smallest resolution of photolithography technique is determined by the diffraction limit $\lambda_s/2$, where λ_s is the operation wavelength of the light source. Therefore, compared to conventional photolithography technique that uses UV light to transfer pattern from mask to wafer, DUV lithography usually works with 193 nm and 248 nm exposure wavelengths and therefore, is able to resolve more detailed feature sizes down to 90 nm. Similar to conventional photolithography processes, the major steps of DUV lithography can be listed as follows:

- a. Surface preparation*
- b. Coating (spin casting)*
- c. Pre-bake (soft bake)*
- d. Alignment*
- e. Exposure*
- f. Development*
- g. Post-bake (hard bake)*
- h. Processing using the photoresist as a masking film*
- i. Stripping*
- j. Post Processing Cleaning (Ashing)*

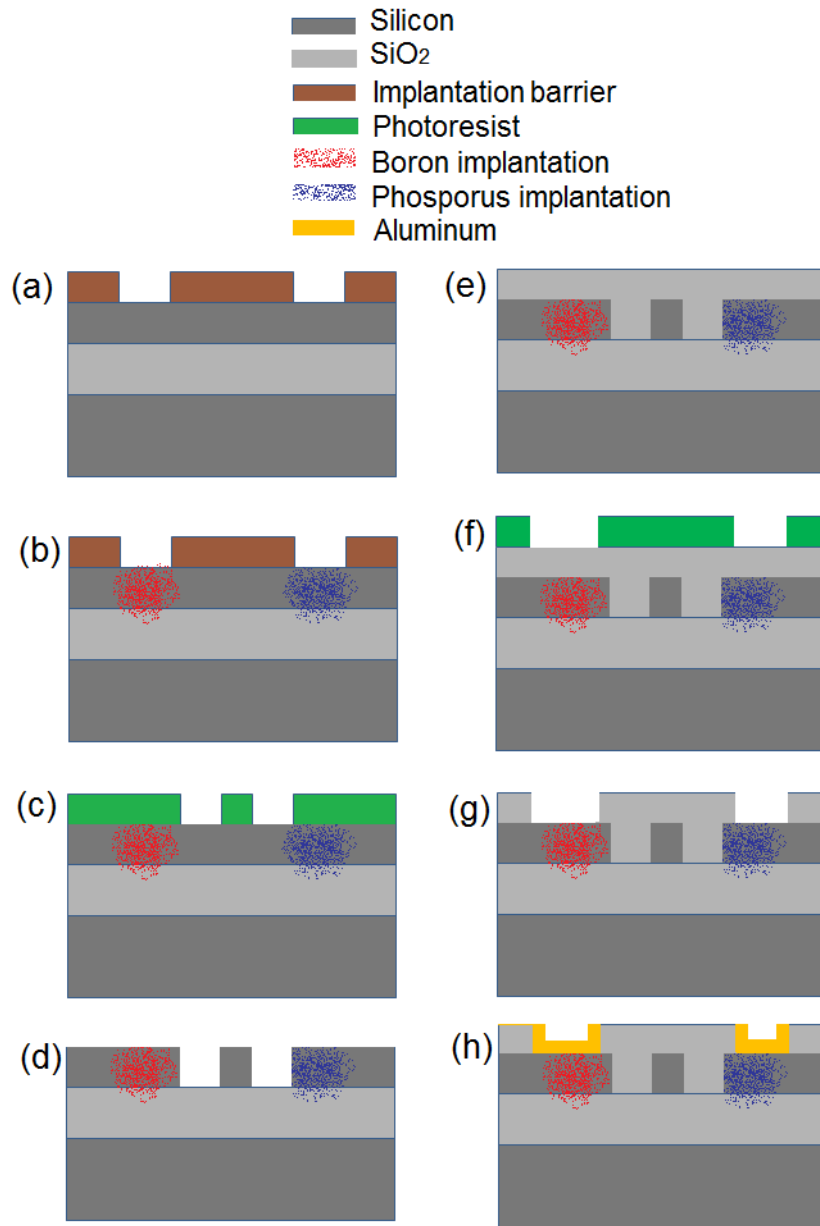


Figure 4.5 Process flow of the hybrid lattice resonator based modulator. (a) DUV patterning of implantation barrier; (b) boron and phosphorus ion implantation; (c) DUV patterning of waveguide and photonic cavity; (d) RIE etching of waveguide and photonic cavity; (e) PECVD process for top SiO₂ cladding; (f) contact hole patterning; (g) contact hole RIE etching; (h) EBE process for aluminum deposition.

Then, the waveguide and the hybrid-resonator are etched with the RIE method. The dry etching method uses a chemically reactive plasma to remove the unprotected top layer silicon. Here, sulfur

hexafluoride (SF_6) is used as the major etching gas and the gap flow rate, power, and chamber pressure are optimized towards a relatively slow etching rate for the fine features in the device. After the process, the cross section of the device appears to be Fig. 4.5 (d).

After that, a 2 μm SiO_2 cladding layer is deposited over the surface of the etched photonic cavity and waveguide, which is especially important for passivating the silicon EO active devices for protection and isolation purposes. This step is performed by plasma-enhanced chemical vapour deposition (PECVD). After the SiO_2 deposition, the resultant device cross section is shown in Fig. 4.5 (e).

Then, the contact holes are patterned and etched using the process discussed above. After that, the aluminum electrodes are deposited and the basic requirement for metallization is that it has high conductance to reduce voltage drops on the lines, and minimal capacitance between the lines so as to reduce delay time, which is a significant factor for high speed modulation. Aluminium adheres well to both silicon and silicon dioxide, can be easily vacuum deposited (since it has a low boiling point), and has high conductivity. Therefore, Al is favored in this work and this step is performed by electron beam evaporation (EBE), which falls into a general category of physical vapor deposition (PVD). After the EBE process, the top cladding aluminum layer is removed using another RIE etching process. The cross sectional schematic of the device after this process is shown in Fig. 4.5 (h).

Finally, the metal pad is patterned and etched according to the electrode design discussed in the previous subsection and the coupler deep trench is then patterned and etched after that. As a final step, the wafer is diced into rectangular chips for measurement purposes.

4.2.3. Completed device

The completed device SEM image is shown in Fig. 4.6 (a), where gold sputter coating of the device was first performed before taking the image to improve image quality due to the top insulator

cladding. In Fig. 4.6 (a), one can clearly see the input and output coupling waveguides connected to the hybrid-lattice resonator although the whole device is clad with SiO₂. The electrodes, anode and cathode, are configured perpendicular to the waveguide direction for driving the signal externally. The majority of

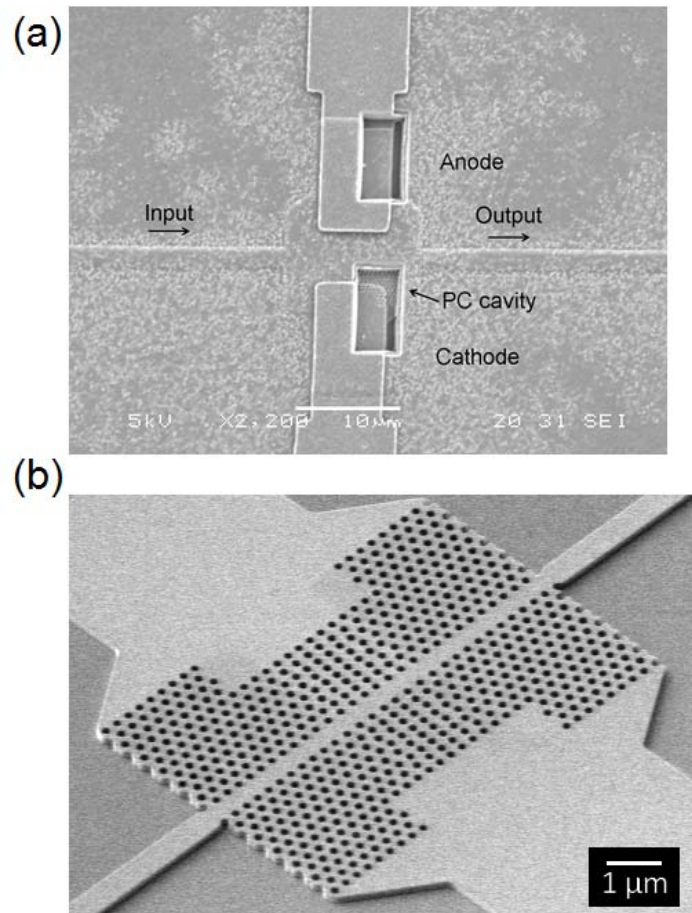


Figure 4.6 (a) SEM image of the completed device (after SiO₂ cladding) showing the light path through the photonic crystal resonator and electrical driving contacts; (b) SEM image of the passive hybrid-lattice resonator and coupling waveguides.

the PC cavity is buried under the top 2 μm cladding layer while a small part of cavity is exposed to make the contact holes where part of the PC lattice of holes can be seen clearly from beneath.

In Fig. 4.6 (b), the passive hybrid-lattice resonator structure is shown where a gradual transition of the hexagonal lattice into the central rectangular one is found. Several periods of the lattice holes are missing to enable an extended electrode on the two sides of the device so that the operation speed can be

improved. Since according to the numerical results shown in Section 2.4.1, the optical mode intensity is mostly confined within three periods of the lattice in the electrode direction, the additional optical absorption due to the extended electrodes is kept at minimum.

4.3. Optical characterization

To enable efficient optical coupling from light source to the waveguide, an inverse taper is designed at the end of the coupling waveguide and tapered (lensed) fiber is designed to match the dimension of the inverse taper, Fig. 4.7 (a). As a result, the total coupling loss can be kept lower than 1 dB when the fiber and the waveguide are perfectly aligned both within the transverse plane and in the vertical direction. The in-plane alignment is achieved by a high magnification optical microscope, where the device top view image shows the clear edge of the coupling waveguides at both input and output side of the device, shown in Fig. 4.7 (b). The vertical alignment is guaranteed by using an infrared camera, where the guided mode intensity can be captured to make sure perfect guiding of the mode inside the waveguide by inspecting the diffraction pattern of the guided mode.

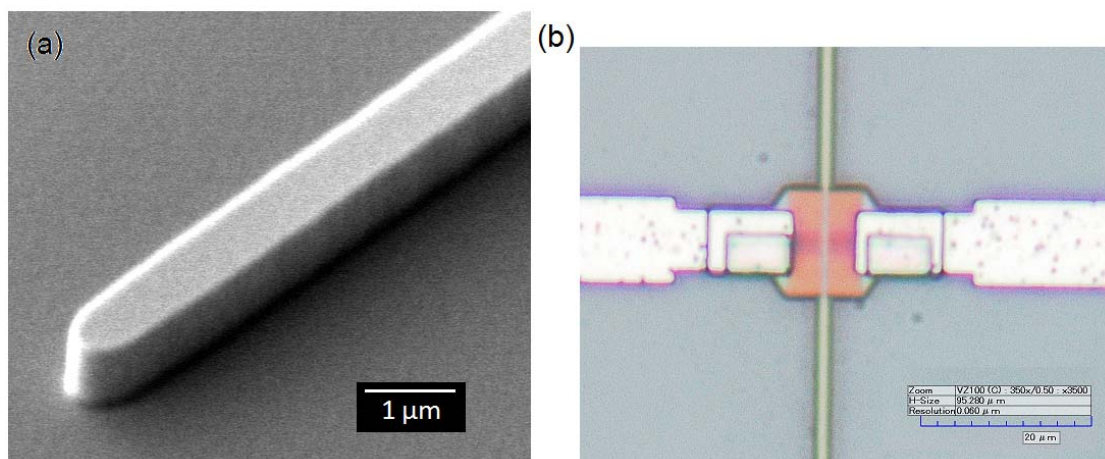


Figure 4.7 (a) SEM image of the inverse tap at the end of the coupling waveguide; (b) device top view under high magnification optical microscope for waveguide alignment purposes.

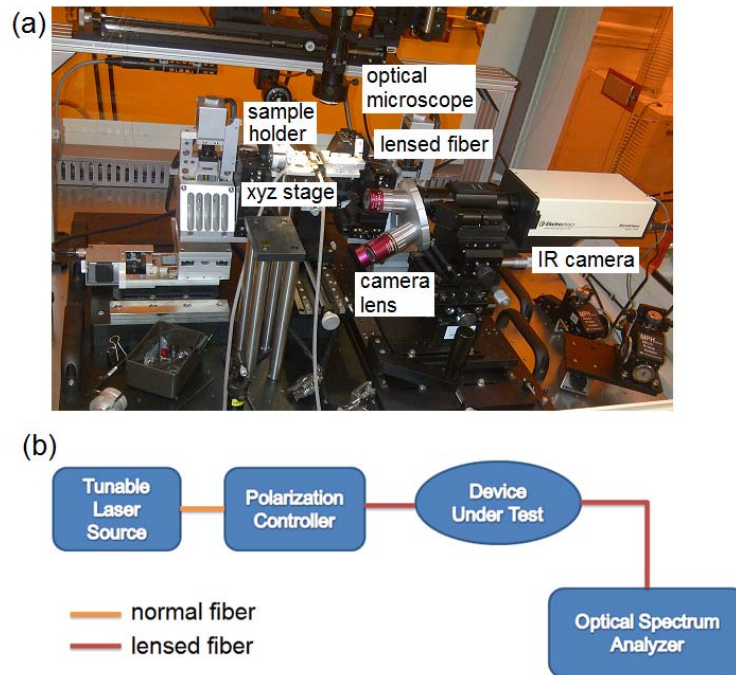


Figure 4.8 (a) Image of the passive nanophotonics measurement setup; (b) Schematic of the optical connection for transmission measurement.

Then, the passive transmission of the device is measured. The image and connection schematic of the measurement setup are first shown in Fig. 4.8 (a) and (b), where the resonance behavior of the cavity is experimentally demonstrated by a high resolution tunable laser source (TLS) and an optical spectrum analyzer (OSA). The scanning wavelength range is from 1540 to 1640 nm in steps of 0.1 nm. The measured transmission spectrum is shown in Fig. 4.9 (a) and (b). In Fig. 4.9 (a), the transmission is plotted in a logarithmic scale and one can tell that the transmitted intensity is almost stable in the frequency domain for the reference waveguide, which is reasonable since the homogenous rib waveguide proves to be a broadband device. However, for the hybrid-lattice resonator based modulator with different defect lattice periods, periodic transmission dips are found beyond the wavelength around 1580 nm, where the peak transmission is also noticeably lower than that below the wavelength of 1580 nm. Therefore, it is confirmed that the PBG based slow light phenomenon is detected between the wavelengths of 1580 to 1640 nm, which almost matches the numerical design results described in Section

2.4.2. Then, the same transmission spectrum is plotted in a linear scale in Fig. 4.9 (b), where multiple resonance peaks are identified within the PBG range. Hereafter, it is confirmed that the hybrid-lattice resonator part of the EO modulator is working properly according to the design. After that, the spectrum is taken out that corresponds to the defect period of 400 nm to investigate the full resonance peaks around the designed value. The closest resonance peak according to the design is plotted in Fig. 4.10, where the resonance wavelength and FWHM pulse width is measured as 1601 and 0.25 nm respectively. The corresponding Q factor is therefore calculated to be around 7800 using the definition: $Q = f_c / f_{FWHM}$, where f_c is the resonance frequency and f_{FWHM} is the full width half maximum linewidth of the resonance peak. Both of the figures are calculated from Fig. 4.10. It is here to point out that since the spectral resolution of the cavity transmission is limited to the minimum tunable step of the tunable laser source (TLS), which is 0.1 nm while the FWHM of the resonance peak is ~0.2 nm, there will be a non-negligible error range for the characterized Q factor. In worst case scenario, the measured FWHM will be in the range from $FWHM_{real}-0.1$ to $FWHM_{real}+0.1$, where $FWHM_{real}$ is the real FWHM pulse width without measurement error. Therefore, the uncertainty of the measured Q factor is from 5336 to 16010. To get a more precise characterization of the high Q cavity, a finer step TLS is recommended. For example, a piezo actuator can be used to control the TLS source with precise wavelength tuning on the order of picometer (pm) [58]. Also shown in ref [58], as an alternative to frequency domain measurement, time domain light emission can be investigated to determine energy decay and photon lifetime. In this way, a precise measurement can be performed to characterize one million-Q factor cavities.

As much as we have tried, due to the collaboration issues of the project between institutions, the active and dynamic characterization of the device was not available to be included into the scope of this work although it would make the work more complete as the candidate wishes.

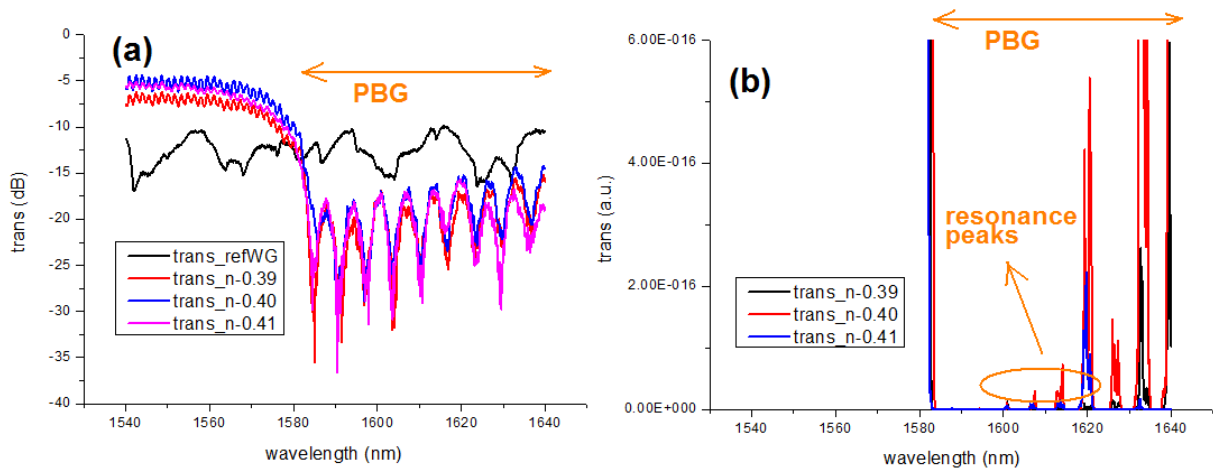


Figure 4.9 (a) The full spectrum of the device from 1540 to 1640 nm in dB. The photonic bandgap and slow light phenomenon are apparent from the low transmission and periodic resonances from 1580 to 1640 nm, which matches the numerical results; **(b)** the transmission is plotted in linear scale and resonance peaks are detected in the PBG.

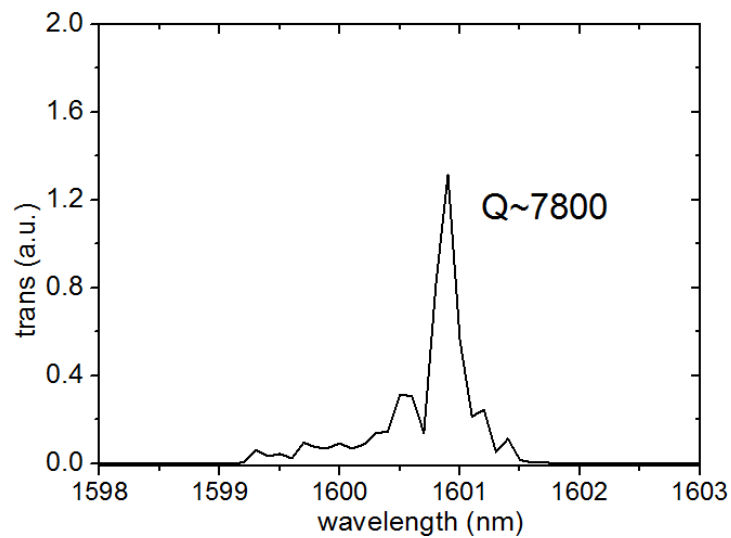


Figure 4.10 Measured transmission spectrum of the hybrid lattice resonator based modulator (defect lattice period 400 nm) indicates a highly confined resonance mode in the near infrared range with a Q factor around 7800.

4.4. Electrical characterization

The electrical I-V characteristics of the modulator are measured by an electrical probe station (Fig. 4.11 (a)) and semiconductor parameter analyzer (Fig. 4.11 (b), HP 4156 A). The I-V response of the device is mainly determined by the embedded P-I-N junction diode which is operated in the forward bias (injection) mode. Therefore, the electrical characteristic of the device should bear fundamental features and trends that are common among classic P-I-N diodes while the absolute value of the I-V curve will be further affected by the embedded holes that form the hybrid-lattice resonator.

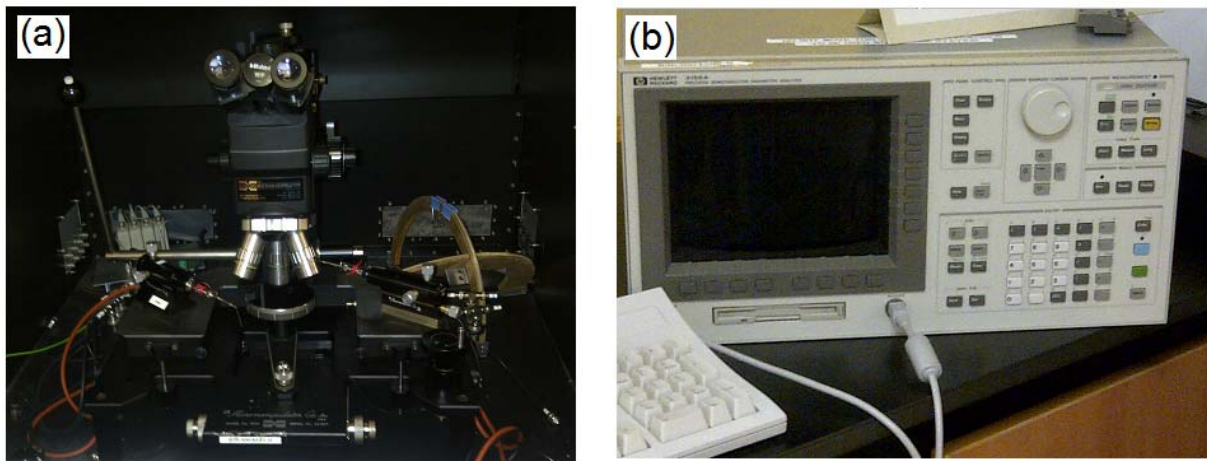


Figure 4.11 (a) Image of the probe station for I-V measurement; (b) image of the HP 4156A semiconductor parameter analyzer.

The measured I-V characteristics of devices with different design parameters are shown in Fig. 4.12 (a) and (b). First, the defect period is kept at 400 nm in Fig. 4.12 (a). One can tell that for the lower doping offset where the intrinsic region of the P-I-N diode is smaller as the P⁺ and N⁺ regions are put closer to each other, the injection current is higher for the same bias voltage. The turn-on voltage of the diodes with either 0.71 or 0.355 μm doping offset is measured around 1 V, and the trend of the I-V characteristic matches what is expected from P-I-N junction diodes. In Fig. 4.12 (b), the I-V characteristic of devices with different defect lattice periods from 390 nm to 410 nm is compared when the doping offset is fixed at 0.71 μm . The results indicate that for larger defect period, higher injection current is

found for the same bias voltage. This is because that when the defect period is larger, the inner most two columns of photonic crystal holes are kept farther from each other and the width of the central homogenous injection path is larger where the electrical scattering is less significant. The results confirm theoretic analysis and numerical results, where the electrical scattering due to the embedded insulator holes is assumed as one of the major impediment for carrier movement both into and out from the active region. What's more, the voltage difference for various defect periods is much larger than that caused by doping offset. This means that the electrical performance of the device (steady state current and carrier level) is more sensitive to defect period than doping offset, which seems counter-intuitive before the study. The important conclusion from this study is that the embedded photonic crystal lattice of holes plays an important role in the electrical part of the modulator performance by introducing noticeable scattering for the free carriers. As the bias voltage is kept at 0.98 V for 10 dB modulation depth, the DC power consumption of the device is calculated to be 1.86 μ W (defect period 400 nm, doping offset 0.71 μ m).

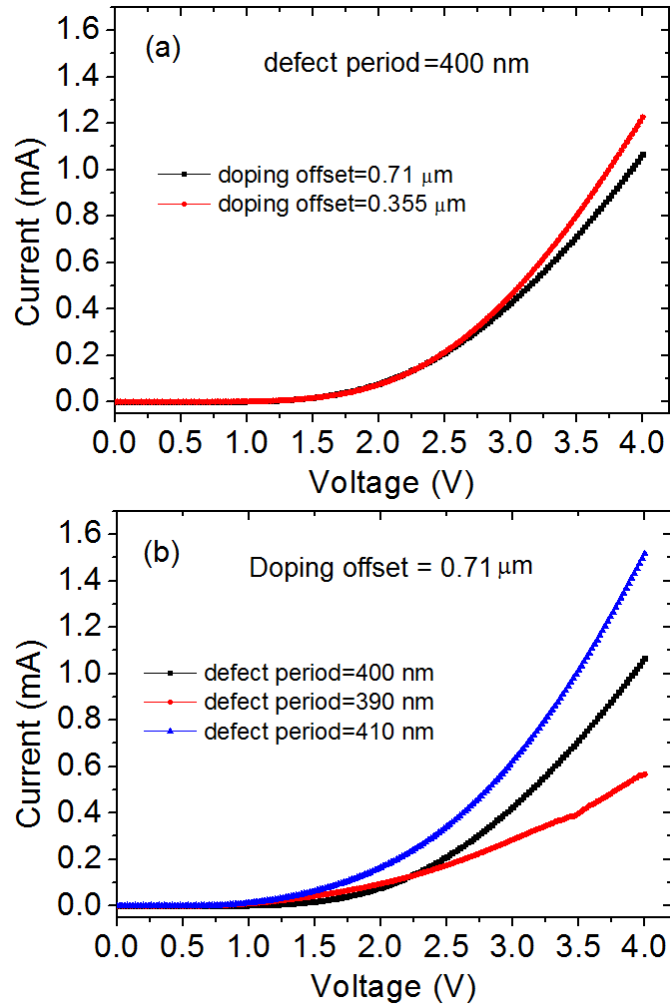


Figure 4.12 I-V characteristic of the devices with different design parameters: (a) doping offset changes when the defect period is kept at 400 nm; (b) defect period changes when the doping period is fixed at 0.71 μm

4.5. Summary

To conclude, in this chapter, the fabrication and measurement of the hybrid-lattice resonator based modulation is described which is electrically configured as P-I-N diode and operated in the carrier injection (forward bias) mode. The fabrication part involves complex semiconductor process steps and techniques for both passive definition of the photonic crystal waveguide based hybrid-lattice resonator

and active definition of the embedded P-I-N diodes, driving electrodes, and device passivation. The background information and physical mechanism of various process techniques are also introduced with details. On the experimental characterization part, both optical and electrical device measurement setup and results are discussed. In the optical part, the nanophotonics measurement set up is used for light path alignment and optical coupling. The transmission spectrum of the device is measured with a tunable laser source and optical spectrum analyzer, based on which the Q factor of the photonic nanocavity is demonstrated. In the electrical part, the I-V characteristic of the device is measured with a probe station and semiconductor parameter analyzer. Both optical and electrical measurement results show a high degree agreement with the numerical study in the previous chapters and sections.

CHAPTER

5. SUMMARY AND FUTURE WORK

In this chapter, a comprehensive summary and comparison of all the devices studied in this work is first given in Section 5.1. The possible areas of future work are then discussed in Section 5.2.

5.1. Summary

In this work, different optical and electrical approaches have been proposed and studied toward the goal of silicon integrated electro-optic modulators with ultra-low energy consumption. The devices of interest belong to a more general device category of optoelectronic devices, where quite intuitively, the overall device performance is determined by combined effects from both optical and electrical sides of the design. Around four years before the time of this writing when starting the project, Intel announced the world's first 40 GHz silicon laser modulator, which is based on the waveguide MZI configuration and free carrier depletion mode operation. For the first time, this combination of photonic waveguide and electrical junction diode was known as a commercially viable way of constructing multi-GHz optical modulators based on pure silicon. Before that, silicon was much less well known for realizing high speed optical modulators due to the absence of a nonlinear Pockels effect. Since then, there has been increasingly strong attention to high bandwidth silicon photonic device research and one important goal in this field is to further reduce device dimensions and energy consumption without sacrificing either device speed or modulation contrast. The resultant modulating component is therefore compatible with electronic CMOS devices to realize high density electro-optic integrated circuits. The solution lies in the photonic slow light and resonant media, where the nonlinear EO interaction can be enhanced to significantly reduce device footprint.

That was where the work covered in this project began. Firstly, the goal of searching for the so-called “optimum” optical medium for the solution of compact high speed optical modulation was pursued consistently. In those early studies, Fabry-Perot resonators and cross waveguide resonators were employed for carrier injection mode operation. The modulation was based on the resonance peak shift of the cavity in such a way that the overall transmitted optical intensity would be modulated by the external electrical bias signal. The FP resonator provided a way of realizing optical confinement of the optical mode in an ultra-compact modal volume and device footprint, and the carrier injection enabled a large amount of localized index perturbation so that the large transmission contrast could be achieved without employing a high Q factor resonator. However, the cavity itself had limited Q factor for an acceptable level of optical loss, which resulted in a limited EO sensitivity. The ultra-thin silicon rib also significantly limited the carrier movement in terms of injected concentration level and injection momentum. Therefore, the cross waveguide resonator structure was proposed to alleviate the limitations found in the FP resonator. Since the carriers were injected from the two branch waveguides instead of the thin silicon rib, the carrier momentum loss was reduced drastically and the injected free carrier concentration was also improved.

Table 5.1 Summary of the major FOMs of the devices studied in this work.

Structure	FP resonator (injection)	Cross waveguide (injection)	Hybrid lattice resonator (depletion)	Polymer P-S-N diode capacitor (depletion, Pockels)
Section	2.3.1	2.3.2	2.4	3.3
Footprint ^a (μm^2)	2.1	16	69	5.5 (mm)
Speed ^b (GHz)	0.3	2.9	238 ^f	269
V_{pp} (V)	1.18	1.65	15	10
Energy ^c (fJ/bit)	86 ($\mu\text{W}/\mu\text{m}$)	17.3 (mW)	26.6	5.83
MD ^d (dB)	>10	5.7	10	N/A
Loss ^e (dB)	-	1.68 (impurity loss)	2.5 (insertion)	0.78 (dB/mm)

- a. Measured as length of the phase shifter for waveguide MZI based devices;
- b. Measured as 3-dB bandwidth for waveguide MZI based devices;
- c. Measured as DC power for injection mode devices and AC energy for depletion mode devices;
- d. Destructive interference is assumed at π phase shift for waveguide MZI based devices;

- e. Measured as propagation loss per unit length for waveguide MZI based devices;
- f. Speed may be further limited by the additional practical constraints explained in Section 2.4.3.

One tradeoff made though is the slightly larger device dimension associated with the cross waveguide resonator.

The cross waveguide structure was approaching the upper limit of what a 1D photonic crystal cavity could do for an EO modulator. At the same time, it was found that the speed of the carrier injection mode operation was significantly limited by the slow rise time of the free carriers. Therefore, a more complicated 2D photonic crystal resonator structure was explored where the in-plane optical confinement was more than one order of magnitude stronger in terms of Q factor. Additionally, the P⁺-P-N-N⁺ diode structure was explored where a new operation mode called “breakdown-delay based depletion mode” was found. This operation mode, when combined with the hybrid-lattice resonator, resulted in a modulation speed that was about two orders of magnitude higher than the injection mode operation that was based on 1D photonic crystal resonators. Moreover, the DC energy consumption of the device was almost zero while the AC energy consumption was also ultra-low.

More recently, the limitation of free carriers became more and more apparent in terms of both device speed and nonlinear EO efficiency. As an alternative approach, nonlinear optical polymers with either strong Pockels or Kerr effect coefficient had been studied intensively for high speed EO modulation purposes. The motivation of nonlinear polymers was their almost instant EO response time and therefore ultra-high optical bandwidth. Moreover, the modulation efficiency could be improved at the same time due to the stronger Pockels or Kerr effect than free carrier effect. Considering these exclusive benefits from polymers, a new electrical configuration was proposed and studied that was able to combine the EO efficiency of both free carrier and Pockels polymer. The answer was the polymer-infiltrated P-S-N diode capacitor. In that particular configuration, the index change from the free carriers could be added constructively to that from the polymer. The overall EO efficiency was proved to be noticeably higher than the device that relied on either EO active medium alone. Additionally, the geometric aspect ratio of

the slot waveguide was reduced to alleviate RC limitation of the device speed so that a much higher device 3-dB bandwidth was found compared to previous devices based on a similar waveguide configuration. The detailed performance FOMs for all the devices studied in this work are shown in Tab. 5.1.

5.2. Future work

As we look forward into the near future, silicon modulators will still be a high priority research topic in the general field of silicon photonics, and the work presented in this writing will be among the necessary steps in the development path of the technology. Based on the results that have already been discussed, the following trends in the technology evolution might be most interesting to explore. Even before that, the active and dynamic characterization of the hybrid lattice modulator fabricated in Chapter 4 will be continued and reported in future publications.

First, the polymer based silicon modulator is one of the promising approaches in this field and sub-THz speed modulation has only been proposed theoretically so far. Therefore, the polymer MZI configuration can be further explored to take into consideration practical limitations in experimental demonstration. As one step further, polymer photonic crystal cavity modulators can be studied both theoretically and experimentally. The fundamental bottlenecks in speed, energy, and dimension need to be challenged with more consolidated effort. The necessary modification of the conventional optical resonators should be made to enhance the nonlinear interaction between polymer and optical media.

Apart from modulators, photonic slow light and resonance media are also promising candidates for high sensitivity optical sensors for chemicals and bio-chemicals. The platform can be based on optofluidics and microfluidics for efficient chemical delivery. Photonic resonance based sensors can be sensitive enough to detect the presence of certain chemicals at an ultra-low concentration level, which find application in biomedical analysis, epidemic control, and public security.

APPENDIX A

EO SENSITIVITY OF A CAVITY RESONATOR FOR HIGH SPEED MODULATION

Generally, for cavity resonator based intensity modulators, the dependence of EO sensitivity on optical confinement and the embedded EO active region is analyzed as follows. Assuming a Gaussian shape for the resonance peak, we have

$$P_{\text{OFF}}(\omega) = Ae^{-(\omega-\omega_0)^2/2\sigma^2} \quad \Delta\omega_{\text{FWHM}} = \frac{\omega_0}{Q} = 2.35\sigma \quad (\text{A. 1})$$

where A and ω_0 are the peak transmission and resonance frequency at the OFF state respectively. When the device is biased, the resonance peak shifts to ω_0' . At the ON state, transmission at ω_0 and MD are calculated as

$$P_{\text{ON}}(\omega_0) = Ae^{-(\omega_0-\omega_0')^2/2\sigma^2} \quad \text{MD} = 10\log[P_{\text{OFF}}(\omega_0)/P_{\text{ON}}(\omega_0)] = 5\log e \cdot (\omega_0 - \omega_0')^2 / \sigma^2 \quad (\text{A. 2})$$

where $\omega_0 = 2\pi C/\lambda_0$ and λ_0 is the vacuum wavelength. For optical mode perturbation in a microcavity system, the following condition applies:

$$\lambda = \lambda_0/n_{\text{eff}} = 2L_{\text{cav}}/k \quad \Delta n_{\text{eff}} \approx \Delta n V_{\text{ol}}/V_{\text{mod}} \quad (\text{A. 3})$$

where L_{cav} is the cavity defect length and k is an integer; Δn_{eff} is the effective index change of the cavity mode between ON and OFF states and Δn is the absolute index change of the EO active medium, e.g. free carriers, NLO organics; V_{ol} is the overlapped volume between EO active medium and cavity mode

distribution. Here, the effective index approximation is used to relate Δn_{eff} to localized index change. By inserting Eq. (A. 1) and (A. 2) into Eq. (A. 3) and defining EO sensitivity as $\eta_{\text{EO}} = \text{MD}/\Delta n^2$, one arrives at the following:

$$\eta_{\text{EO}} \approx \left(\frac{3.5}{n_{\text{eff}}} \right)^2 \left(\frac{Q}{V_{\text{mod}}} \right)^2 V_{\text{ol}}^2 \quad (\text{A. 4})$$

The first term on the right hand side of Eq. (A. 4) is nearly fixed for a given material system and operating wavelength, e.g. NIR operation in a silicon PC waveguide; the second term represents the optical confinement of the resonance medium; and the last term is partially the electro-optic coupling efficiency which can be engineered separately through the configuration of the embedded EO active medium. Although η_{EO} increases monotonously with Q^2 , the quality factor of a practically useful resonator should be capped at $\sim 10^4$ for sub-THz transmission capacity in NIR regime due to the photon lifetime limitation $\tau_{\text{ph}} = Q/\omega_0$ (ω_0 is the resonance frequency).

APPENDIX B

LIST OF PUBLICATIONS AND PATENTS FROM THIS WORK

Journal Articles

1. M. Xin, C. E. Png, S. T. Lim, V. Dixit, and A. J. Danner, “A high speed electro-optic phase shifter based on a polymer-infiltrated P-S-N diode capacitor,” *Opt. Express* **19**, 14354-14369 (2011).
2. M. Xin, C. E. Png, and A. J. Danner, “A breakdown delay-based depletion mode silicon modulator with photonic hybrid-lattice resonator,” *Opt. Express* **19**, 5063-5076 (2011).
3. M. Xin, L. Zhang, C. E. Png, J. H. Teng, and A. J. Danner, “Asymmetric open cavities for beam steering and switching from line-defect photonic crystals,” *J. Opt. Soc. Am. B* **27**, 1153 (2010).
4. M. Xin, A. J. Danner, C. E. Png, and S. T. Lim, “Theoretical study of a cross waveguide resonator-based silicon electro-optic modulator with low power consumption,” *J. Opt. Soc. Am. B* **26**, 2176 (2009).
5. M. Xin, A. J. Danner, C. E. Png, and S. T. Lim, “Resonator-based silicon electro-optic modulator with low power consumption,” *Jpn. J. Appl. Phys.* **48**, 04C104 (2009).
6. L. Zhang, M. Xin, J. H. Teng, and S. J. Chua, “Photonic band structure of nanoporous anodized aluminum oxide with radius-to-period ratio modulation,” *Comput. Mater. Sci.* **49**, Issue 1, S153-S156 (2010).

Conference Presentations and Proceedings

7. M. Xin, C. E. Png, S. T. Lim, V. Dixit, A. J. Danner, and E. P. Li, “Enhancing performance of

- high speed electro-optic phase shifters with a polymer-infiltrated P-S-N diode capacitor,” Submitted to 8th IEEE International Conference on Group IV Photonics, London, England, Sep. 14-16, 2011.
8. M. Xin, C. E. Png, S. T. Lim, V. Dixit, and A. J. Danner, “A high speed electro-optic phase shifter based on a polymer-infiltrated P-S-N diode capacitor,” to be presented at CLEO Pacific Rim 2011, Sydney, Australia, Aug. 28-Sep. 1, 2011.
 9. M. Xin, C. E. Png, and A. J. Danner, “A compact depletion mode silicon modulator based on a photonic hybrid-lattice mode-gap resonator,” Proc. SPIE 7943, 794318 (2011). (Presented at Photonics West 2011, San Francisco, CA, USA, Jan. 22-27, 2011)
 10. M. Xin, A. J. Danner, C. E. Png, and S. T. Lim, “Compact silicon electro-optic modulator based on a cross waveguide resonator,” presented at ICMAT (International Conference on Material for Advanced Technology), Singapore, Jun. 2009.
 11. M. Xin, A. J. Danner, C. E. Png, and S. T. Lim, “Cross waveguide resonator-based silicon electro-optic modulator with low power consumption,” presented at SMONP (Nanophotonics Down Under), Melbourne, Australia, Jun. 2009.
 12. M. Xin, A. J. Danner, C. E. Png, and S. T. Lim, “A resonator-based silicon electro-optic modulator with ultra-low power consumption and optimized modulation performance,” presented at IEEE Photonic Global, Singapore, Dec. 2008.
 13. M. Xin, A. J. Danner, C. E. Png, and S. T. Lim, "Resonator-based silicon electro-optic modulator with low power consumption," presented at SSDM (International Conference on Solid State Devices and Materials), Tsukuba, Japan, Sep. 2008.

Patents

M. Xin, C. E. Png, and A. J. Danner, “Breakdown delay based carrier depletion for high speed silicon optical modulators,” (US provisional USPTO 61/423,613).

LIST OF REFERENCES

1. R. Soref, "The past, present, and future of silicon photonics," *IEEE Journal of Selected Topics in Quantum Electronics* **12**, 1678-1687 (2006).
2. R. A. Soref, and J. P. Lorenzo, "All-silicon active and passive guided-wave components for $\lambda=1.3$ and $1.6 \mu\text{m}$," *IEEE Journal of Quantum Electronics* **22**, 873-879 (1986).
3. J. P. Lorenzo, and R. A. Soref, "1.3 μm electrooptic silicon switch," *Applied Physics Letters* **51**, 6-8 (1987).
4. R. A. Soref, and B. R. Bennett, "Electrooptical effects in silicon," *IEEE Journal of Quantum Electronics* **23**, 123-129 (1987).
5. J. N. Winn, R. D. Meade, and J. D. Joannopoulos, "2-dimensional photonic band-gap materials," *Journal of Modern Optics* **41**, 257-273 (1994).
6. R. D. Meade, A. Devenyi, J. D. Joannopoulos, O. L. Alerhand, D. A. Smith, and K. Kash, "Novel applications of photonic band-gap materials - low-loss bends and high q-cavities," *Journal of Applied Physics* **75**, 4753-4755 (1994).
7. H. Gersen, T. J. Karle, R. J. P. Engelen, W. Bogaerts, J. P. Korterik, N. F. van Hulst, T. F. Krauss, and L. Kuipers, "Real-space observation of ultraslow light in photonic crystal waveguides," *Physical Review Letters* **94** (2005).
8. J. S. Foresi, P. R. Villeneuve, J. Ferrera, E. R. Thoen, G. Steinmeyer, S. Fan, J. D. Joannopoulos, L. C. Kimerling, H. I. Smith, and E. P. Ippen, "Photonic-bandgap microcavities in optical waveguides," *Nature* **390**, 143-145 (1997).
9. E. Yablonovitch, T. J. Gmitter, R. D. Meade, A. M. Rappe, K. D. Brommer, and J. D. Joannopoulos, "Donor and acceptor modes in photonic band-structure," *Physical Review Letters* **67**, 3380-3383 (1991).
10. G. T. Reed, G. Mashanovich, F. Y. Gardes, and D. J. Thomson, "Silicon optical modulators (vol 4, pg 518, 2010)," *Nature Photonics* **4**, 661-661 (2010).
11. A. S. Liu, R. Jones, L. Liao, D. Samara-Rubio, D. Rubin, O. Cohen, R. Nicolaescu, and M. Paniccia, "A high-speed silicon optical modulator based on a metal-oxide-semiconductor capacitor," *Nature* **427**, 615-618 (2004).
12. L. Liao, A. Liu, D. Rubin, J. Basak, Y. Chetrit, H. Nguyen, R. Cohen, N. Izhaky, and M. Paniccia, "40 Gbit/s silicon optical modulator for highspeed applications," *Electronics Letters* **43**, 1196-1197 (2007).
13. A. S. Liu, L. Liao, D. Rubin, H. Nguyen, B. Ciftcioglu, Y. Chetrit, N. Izhaky, and M. Paniccia, "High-speed optical modulation based on carrier depletion in a silicon waveguide," *Optics Express* **15**, 660-668 (2007).

14. N. N. Feng, S. R. Liao, D. Z. Feng, P. Dong, D. W. Zheng, H. Liang, R. Shafiqi, G. L. Li, J. E. Cunningham, A. V. Krishnamoorthy, and M. Asghari, "High speed carrier-depletion modulators with 1.4V-cm V pi L integrated on 0.25 mu m silicon-on-insulator waveguides," *Optics Express* **18**, 7994-7999 (2010).
15. C. E. Png, S. P. Chan, S. T. Lim, and G. T. Reed, "Optical phase modulators for MHz and GHz modulation in silicon-on-insulator (SOI)," *Journal of Lightwave Technology* **22**, 1573-1582 (2004).
16. C. A. Barrios, and M. Lipson, "Modeling and analysis of high-speed electro-optic modulation in high confinement silicon waveguides using metal-oxide-semiconductor configuration," *Journal of Applied Physics* **96**, 6008-6015 (2004).
17. C. A. Barrios, "Electrooptic modulation of multisilicon-on-insulator photonic wires," *Journal of Lightwave Technology* **24**, 2146-2155 (2006).
18. F. Y. Gardes, G. T. Reed, N. G. Emerson, and C. E. Png, "A sub-micron depletion-type photonic modulator in Silicon On Insulator," *Optics Express* **13**, 8845-8854 (2005).
19. W. M. J. Green, M. J. Rooks, L. Sekaric, and Y. A. Vlasov, "Ultra-compact, low RF power, 10 gb/s silicon Mach-Zehnder modulator," *Optics Express* **15**, 17106-17113 (2007).
20. L. L. Gu, W. Jiang, X. N. Chen, L. Wang, and R. T. Chen, "High speed silicon photonic crystal waveguide modulator for low voltage operation," *Applied Physics Letters* **90** (2007).
21. D. Marris-Morini, L. Vivien, J. M. Fedeli, E. Cassan, P. Lyan, and S. Laval, "Low loss and high speed silicon optical modulator based on a lateral carrier depletion structure," *Optics Express* **16**, 334-339 (2008).
22. M. R. Watts, W. A. Zortman, D. C. Trotter, R. W. Young, and A. L. Lentine, "Low-Voltage, Compact, Depletion-Mode, Silicon Mach-Zehnder Modulator," *IEEE Journal of Selected Topics in Quantum Electronics* **16**, 159-164 (2010).
23. Q. F. Xu, B. Schmidt, S. Pradhan, and M. Lipson, "Micrometre-scale silicon electro-optic modulator," *Nature* **435**, 325-327 (2005).
24. Q. F. Xu, S. Manipatruni, B. Schmidt, J. Shakya, and M. Lipson, "12.5 Gbit/s carrier-injection-based silicon micro-ring silicon modulators," *Optics Express* **15**, 430-436 (2007).
25. B. Schmidt, Q. F. Xu, J. Shakya, S. Manipatruni, and M. Lipson, "Compact electro-optic modulator on silicon-on-insulator substrates using cavities with ultra-small modal volumes," *Optics Express* **15**, 3140-3148 (2007).
26. M. R. Watts, D. C. Trotter, R. W. Young, and A. L. Lentine, *Ultralow Power Silicon Microdisk Modulators and Switches* (2008).
27. P. Dong, S. R. Liao, D. Z. Feng, H. Liang, D. W. Zheng, R. Shafiqi, C. C. Kung, W. Qian, G. L. Li, X. Z. Zheng, A. V. Krishnamoorthy, and M. Asghari, "Low V-pp, ultralow-energy, compact, high-speed silicon electro-optic modulator," *Optics Express* **17**, 22484-22490 (2009).

28. F. Y. Gardes, A. Brimont, P. Sanchis, G. Rasigade, D. Marris-Morini, L. O'Faolain, F. Dong, J. M. Fedeli, P. Dumon, L. Vivien, T. F. Krauss, G. T. Reed, and J. Marti, "High-speed modulation of a compact silicon ring resonator based on a reverse-biased pn diode," *Optics Express* **17**, 21986-21991 (2009).
29. Q. F. Xu, "Silicon dual-ring modulator," *Optics Express* **17**, 20783-20793 (2009).
30. C. Koos, L. Jacome, C. Poulton, J. Leuthold, and W. Freude, "Nonlinear silicon-on-insulator waveguides for all-optical signal processing," *Optics Express* **15**, 5976-5990 (2007).
31. J. Leuthold, W. Freude, J. M. Brosi, R. Baets, P. Dumon, I. Biaggio, M. L. Scimeca, F. Diederich, B. Frank, and C. Koos, "Silicon Organic Hybrid Technology-A Platform for Practical Nonlinear Optics," *Proceedings of the IEEE* **97**, 1304-1316 (2009).
32. R. Ding, T. Baehr-Jones, Y. Liu, R. Bojko, J. Witzens, S. Huang, J. Luo, S. Benight, P. Sullivan, J. M. Fedeli, M. Fournier, L. Dalton, A. Jen, and M. Hochberg, "Demonstration of a low V pi L modulator with GHz bandwidth based on electro-optic polymer-clad silicon slot waveguides," *Optics Express* **18**, 15618-15623 (2010).
33. V. R. Almeida, Q. F. Xu, C. A. Barrios, and M. Lipson, "Guiding and confining light in void nanostructure," *Optics Letters* **29**, 1209-1211 (2004).
34. M. Hochberg, T. Baehr-Jones, G. Wang, M. Shearn, K. Harvard, J. Luo, B. Chen, Z. Shi, R. Lawson, P. Sullivan, A. K. Y. Jen, L. Dalton, and A. Scherer, "Terahertz all-optical modulation in a silicon-polymer hybrid system," *Nature Materials* **5**, 703-709 (2006).
35. Y. Enami, C. T. Derose, D. Mathine, C. Loychik, C. Greenlee, R. A. Norwood, T. D. Kim, J. Luo, Y. Tian, A. K. Y. Jen, and N. Peyghambarian, "Hybrid polymer/sol-gel waveguide modulators with exceptionally large electro-optic coefficients," *Nature Photonics* **1**, 180-185 (2007).
36. J. T. Robinson, K. Preston, O. Painter, and M. Lipson, "First-principle derivation of gain in high-index-contrast waveguides," *Optics Express* **16**, 16659-16669 (2008).
37. J. M. Brosi, C. Koos, L. C. Andreani, M. Waldow, J. Leuthold, and W. Freude, "High-speed low-voltage electro-optic modulator with a polymer-infiltrated silicon photonic crystal waveguide," *Optics Express* **16**, 4177-4191 (2008).
38. C. Koos, P. Vorreau, T. Vallaitis, P. Dumon, W. Bogaerts, R. Baets, B. Esembeson, I. Biaggio, T. Michinobu, F. Diederich, W. Freude, and J. Leuthold, "All-optical high-speed signal processing with silicon-organic hybrid slot waveguides," *Nature Photonics* **3**, 216-219 (2009).
39. C. Y. Lin, X. L. Wang, S. Chakravarty, B. S. Lee, W. C. Lai, J. D. Luo, A. K. Y. Jen, and R. T. Chen, "Electro-optic polymer infiltrated silicon photonic crystal slot waveguide modulator with 23 dB slow light enhancement," *Applied Physics Letters* **97** (2010).
40. J. H. Wulbern, A. Petrov, and M. Eich, "Electro-optical modulator in a polymer-infiltrated silicon slotted photonic crystal waveguide heterostructure resonator," *Optics Express* **17**, 304-313 (2009).

41. J. H. Wülbern, J. Hampe, A. Petrov, M. Eich, J. Luo, A. K. Y. Jen, A. Di Falco, T. F. Krauss, and J. r. Bruns, "Electro-optic modulation in slotted resonant photonic crystal heterostructures," *Applied Physics Letters* **94**, 241107 (2009).
42. M. Gould, T. Baehr-Jones, R. Ding, S. Huang, J. D. Luo, A. K. Y. Jen, J. M. Fedeli, M. Fournier, and M. Hochberg, "Silicon-polymer hybrid slot waveguide ring-resonator modulator," *Optics Express* **19**, 3952-3961 (2011).
43. B. Jalali, S. Fathpour, and K. Tsia, "Green silicon photonics," *Optics and Photonics News* **20**, 18-23 (2009).
44. "ATLAS User's Manual," (SILVACO International, Santa Clara, CA, 2005).
45. S. M. Sze, and K. K. Ng, "Physics of Semiconductor Devices," (John Wiley & Sons, Inc., Hoboken, New Jersey, 2007).
46. S. Selberherr, "Process and device modeling for VLSI," *Microelectronics and Reliability* **24**, 225-257 (1984).
47. "Fullwave 5.0 User Guide," (RSoft Design Group, Inc., Ossining, NY, 2006).
48. A. Tavlove, "Computational Electrodynamics: The Finite-Difference Time-Domain Method," (Artech House, Norwood, MA, 1995).
49. K. S. Yee, "Numerical solution of initial boundary value problems involving maxwells equations in isotropic media," *IEEE Transactions on Antennas and Propagation* **AP14**, 302-& (1966).
50. J. D. Joannopoulos, S. G. Johnson, J. N. Winn, and R. D. Meade, "Photonic Crystals-Molding the Flow of Light," (Princeton University Press, Princeton, New Jersey, 2008).
51. "Bandsolve 3.0 User Guide," (RSoft Design Group, Inc., Ossining, NY, 2006).
52. D. B. M. Klaassen, "A Unified Mobility Model for Device Simulation - I. Model Equations and Concentration Dependence," *Solid-State Electronics* **35**, 953-959 (1992).
53. D. B. M. Klaassen, "A Unified Mobility Model for Device Simulation - II. Temperature Dependence of Carrier Mobility and Lifetime," *Solid-State Electronics* **35**, 961-967 (1992).
54. F. X. Kartner, S. Akiyama, G. Barbastathis, T. Barwicz, H. Byun, D. T. Danielson, F. Gan, F. Grawert, C. W. Holzwarth, J. L. Hoyt, E. P. Ippen, M. Kim, L. C. Kimerling, J. Liu, J. Michel, O. O. Olubuyide, J. S. Orcutt, M. Park, M. Perrott, M. A. Popovic, P. T. Rackich, R. J. Ram, H. I. Smith, and M. R. Watts, "Electronic photonic integrated circuits for high speed, high resolution, analog to digital conversion - art. no. 612503," in *Silicon Photonics*, J. A. Kubby, and G. T. Reed, eds. (2006), pp. 12503-12503.
55. N. Moll, R. Harbers, R. F. Mahrt, and G. L. Bona, "Integrated all-optical switch in a cross-waveguide geometry," *Applied Physics Letters* **88** (2006).
56. P. B. Deotare, M. W. McCutcheon, I. W. Frank, M. Khan, and M. Loncar, "High quality factor photonic crystal nanobeam cavities," *Applied Physics Letters* **94** (2009).

57. P. B. Deotare, M. W. McCutcheon, I. W. Frank, M. Khan, and M. Loncar, "Coupled photonic crystal nanobeam cavities," *Applied Physics Letters* **95** (2009).
58. T. Asano, B. S. Song, Y. Akahane, and S. Noda, "Ultra-high-Q nanocavities in two-dimensional photonic crystal slabs," *IEEE Journal of Selected Topics in Quantum Electronics* **12**, 1123-1134 (2006).
59. D. Englund, I. Fushman, and J. Vuckovic, "General recipe for designing photonic crystal cavities," *Optics Express* **13**, 5961-5975 (2005).
60. Y. Hamachi, S. Kubo, and T. Baba, "Slow light with low dispersion and nonlinear enhancement in a lattice-shifted photonic crystal waveguide," *Optics Letters* **34**, 1072-1074 (2009).
61. N. Ozaki, Y. Kitagawa, Y. Takata, N. Ikeda, Y. Watanabe, A. Mizutani, Y. Sugimoto, and K. Asakawa, "High transmission recovery of slow light in a photonic crystal waveguide using a hetero group velocity waveguide," *Optics Express* **15**, 7974-7983 (2007).
62. J. P. Hugonin, P. Lalanne, T. P. White, and T. E. Krauss, "Coupling into slow-mode photonic crystal waveguides," *Optics Letters* **32**, 2638-2640 (2007).
63. P. Rodin, U. Ebert, A. Minarsky, and I. Grekhov, "Theory of superfast fronts of impact ionization in semiconductor structures," *Journal of Applied Physics* **102** (2007).
64. S. L. Konsek, and T. P. Pearsall, "Dynamics of electron tunneling in semiconductor nanostructures (vol B 67, art no 045306, 2003)," *Physical Review B* **67** (2003).
65. F. Zhang, L. N. Shi, C. F. Li, W. Yu, and X. W. Sun, "A high-power solid-state p(+)-n-n(+) diode for picosecond-range closing switching," *Semiconductor Science and Technology* **20**, 991-997 (2005).
66. L. Liao, D. Samara-Rubio, M. Morse, A. S. Liu, D. Hodge, D. Rubin, U. D. Keil, and T. Franck, "High speed silicon Mach-Zehnder modulator," *Optics Express* **13**, 3129-3135 (2005).
67. F. W. Gan, and F. X. Kartner, "High-speed silicon electrooptic modulator design," *IEEE Photonics Technology Letters* **17**, 1007-1009 (2005).
68. T. Baehr-Jones, B. Penkov, J. Q. Huang, P. Sullivan, J. Davies, J. Takayesu, J. D. Luo, T. D. Kim, L. Dalton, A. Jen, M. Hochberg, and A. Scherer, "Nonlinear polymer-clad silicon slot waveguide modulator with a half wave voltage of 0.25 V," *Applied Physics Letters* **92** (2008).
69. T. Gorman, S. Haxha, H. Ademgil, and J. J. Ju, "Ultra-High-Speed Deeply Etched Electrooptic Polymer Modulator," *IEEE Journal of Quantum Electronics* **44**, 1180-1187 (2008).
70. "Beamprop 7.0 User Guide," (RSoft Design Group, Inc., Ossining, NY, 2006).
71. R. Scarmozzino, and R. M. Osgood, "Comparison of finite-difference and fourier-transform solutions of the parabolic wave-equation with emphasis on integrated-optics applications," *Journal of the Optical Society of America a-Optics Image Science and Vision* **8**, 724-731 (1991).
72. R. Clauberg, and P. Vonallmen, "Vectorial beam-propagation method for integrated-optics," *Electronics Letters* **27**, 654-655 (1991).

73. K. Preston, and M. Lipson, "Slot waveguides with polycrystalline silicon for electrical injection," *Optics Express* **17**, 1527-1534 (2009).
74. J. Witzens, T. Baehr-Jones, and M. Hochberg, "Design of transmission line driven slot waveguide Mach-Zehnder interferometers and application to analog optical links," *Optics Express* **18**, 16902-16928 (2010).
75. H. Cao, T. F. Heinz, and A. Nahata, "Electro-optic detection of femtosecond electromagnetic pulses by use of poled polymers," *Optics Letters* **27**, 775-777 (2002).
76. P. Mueller, M. Wellenzohn, and R. Hainberger, "Nonlinearity of optimized silicon photonic slot waveguides," *Optics Express* **17**, 9282-9287 (2009).
77. A. G. Rickman, G. T. Reed, and F. Namavar, "Silicon-on-insulator optical rib wave-guide loss and mode characteristics," *Journal of Lightwave Technology* **12**, 1771-1776 (1994).
78. C. E. Png, G. H. Park, S. T. Lim, E. P. Li, A. J. Danner, K. Ogawa, and Y. T. Tan, "Electrically controlled silicon-based photonic crystal chromatic dispersion compensator with ultralow power consumption," *Applied Physics Letters* **93**, 061111 (2008).
79. G. P. Agrawal, *Fiber-Optic Communication Systems* (John Wiley & Sons, Inc., New Jersey, 1997).
80. T. D. Kim, J. W. Kang, J. D. Luo, S. H. Jang, J. W. Ka, N. Tucker, J. B. Benedict, L. R. Dalton, T. Gray, R. M. Overney, D. H. Park, W. N. Herman, and A. K. Y. Jen, "Ultralarge and thermally stable electro-optic activities from supramolecular self-assembled molecular glasses," *Journal of the American Chemical Society* **129**, 488-489 (2007).
81. K. Brunner, U. Bockelmann, G. Abstreiter, M. Walther, G. Bohm, G. Trankle, and G. Weimann, "Photoluminescence from a single GaAs/AlGaAs quantum dot," *Physical Review Letters* **69**, 3216-3219 (1992).
82. J. T. Gallo, T. Kimura, S. Ura, T. Suhara, and H. Nishihara, "Method for characterizing poled-polymer wave-guides for electrooptic integrated-optical-circuit applications," *Optics Letters* **18**, 349-351 (1993).
83. H. S. Lee, T. D. Kang, H. Lee, S. K. Lee, J. H. Kim, and D. H. Choi, "Ellipsometric study of the poling effect on nonlinear-optical side-chain polymers containing disperse red 1," *Journal of Applied Physics* **102** (2007).
84. A. Alping, X. S. Wu, T. R. Hausken, and L. A. Coldren, "Highly efficient waveguide phase modulator for integrated optoelectronics " *Applied Physics Letters* **48**, 3 (1986).
85. J. G. Mendoza-Alvarez, L. A. Coldren, A. Alping, R. H. Yan, T. Hausken, K. Lee, and K. Pedrotti, "Analysis of depletion edge translation lightwave modulators," *Journal of Lightwave Technology* **6** (1988).
86. W. Kim, W.-S. Yang, and H.-Y. Lee, "Effects of parasitic modes in high-speed LiNbO₃ optical modulators," *Optics Express* **12** (2004).

87. B. Bortnik, Y. C. Hung, H. Tazawa, B. J. Seo, J. D. Luo, A. K. Y. Jen, W. H. Steier, and H. R. Fetterman, "Electrooptic polymer ring resonator modulation up to 165 GHz," IEEE Journal of Selected Topics in Quantum Electronics **13**, 104-110 (2007).
88. "L-Edit Data Sheet ", http://www.tannereda.com/images/pdfs/Datasheets/DS_LEdit.pdf.
89. "ATHENA User's Manual," (SILVACO International, Santa Clara, CA, 2005).